University of Southampton

Faculty of Engineering and Physical Sciences

School of Electronics and Computer Science

Space Charge Modelling and Measurement in HVDC Extruded Cable Insulation

by

Yunpeng Zhan

A thesis submitted for the degree of Doctor of Philosophy

September 2020

University of Southampton

Abstract

Faculty of Engineering and Physical Sciences

School of Electronics and Computer Science

Thesis for the degree of Doctor of Philosophy

Space Charge Modelling and Measurement in HVDC Extruded Cable Insulation

by

Yunpeng Zhan

Space charge accumulation under the DC field is one of the most challenging issues in the further development of HVDC extruded cable systems. The electric field distribution over the insulation thickness is strongly affected by space charge, which further control the long-term reliability and life expectancy of the cable system. Although extensive efforts have been made to investigate the space charge behaviour in dielectrics, the charge generation and transport mechanisms are still not yet well understood. The space charge and field distribution in cable system cannot be calculated accurately by the conductivity model, which serves as an important reference for DC cable design. Thus this dissertation devotes to study space charge by numerical modelling and experimental investigation of space charge behaviour in cable insulation.

A numerical modelling approach based on bipolar charge transport theory has been developed to simulate the space charge dynamics in polymeric insulation of coaxial geometry. Based on previous experimental observations, a threshold electric field (10 kV/mm for polyethylene-based material) at which the charge injection takes place is introduced. The build-up of space charge in the medium size cable insulation in the presence of temperature gradient has been modelled and the field inversion phenomenon has been verified under the applied voltage of 90 kV. Compared with the traditional conductivity model, the new modelling method performs better as it well describes the charge generation and transport mechanisms. The space charge and field distribution in cable system under the voltage polarity reversal have been calculated, and the significant field enhancement near the conductor suggests that particular attentions need to be paid on the DC cable design and the operation methods of polarity reversal.

Considering the practical operation of HVDC cable systems, the thermal transient effects on the space charge behaviour in cable insulation have been investigated. It is found that the field

inversion can only take place with a higher load current which represents a higher general temperature and a larger temperature gradient, and this phenomenon can still be maintained even with the temperature decreasing. It is suggested that different loading conditions need to be considered in designing DC polymeric cables.

To study the hetero charge accumulation in cross-linked polyethylene, the formation and transport of the ionic charges have been considered and fed into the bipolar charge transport model. By introducing the impurity molecules serving as the ion-pairs with a dissociation coefficient, the modified model can be employed to investigate the hetero charge formation in XLPE material. Simulations have been performed in XLPE flat specimens, and it is found that if the ionic charges distribute predominantly and offset the electronic charges, the net charge distribution will exhibit as a hetero charge accumulation.

A pulsed electro-acoustic system for measuring space charge accumulation in cable insulation has been designed and built, and considerable hetero charges have been experimentally observed in the XLPE insulated cables. The modelling approach considering both the charge injection and ionic dissociation is employed to investigate the space charge behaviour in XLPE cables, and both the space charge and field distribution are consistent with the experimental observations in the original cables. It is found that the ionic charge behaviour interplays tightly with the electronic charge behaviour, and it is also suggested that the impurity concentration gradient needs to be considered in the degassed cables.

Table of Contents

List of Tables

List of Figures

List of Publication

Journal and Articles

Y. Zhan, G. Chen, and M. Hao, “Space charge modelling in HVDC extruded cable insulation,” *IEEE Trans. Dielectr. Electr. Insul.*, vol. 26, no. 1, pp. 43–50, 2019.

Y. Zhan, G. Chen and M. Hao, “Comparison of two models on simulating electric field in HVDC cable insulation,” *IEEE Trans. Dielectr. Electr. Insul.*, vol. 26, no. 4, pp. 1107–1115, 2019.

Y. Zhan, Z. Xu and G. Chen, “Space charge measurement and modelling in cross-linked polyethylene,” *Energies*, vol. 13, no. 8, p. 1906, 2020.

Y. Zhan and G. Chen, “Measurement and Modelling of Space Charge in XLPE Insulated Cable”, submitted to *IEEE Trans. Dielectr. Electr. Insul.*, under review.

Conference Papers and Presentations

ORAL PRESENTATIONS

“**Modelling Space Charge in HVDC Cable Insulation**”
Yunpeng Zhan, George Chen and Miao Hao, International Symposium on High Voltage Engineering (ISH), 2019.

“**Electric Field Calculation in HVDC Cable Insulation under Thermal Transient Effects**”
Yunpeng Zhan and George Chen, New Energy Electric Power System and Equipment, China, 2019.

POSTER PRESENTATIONS

“**Simulation of the Electrical Breakdown in Polymers**”
Yunpeng Zhan and George Chen, Universities High Voltage Network Colloquium (UHVnet), 2017.

“**Modelling Space Charge in the Coaxial Extruded Insulation**”
Yunpeng Zhan, George Chen and Ying Liu, International Symposium on HVDC Cable Systems (Jicable-HVDC’17), 2017.

“**Thermal Transient Effects on Space Charge Dynamics in HVDC Extruded Cable Insulation**”
Yunpeng Zhan, George Chen and Miao Hao, International Conference on the Properties and Applications of Dielectrics Materials (ICPADM), 2018, IEEE Conference.

“**Study of DC Breakdown in Multi-layered Insulation Systems**”
Miao Hao, ***Yunpeng Zhan*** and George Chen, International Conference on Electrical Materials and Power Equipment (ICEMPE), 2019, IEEE Conference.

Research Thesis: Declaration of Authorship

Print name:	Yunpeng Zhan
Title of thesis:	Space Charge Modelling and Measurement in HVDC Extruded Cable Insulation

I declare that this thesis and the work presented in it are my own and has been generated by me as the result of my own original research.

I confirm that:

1. This work was done wholly or mainly while in candidature for a research degree at this University;
2. Where any part of this thesis has previously been submitted for a degree or any other qualification at this University or any other institution, this has been clearly stated;
3. Where I have consulted the published work of others, this is always clearly attributed;
4. Where I have quoted from the work of others, the source is always given. With the exception of such quotations, this thesis is entirely my own work;
5. I have acknowledged all main sources of help;
6. Where the thesis is based on work done by myself jointly with others, I have made clear exactly what was done by others and what I have contributed myself;
7. None of this work has been published before submission.

Signature:

Date:

Acknowledgements

I would like to present my sincere appreciation to my supervisor Prof. George Chen, who offers invaluable suggestions and encouragements with great patience during my PhD study. I am very grateful for his innovated opinions and insight advices through weekly meetings and frequent discussions. I must thank him a lot for his generous assistance and support.

Many thanks to Dr Zhiqiang Xu and Dr Miao Hao, who give me training on the experimental techniques and provide a lot guidance on building the new PEA system for cable. Thanks to Dr Churui Zhou, Dr Bo Huang and Dr Yan Wang, who give many inspirations in my research area. Great thanks to Neil Palmer, Alan Welford, Charlie Reed and Mark Long for their talented and generous technical support on my experimental work in the Tony Davies High Voltage Laboratory.

Finally, thanks to my friends for them accompanies in Southampton and the keen support of my families from China.

Definitions and Abbreviations

Symbols

E, F	Electric field, Vm^{-1}
n, ρ	Space charge density, Cm^{-3}
ε	Permittivity of dielectric, Fm^{-1}
t	Time unit, s
q, e	Unit charge, $1.6 \times 10^{-19}C$
ϕ	Potential barrier height at the interface
J, j	Current density Am^{-2}
T	Temperature, K
k_B	Boltzmann constant, $k_B = 1.38 \times 10^{-23} JK^{-1}$
A	Richardson constant, $A = 1.2 \times 10^6 Am^{-1}K^{-2}$
K_D	Dissociation rate
K_R	Recombination rate
E_D	The activation energy for dissociation
v	Attempt-to-escape frequency, s^{-1}
c	Density of neutral ion-pairs
d_a	Average distance between traps, m
φ	Hopping barrier height
D_n	Fick’s diffusion coefficient
V, U	Voltage potential, V
μ	Mobility of charge carriers, $m^2V^{-1}s^{-1}$
σ	Conductivity, Sm^{-1}
θ	fraction coefficient
f_c	Cut-off frequency of the filter, Hz
C	Capacitance, F
R	Resistance, Ω
p	Acoustic wave pressure
r	Radius, mm
s	Source term for each species, $Cm^{-3}s^{-1}$
$S_0, S_1, S_2, S_3,$	Recombination coefficients for electrons/holes
D_e, D_h	Detrapping coefficients for electrons/holes
B_e, B_h	Trapping coefficients
w_{ei}, w_{hi}	Injection barrier height
w_{tre}, w_{trh}	Detrapping barrier height
$w_{\mu e}, w_{\mu h}$	Hopping barrier height
ρ_d	Material density, kgm^{-3}
Q	Heat source, Wm^{-3}
D_f	Diffusion coefficient
ρ_{al}	The resistivity of aluminium
D_d	Dissociation coefficient of the impurity molecule
w_d	Dissociation barrier
N	The neutral ion-pair density

Abbreviations

HV	High voltage
AC	Alternating current
DC	Direct current
kV	Kilo volts
MW	Megawatts
OF	Oil-filled cable
MI	Mass-impregnated cable
PP	Polypropylene
PPLP	Polypropylene-laminated-paper
LCC-CSC	Line-commutated current source converter
VSC	Self-commutated voltage source converter
LDPE	Low density polyethylene
XLPE	Cross-linked polyethylene
PEA	Pulsed electro-acoustic method
LIPP	Laser-induced pressure pulse method
LIMM	Laser intensity modulation method
TSM	Thermal step method
TPM	Thermal pulse method
PWP	Pressure wave propagation method
PVDF	Polyvinylidene fluoride
Hz	Hertz
SCLC	Space charge limited current
FEM	Finite element method
CFL	Courant-Friedrich-Levy relation
PDE	Partial differential equation

Chapter 1 Introduction

High voltage direct current (HVDC) transmission systems have been developed rapidly in recent decades, as this technology contributes to large-scale power delivery over long distance and the integration of renewable electricity sources [1]. As the main component of the HVDC power transmission, many different HVDC cable technologies have been developed and deployed successfully around the world. Although the majority of the well-established HVDC cable systems currently in service are based on paper/oil or mass impregnated insulation systems, the HVDC cable based on extruded polymeric insulation attracts more interests due to the factors of higher operating temperature, easier installation and maintenance and less environmental impacts [2]. However, it is well reported that the electric field distribution across the HVDC extruded cables can be greatly affected by space charge, which controls the cable system behaviour, particularly, its long-term reliability and life expectancy. By creating zones of high electric field, space charge accumulation can accelerate dielectric ageing process and even lead to early electrical failure [3] [4]. Therefore, measurement, understanding and modelling of space charge processes are essential, in order to calculate the electric field distribution in cable insulation for HVDC cable design and service lifetime estimation.

1.1 HVDC cable systems

It is well known that the transmission lines can be either overhead lines or cable lines. The overhead lines are cheaper; however, the cable lines are more attractive for crossing the vast urban area, and it is considered to be the only technically feasible solution for sea-crossing power transfer [5]. Compared with overhead lines, cable lines offer no visual impact and a reduced environmental impact, at least as perceived by the general public. Particularly, cable lines can be a technically attractive option when railway or motorway tunnels are already available. Using HVDC transmission for underground or undersea cable systems involves significant savings in the costs of installed cables and power losses, which will be illustrated in the following section.

1.1.1 HVAC versus HVDC transmission

The commercially electrical energy transmission first started with direct current (DC) in 1870s [6]. However, as alternating current (AC) technology was introduced in the development of electric power systems, the dominance of DC was soon terminated. Indeed, AC benefits from using transformers, which are straightforward to manufacture and efficient to achieve voltage conversion [7]. Furthermore, three-phase synchronous generators are superior to DC generators due to its more economical production and much higher efficiency. For these reasons, electric power is usually generated, transmitted and distributed in the format of alternating current [5]. However, it was found that high-voltage AC transmission have several disadvantages, which might compel a change to the DC technology, such as:

1. In AC transmission links, the transmission capacity and the transmission distance are limited by inductive and capacitive elements of overhead lines and cables [8]. Especially for a cable, since it can be treated as a long cylindrical capacitor, the AC transmission length is mainly limited by the charging current, and the reactive compensations are required with increased expense.
2. Direct connection between two AC systems with different frequencies is not possible [7].

With the development of high-power AC/DC and DC/AC conversion systems in past century, the costs, performance and reliability of the conversion systems are becoming acceptable [2] [9] [10]. Compared with HVAC transmission, the advantages of HVDC technology are attractive, for example:

1. HVDC lines involve lower capital costs (bipolar lines vs three phase lines), and the lower energy losses with the same current in the conductor. HVAC transmission not only has the ohmic losses in conductor but also induces more losses in conductor, sheath and armouring. Actually, the skin effect and the proximity effect in the conductor are absent in HVDC cables, as well as the additional losses outside the conductor, making the conductor section being exploited more efficiently. Furthermore, the mean higher operational electric field stress of HVDC cables also leads to a higher utilization of the cable [2].
2. HVDC link can interconnect the unsynchronized AC networks or that operated at different frequencies. The power flow in a DC scheme can be easily controlled at high speed, therefore a DC link can provide the stability of the interconnected AC grids [11].
3. HVDC cable lengths are not limited by charging current and no reactive compensation (for the cable itself) is required at the end stations or at intermediate points, as in the case of AC transmission systems.

Whenever long-distance power transmission is discussed, HVDC systems are always considered to be more economical than the corresponding HVAC systems with the same power rating due to lower line cost and lower losses, as shown in Figure 1-1 [5]. The concept of “break-even distance” is the value of transmission line length such that the savings in HVDC line and loss costs offset the higher converter station costs. For cable lines, the HVDC solution is generally more preferable than HVAC from the distances of about 40-50 km [11]. Currently, HVDC cable systems have been used worldwide for the transport of electrical energy, and one typical example of HVDC cable application is the submarine power transmission [12] [13]. In this case, overhead lines cannot be employed.

Furthermore, there is a drop-off in cable capacity with AC transmission over distance due to its reactive component of charging current. Therefore, HVDC cable systems are considered to be the only technically applicable solution for long distance undersea connections. Another typical application of HVDC transmission is to transfer power between two independent AC networks that are not synchronized, and one example of this is the 2,000 MW England-France interconnector linking the British and French transmission systems [5].

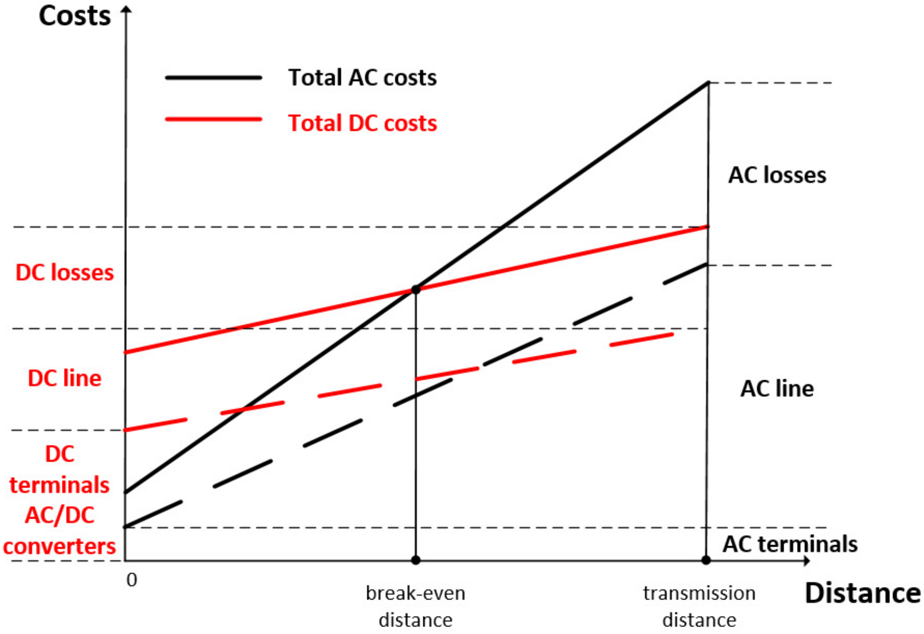

Figure 1-1. Qualitative plot comparing the costs of HVAC (black lines) and HVDC (red lines) transmission systems [5].

1.1.2 Different types of HVDC cables

A typical cable system consists of a cable and its accessories, i.e. joints and terminations. Joints are frequently applied in a HVDC cable system when the cable becomes too long to be produced in one length. Terminations are applied at the ends of a cable circuit to grade the electric field and to connect the cable to the power line. The types of HVDC cables can be classified by the different insulation systems. In the following, the main types of HVDC cables are briefly reviewed.

Oil-filled (OF) cable

Oil-filled cable, also known as fluid-filled cable, usually uses multi-layer impregnated paper as the main insulation, and the conductor of it incorporates a longitudinal duct to permit oil flowing along the cable. Generally, there are two kinds of OF cables, the first type is filled with low viscosity oil that requires pressure feeding units and oil refill tanks to maintain the high oil pressure in the cable in order to avoid generating bubbles in the oil, which limits the length of cable [7]. The second one is filled with the high viscosity oil in the cable to keep a stable pressure along the cable. In this way, this kind of OF cables does not need extra oil feeding units, and theoretically, the length of this kind of cable can be unlimited [14]. The potential capacity of the OF cables can be extremely large if the conductor could be cooled by the oil. The voltage rating of the OF cables reached 600 kV, and was able to be designed up to 1400 kV DC voltage [15]. However, because of its obvious disadvantages, like the risk of oil leakage, the limited cable length, oil-filled cables were gradually replaced by mass-impregnated cables or extruded cables.

Mass-impregnated (MI) cable

As an established cable technology for HVDC for over 60 years, MI cables have shown high performance and reliability in large HVDC power transmissions at up to 500 kV DC voltage [12]. The copper or aluminum conductor is covered by pure cellulose paper impregnated with oil and resin in MI cables. The length of MI cables can be unlimited based on the principle, due to no oil feeding system and external pressure being required. Moreover, the environment impacts can be neglected because there is no oil leakage in MI cables. However, the transmission capacity of MI cables is limited by the conductor temperature, which typically should not exceed 55°C [13]. It is also reported that the power capacity of MI cables can be potentially enlarged by applying laminated polymeric film and paper, such as polypropylene-laminated-paper (PPLP), to achieve operating under higher conductor temperature (80-90°C) [16]. The HVDC MI cable with PPLP insulation has been applied in commercial projects with improved power capacity and voltage level. For example, a 385 km MI submarine cable (improved by PPLP) was applied in the western HVDC link project, which is the first 600 kV subsea HVDC cable transmission with a 2200 MW power capacity in the world [17].

Polymer-insulated or extruded cable

Different from the paper insulated cables, polymeric material is used as the main insulation in extruded cables, as shown in Figure 1-2 [13]. The main insulation is polymeric and mostly based on polyethylene compounds, among which the preferred one is cross-linked polyethylene (XLPE). The cable manufacturing is done through a so-called triple extrusion line, as presented in Figure 1-3 [5]. The bare conductor enters the triple extrusion head, where insulation and screens are applied in sequence, followed immediately by a cross-linking phase of the insulation to give it the appropriate thermomechanical properties. The extruded cables have many significant advantages compared with other types of cables. First, the polymeric insulation can withstand a higher operational temperature, allowing more electrical power to be transferred for a given conductor cross-section than MI cables. Moreover, the cables are generally mechanically robust and the weight is lighter than the MI cables. Furthermore, the installation of extruded cables is simple and fast due to the easier jointing process. The last, the environmental problems can be avoided, because extruded cables will not cause any oil leakage. Due to these benefits, extruded cables have been developed rapidly in recent years, and they are expected to replace the traditional mass-impregnated lapped paper cables.

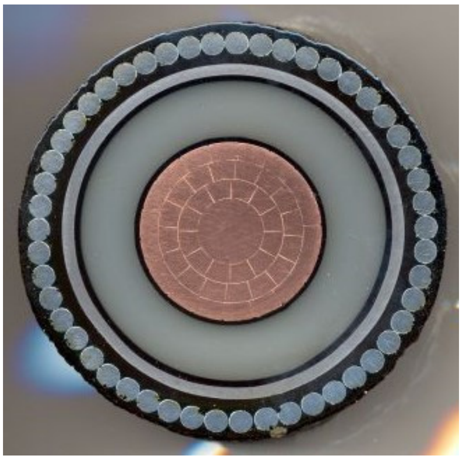

Figure 1-2. XLPE-insulated cable [13].

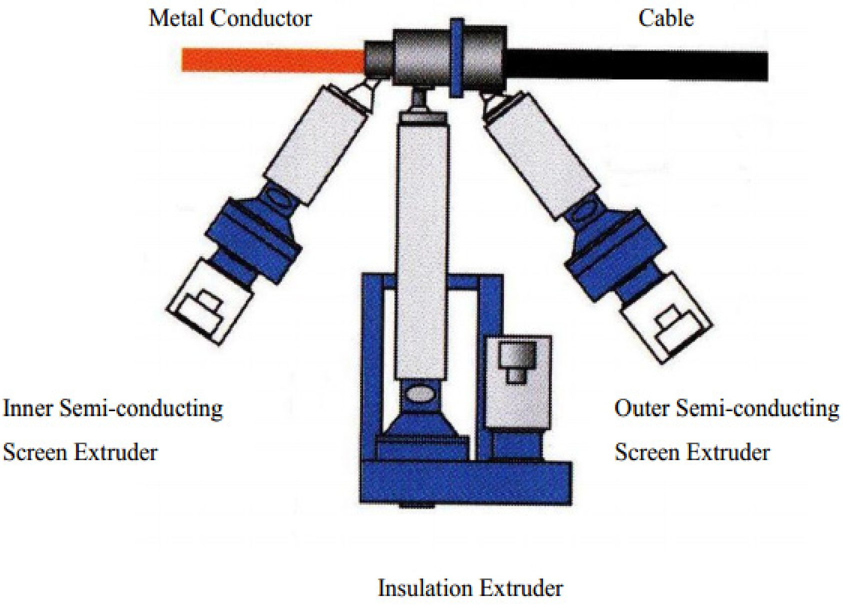

Figure 1-3. The triple extrusion stage for the extruded cable [5].

Up to now, most extruded HVDC cable systems employ XLPE as the main insulation material, and they have been successfully applied in many HVDC projects at up to 300 kV voltage rating and up to 1000 MW power rating [18]. In 2014, a 525 kV HVDC XLPE insulated cable system with a power rating range of up to 2600 MW has been produced by ABB [19], and shortly afterwards, a 640 kV extruded DC cable system with at least 3000 MW power rating is developed by NKT [20]. Recent research also suggests that polypropylene (PP) could be utilized as the insulation material for HVDC cables, due to its high temperature stability and excellent recyclability [21]. Since the PP-based HVDC cables can be manufactured without the crosslinking and degassing processes which cause pollution and energy consumption, as a recyclable thermoplastic polymeric material, PP is becoming a hotspot in the research and development of next generation insulation material for HVDC extruded cables [22] [23] [24]. Prysmian group has launched a new breakthrough HVDC recyclable cable technology of 525 kV based on PP insulation [25]. However, the stiffness and brittleness of PP under low temperature limit its application, and the researchers are still dedicated to improve its mechanical properties, such as by blending with thermoplastic elastomers [26]. In general, the PP-based cable is still not a fully established technology for DC cable systems yet.

The main drawback which limits the performance of HVDC extruded cable systems is, the easy formation of space charge inside the insulation, which can result in localized high electric field, accelerating degradation and ageing processes of insulation material [3] [4] [27]. Moreover, during or shortly after voltage polarity reversal, the presence of space charge can lead to considerable electric field enhancement and may cause permanent failure in the insulation [28]. To understand the issues related to space charge accumulation and meet the requirement for future HVDC cables, the research directions in past decades have been mainly focused on:

1. The development of space charge detection methods, especially considering the thermal impacts.
2. The development of dielectric material with improved electrical, thermal and mechanical properties, such as using additives or nano-fillers.
3. The development of numerical approaches for predicting the material behavior, to study the space charge generation and transport mechanisms in polymeric insulation.

It is generally agreed that the space charge accumulation must be minimized in HVDC cables for improving the performance [5]. Some efforts have been made to suppress the space charge by limiting the charge injection from electrodes, via a modification of the characteristics of the interface between the conductor/insulation [29] [30]. In addition, it is also reported that the properties of the bulk material can be improved by adding additives or nanocomposite fillers [31] [32] [33], and a 500 kV HVDC XLPE cable has been developed based on the homogeneously dispersed nano-sized MgO-filler [34]. The performance of the nanocomposite-filled insulation is not only dependent on the types of nano-particles, but also determined by other complexities, such as size, concentration level, surface treatment, dispersion and moisture [35]. Although the mechanism of nano-filler function is still not fully understood, it can be argued that the trap distribution and the trap depth may be altered by adding nano-fillers into PE-based compounds [5]. Another space charge suppressing method is to improve the cleanliness of XLPE by minimizing the chemical species introduced into XLPE during the manufacturing, and a superior electrical performance XLPE insulated cable with high purity is commercially available for 525 kV HVDC transmission [19].

1.2 Space charge in polymeric insulation material

Polymeric insulation has been successfully used in AC cable technology since 1960s, and now it is still dominating [28]. However, the use of polymeric material for HVDC cables was not as successful. Different attempts had been made to apply this excellent insulating material for manufacturing HVDC cables since four decades ago, and a lot of emphasis was put on the ability of polymeric insulation to withstand the polarity reversal since HVDC converters of the Self-commutated voltage source (VSC) type were in the infant stage and the HVDC systems were dominated by the Line-commutated current source (LCC-CSC) type [28] [36]. Nevertheless, those attempts were aborted and most existing HVDC cables were mass-impregnated or oil-filled cables. It has to be illustrated that, in LCC-CSC systems the power flow direction reversal is achieved by changing the pole voltage polarity since the current flow cannot be reversed. On the contrary, in VSC systems the current flow direction is reversed while the same pole voltage polarity is always maintained to accomplish the power flow reversal [10]. Until 1999, the first commercial HVDC cable system with extruded insulation, the Gotland HVDC link with the VSC technology, was able to be commissioned [37]. Today the design of HVDC extruded cables is still one of the most challenging issues in the cable industry, as the electric field distribution over the insulation thickness can be highly affected by the accumulation of space charge, which can control the cable system behaviour, particularly, its long-term reliability and life expectancy. In fact, space charge can be easily accumulated in the polymeric insulation under DC field, due to charge injection from the electrodes or to ionization of dissociable impurities within the insulation bulk. The accumulated charges can deform the electric field by creating zones of high overstress, and if the space charge density becomes sufficiently high, the local electric field strength may exceed the breakdown strength of the dielectric, leading to dielectric failure. Even if the enhanced field created locally by the trapped charges is not high enough to exceed the breakdown strength, the overstress can still boost the degradation reactions by the electrostatic energy associated with the accumulated charges and cause the formation of weak points in the material, triggering ageing processes [4].

1.2.1 Space charge field

From a macroscopic point of view, insulating materials allow a weak electrical conduction under DC field. This weak flow of charge within the insulation may not be uniform due to a local non-homogeneity of the material, thereby forming space charge. According to the current density continuity equation, when a divergence takes place between the incoming and outgoing charge, charge builds up in this region,

$$\nabla \cdot \vec{j} + \frac{\partial \rho}{\partial t} = 0 \tag{1-1}$$

where j is the current density, ρ is the space charge density and t is the time. According to Gauss' Law, space charge field E_s is associated to a charge distribution:

$$\rho = \nabla \cdot \left(\varepsilon_0 \varepsilon_r \vec{E}_s \right) \tag{1-2}$$

where ε_0 is the vacuum permittivity and ε_r is the relative permittivity of the insulation. Therefore, the electric field E within the cable insulation in the presence of space charge is given by the sum of two contributions: the space charge field E_s and the external field E_0, which is created by the applied voltage,

$$\vec{E} = \vec{E}_S + \vec{E}_0 \tag{1-3}$$

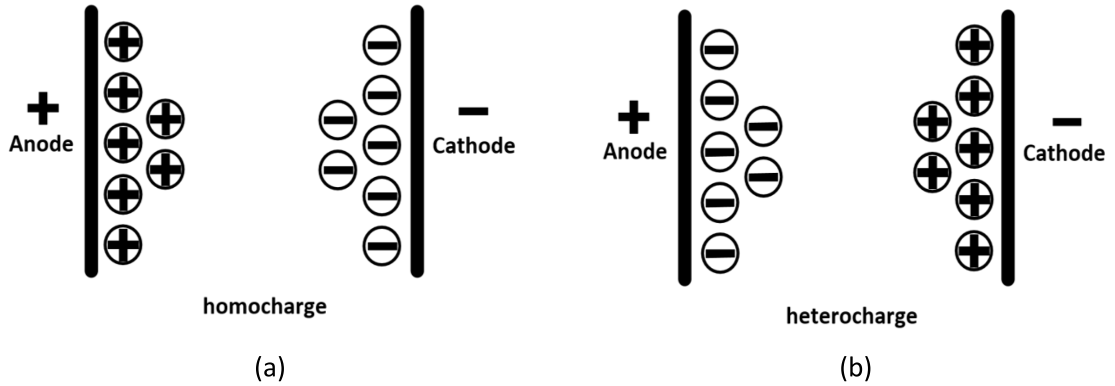

(a) (b)

Figure 1-4. Representation of space charge build-up at the electrodes. (a) homo charge distribution. (b) hetero charge distribution.

With reference to the space charge build-up in the vicinity of the electrodes, two types of space charge distributions are showed in Figures 1-4a and 1-4b. The homo charges have the same polarity as the adjacent electrodes, and is usually due to the trapping of injected charges [38]. As shown in Figure 1-5a, the presence of homo charges can lower the electric field at the interfaces of the electrodes, but enhance the field in the bulk. In contrast, the hetero charges have the opposite polarity to the nearby electrodes, and they are generally believed to be originated from the ionization of the dissociable chemical species present in the insulated material. These species can be introduced during the manufacturing of the material, such as antioxidants, crosslinking by-products, or other additives and impurities [39] [40] [41]. It is also reported that the hetero charge distribution may be due to the injected charge from one electrode partial blocking at another electrode [42]. The build-up of hetero charges can result in enhancing the electric field near the electrodes and a consequent reduction in the middle of the insulation, as presented in Figure 1-5b.

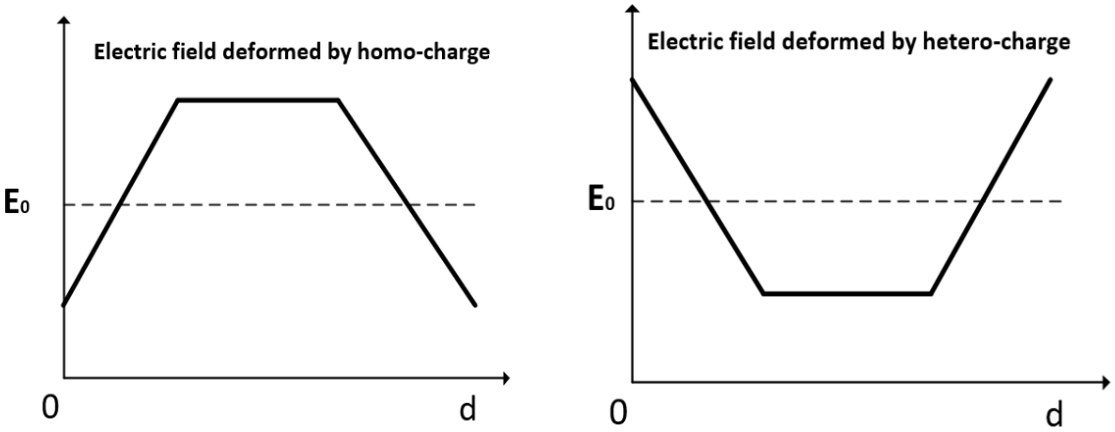

(a) (b)

Figure 1-5. Schematic representation of electric field distribution deformed by space charge. (a) with the presence of homo charges. (b) with the presence of hetero charges.

The accumulated space charge can be released from the insulation when the external field is removed and the insulation is short-circuited. However, this process can last long, depending on the type of insulation and on the temperature. A consequence of this phenomenon is that the accumulated charges will be kept within the insulation when the DC voltage is removed or when the polarity of the external DC voltage changes. In the case of the formation of homo charges in the HVDC cable insulation, when the polarity reversal is operated, the homo charges become hetero charges, and the insulation near the electrodes is suddenly subjected to an extremely high field. This fact has been confirmed by experimental results that presents polarity reversal leads to a reduction in the life of the insulating material [43].

1.2.2 Space charge detection technique

In the past decades, many techniques have been developed for measuring space charge, in order to assess the behaviour of a specific material under different stresses. Following the history, space charge measurement techniques could be simply classified as destructive and non-destructive ones. Early methods of studying space charge distribution in polymers employed destructive techniques, such as Dust Figure Method [44] and Probe Method [45]. The general principle of these techniques is cutting samples into pieces and then detecting the charge distribution characteristic on the surface of slices. However, because the methods involve slicing, the sample preparation procedures can affect the detected results greatly. From the early 1980s to mid-1990s, a number of non-destructive methods have been developed to investigate space charge distribution in solid polymeric materials. The first non-destructive technique for space charge measurement was introduced by Collins [46], from which space charge measurement methods are improved gradually, and they can be generally divided into two categories:

“Thermal methods”: Thermal pulse method (TPM) [47]; Thermal step method (TSM) [48]; Laser intensity modulation method (LIMM) [49].

“Wave propagation methods”: Pulsed electro-acoustic method (PEA) [50]; Laser-induced pressure pulse method (LIPP) [51]; Pressure wave propagation method (PWP) [52].

Table 1-1. Summary and comparisons of space charge detection methods [53].

Group	**Method**	**Disturbance**	**Scan mechanism**	**Detection process**	**Thickness (μm)**	**Resolution (μm)**	**Comments**
Wave propagation	PEA	Force of modulated electric field on charges in samples	Propagation with longitudinal sound velocity	Piezoelectric transducer at bottom electrode	25-20000	1.6-1000	Deconvolution required, also used for surface charge measurement. Better resolution can be achieved by using a pulse voltage of narrow width.
	LIPP	Absorption of short laser light pulse in front electrode	Propagation with longitudinal sound velocity	Current or voltage between sample electrodes	<1000	~1	Deconvolution required. The resolution can be improved by using a femtosecond laser pulse.
	PWP	Absorption of short laser light pulse in metal target	Propagation with longitudinal sound velocity	Current or voltage between sample electrodes	50-1000	10	Resolution improved with deconvolution. Also used for surface charge measurements.
Thermal	TSM	Applying two isothermal sources across the sample	Thermal expansion of the sample	Current between sample electrodes	10-20000	1-150	Deconvolution required, measurements performed on thinner samples require a faster heating. The resolution can reach the order of nm using a femtosecond pulse.
	TPM	Absorption of short light pulse in front electrode	Diffusion according to heat conduction equations	Voltage change across sample	25-200	2.5	Deconvolution required. The resolution can be enhanced by collecting the data from both sides of the sample.
	LIMM	Absorption of modulated light in front electrode	Frequency-dependent steady-state heat profile	Current between sample electrodes	≤100	≥2	Deconvolution required, the resolution can be improved by using a very narrow laser.

Table 1-1 summaries the generally used space charge detection methods, and the most widely used methods at present are the PEA and the TSM techniques, due to their better resolution and wider measuring range. Indeed, the two methods both enable the measurement to be performed over the whole insulation thickness even of full-size power cables. However, the PEA method seems superior overall since it exhibits better performance on time resolution. Actually, the PEA method requires the application of a very short voltage pulse, which can be applied to the samples being tested without interrupting the poling voltage. On the contrary, The TSM method not only needs the application of a thermal step to the specimens, which is more time-consuming for the heat to be delivered from the thermal diffuser to the specimens; but also the HVDC source has to be switched off during the measurement. Hence, one single space charge measurement via the TSM requires a much longer time than one single measurement via the PEA technique. Moreover, the power source has to be disconnected while performing space charge measurement by means of the TSM and resumed thereafter, namely the TSM method is not suitable to observe space charge behaviour continuously in long-term ageing sample test. Compared with the other methods, another main advantage of PEA method is that the high-voltage circuit and the circuit for detecting the pressure wave signal are electrically separated by the ground electrode. In this case, even when dielectric discharge takes place, the ground electrode can protect the amplifier and oscilloscope, and that is why the PEA method is considered as the safest method for studying space charge in samples subjected to high voltage. The details will be illustrated in section 2.3. For the above reasons, considering the resolution, construction cost and measuring range, PEA method is adopted in this study.

1.3 Research gap and objectives

For HVDC cable transmission systems, the trend nowadays is towards XLPE insulated cables with a service temperature of 90°C at the core and a design field of 20 kV/mm [54]. However, space charge accumulation under HVDC stress has been confirmed as one of the major technical problems in the further development of HVDC extruded cable technology. In past two decades, extensive efforts have been made from space charge measurements in order to investigate the space charge behaviour and to understand the relationship between space charge and electrical performance of the dielectrics. Due to potential electrical degradation ageing process triggered by the accumulation space charges, the IEEE standard 1732 was established for measuring space charge in HVDC extruded cables as the qualification tests in 2017 [55]. However, the space charge detection methods cannot distinguish the charge carrier species, and the understanding of the charge generation and transport mechanisms in polymeric insulation is still not fully established. In addition to improve the insulation material properties and minimize space charge effects, numerical modelling is extremely useful to understand and predict material performance. A conductivity model which serves as an important reference for HVDC cable design has been recognized with limited performance, as it lacks descriptions on space charge behaviour [56]. A bipolar charge transport theory, which brings the details of the electronic charge generation and transport mechanisms, has been proposed and successfully applied to analyse the space charge dynamics in polyethylene [57]. However, such model is always utilized for flat specimens, and the extension to coaxial geometry is still missing. Due to the cable geometry factor, the divergent electric field and the temperature gradient can severely affect space charge accumulation [58]. Especially when considering the operation stages of the HVDC cable systems, the space charge behaviour and the transient electric field distribution need to be investigated under the polarity reversal and the thermal transient. Furthermore, most emphasis has been devoted to study the electronic charges injected from the interface of electrode/insulation, although the ionization of dissociable impurities also plays an important role in the space charge accumulation, no attempts have been made to investigate the ionic charge behaviour in the HVDC XLPE cable.

The general objective of the present study is to obtain a better understanding of the space charge behaviour in HVDC extruded cable insulation. The calculation method of space charge and electric field distribution in the DC cable systems will be developed, in order to provide tools and principles to support the design and operation of HVDC extruded cable systems. The following milestones were set for the dissertation:

- The investigation of space charge behaviour in the DC extruded cable in the presence of temperature gradient by employing the bipolar charge transport theory.
- The investigation of polarity reversal and thermal transient effects on electric field distribution in HVDC cable systems.
- The methodology proposed to simulate the hetero charge formation in XLPE by additionally considering the ionization of dissociable impurities.
- The measurement of space charge accumulation in XLPE insulated cables, and the implementation of a model to simulate the space charge behaviour in XLPE insulated cables.

1.4 Contributions of this research

This dissertation contributes to the understanding in space charge behaviour in HVDC extruded cable systems through theoretical modelling and experimental investigations. A threshold electric field at which the charge injection takes place is introduced into the bipolar charge transport model, and the dynamic space charge and field distribution in DC cable insulation in the presence of a temperature gradient are numerically modelled. Compared with the traditional conductivity model, the new approach is superior in calculating the electric field in DC cable systems, since such model provides well descriptions on charge generation and transport mechanisms.

The space charge behaviour and transient field distribution under the operation stages of the HVDC cable systems are first investigated by employing the bipolar charge transport theory. By exploring the electric field variation under the polarity reversal, the modelling approach can provide operational recommendations for HVDC cable systems and assist DC cable design.

The thermal transient effects on the space charge behaviour and the transient field distribution are first investigated by numerical modelling. Due to the temperature dependence of charge generation and transport, it is suggested that different loading conditions need to be considered in designing DC polymeric cables.

By considering the ionization of dissociable impurities in XLPE, the formation and transport of ionic charge carriers are taken into account and fed into the bipolar charge transport model for simulating the hetero charge formation in XLPE. The proposed model can not only contribute to simulate space charge dynamics and field variation in the cable insulation material, but also assist in understanding the mechanisms of charge generation and transport in solid dielectrics.

A pulsed electro-acoustic system for measuring space charge in XLPE cables is designed and built. The space charge measurements have been carried on XLPE insulated cables at room temperature and the obvious hetero charge formation can be detected. Based on the proposed model, it is the first time to simulate the hetero charge formation in XLPE insulated cables by considering the ionic charge carriers.

1.5 Outline of the dissertation

The thesis will be organized as following chapters:

In Chapter 2, the basics of space charge in polymeric insulation material are reviewed, including the charge generation and transport mechanisms, and the principle of the pulsed electro-acoustic method is also described.

In Chapter 3, comparisons of the two models, the conductivity model and the bipolar charge transport model, on calculating the electric field in DC polymeric cable are made. The two models are described respectively and employed to simulate the space charge and field distribution in a medium voltage size DC cable in the presence of a temperature gradient. The advantages and limitations of them are summarized after analyzation of their results compared with the previous experimental work. Simulations of space charge and transient field distribution in DC cable under the voltage polarity reversal are also performed.

In Chapter 4, the thermal transient effects on space charge dynamics in DC cable insulation are investigated by means of the bipolar charge transport theory. The space charge and field distribution in cables subjected to cyclic load are also studied.

In Chapter 5, space charge measurements are taken on LDPE, fresh and degassed XLPE flat specimens separately at room temperature, in order to observe the homo charge and hetero charge formation. A modified model by considering the ionic dissociation of impurities has been proposed and employed to simulate the hetero charge formation in XLPE.

In Chapter 6, the experimental setup of the cable PEA system is described, and the space charge measurements are carried on the XLPE insulated cables at room temperature. The space charge and field distribution in the XLPE insulated cable are also simulated by the proposed modelling approach.

In Chapter 7, the conclusions based on the present work are summarized and some suggestions for the future study are given.

Chapter 2 Space charge mechanisms in HVDC extruded cable and the pulsed electro-acoustic method

In order to achieve the understanding of space charge behaviour in polymeric insulation material, the basics of space charge have to be acknowledged. This chapter first introduces the charge generation mechanisms, and then the classic theories of charge transport are reviewed. Note that the dielectric material focused here is polyethylene, not only due to its simple chemical formulation subjected to many theoretical studies, but also to the main insulation of HVDC extruded cable is polyethylene-based. Apart from these, the space charge detection technique applied in this study is reviewed in detail as well.

2.1 Charge generation

Space charge in polymeric material may originate from the charge injection at the electrodes, or from the ionization process of some dissociable chemical species presenting in the bulk, such as cross-linking by-products, antioxidants and other impurities [38] [40] [41] [59]. Generally, the charge injection processes are responsible for homo charge distribution, while hetero charge formation results from the ionization of the dissociable chemical species or partial blocking of injected charge carriers.

2.1.1 Electronic injection

The injection of charges from the electrodes involves the transfer of electrons (and holes) through the electrode-polymer interface, and such process is highly dependent on the condition of the interface, including the electrode material, the surface defects, the impurity and the oxidation level. The electronic charge injection can always be described by the two mechanisms, the Schottky injection and the Fowler-Nordheim injection [38]. A coulombic potential barrier usually limits the transfer of electrons between electrodes and polymeric insulation, and this barrier can be reduced both in height and width by high electric fields [38]. Due to the combination of the applied field and the image force, the reduction in barrier height enhances the probability that there will be electrons/holes with sufficient thermal energy to overcome it, and this kind of process is called Schottky injection [60]. The other effect of high field is the reduction in width of potential barrier, making the electrons/holes possibly tunnelling through the barrier even with insufficient energy due to the particle-wave duality of electrons/holes, and such mechanism is called Fower-Nordheim injection. It should be noted that the tunnelling effect is only expected to occur at very high electric field (over 10^9 V/m) [61], and therefore in this study towards HVDC cable application the Schottky injection is considered to be the primary form.

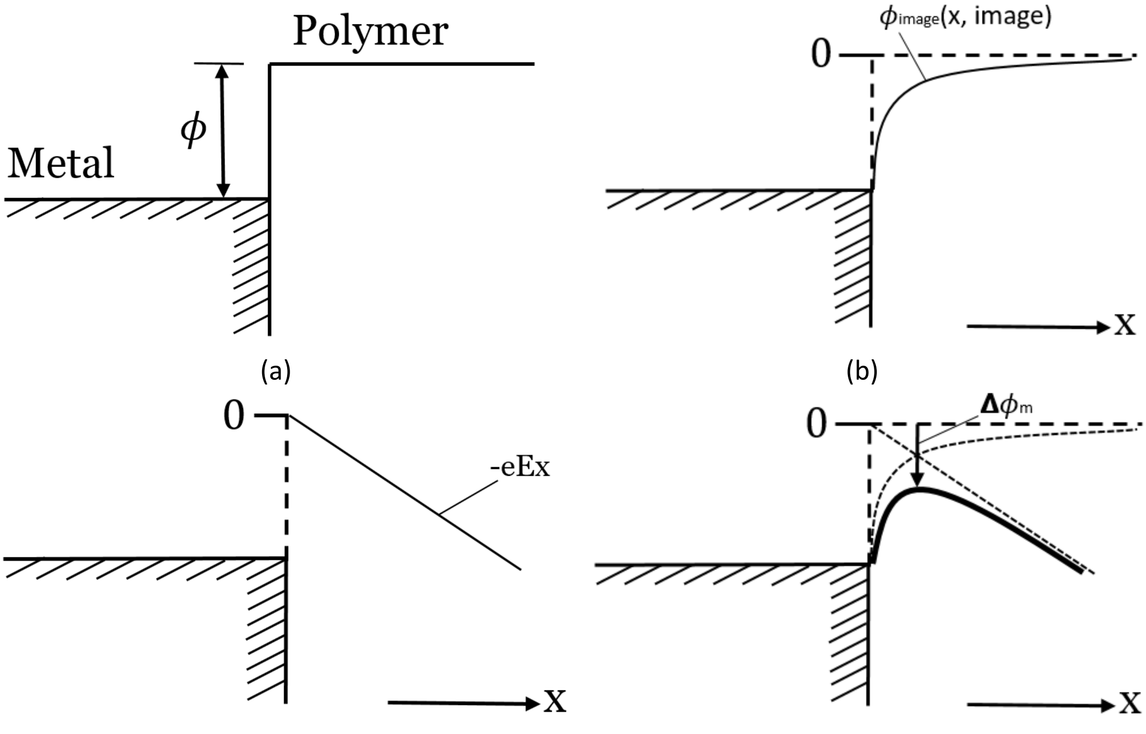

(a) (b) (c) (d)

Figure 2-1. Modification of the coulombic potential barrier at a metal-polymer interface by an applied electric field *E*, as a function of the distance of the electron from the interface, *x*: (a) total barrier height; (b) shape of barrier including effect of coulombic image force; (c) potential energy due to applied electric field; (d) total barrier shape [38].

Based on the simple electron energy-band diagram shown in Figure 2-1, the coulombic potential barrier at the interface prevents the injection of electrons from the metal into the insulator. The barrier height depends on the interface, and in the case of metal/polymer, the height of barrier, ϕ, is dependent on the metal-insulation work function difference and local conditions of electrical polarization [38]. When an electric field *E* is applied, the barrier height could be reduced by the applied field and the image force effect so that enhanced electron injection can take place at the interface, resulting in a reduced potential barrier of the form [38]:

$$\phi(x) = \phi - \frac{e^2}{16\pi\varepsilon_0\varepsilon_r x} - eEx \tag{2-1}$$

where *x* is the distance of electron from the interface, *e* is the elementary charge; ε_0 is the vacuum permittivity and ε_r is the relative dielectric permittivity. The image force tends to attract the emitted electrons back to the metal, while the driving force due to the applied field tends to drives the emitted electrons away from the metal. There is an optimal point where the net force acting on the electrons is zero and the potential barrier height becomes maxima. By setting the differential of the potential barrier height as a function of distance is zero, the optimal point x_m is obtained [38]:

$$x_m = \sqrt{\frac{e}{16\pi\varepsilon_0\varepsilon_r E}} \tag{2-2}$$

At the optimal point x_m, the lowering potential barrier height $\Delta\phi_m$ can be calculated as [38]:

$$\Delta\phi_m = \sqrt{\frac{e^3 E}{4\pi\varepsilon_0\varepsilon_r}} \tag{2-3}$$

Therefore, the effective potential barrier height can be expressed as [38]:

$$\phi_{eff} = \phi - \sqrt{\frac{e^3 E}{4\pi\varepsilon_0\varepsilon_r}} \tag{2-4}$$

In accordance with the Richardson-Dushman equation, the emitted current density J at temperature T is of the form [38]:

$$J = AT^2 \exp\left(-\frac{\psi}{k_B T}\right) \tag{2-5}$$

where A is the Richardson constant (1.2×10^6 A/m^2/K^2), k_B is the Boltzmann constant, ψ is the potential barrier height (eV). By introducing the expression of the effective potential barrier height, the Richardson-Schottky law of electron injection from metal into insulator is obtained by [60]:

$$J = AT^2 \exp\left(-\frac{\phi}{k_B T}\right) \exp\left(\frac{1}{k_B T}\sqrt{\frac{e^3 E}{4\pi\varepsilon_0\varepsilon_r}}\right) \tag{2-6}$$

It should be noted that, the above Schottky injection current takes place at a metal-polymer interface. However, indeed, there is always a semicon layer between the metal and the insulator whether in HVDC extruded cable systems or in the space charge measurement system. When considering the interface between the semi-conductive electrodes and the polymeric insulation, it still can be assumed that such potential barrier exists due to work function difference, as the semicon layer can be treated as a conductive medium compared with the polymeric insulation.

2.1.2 Ionic process

Insulating polymeric material may contain ions, groups capable of ionizing, or groups into which ionic material have been introduced [38]. In most insulating material, water is always a source of ions. It is generally not easy to identify the ions experimentally in solid polymers, but it is reasonable to assume that they are derived mainly from fragments of polymerization catalyst, degradation and dissociation products of polymer itself, absorbed water, and other impurities introduced into the polymer during the fabrication process, such as cross-linking by-products [60]. For example, if *AB* molecules are the only dissociable species present in the material, and a molecule *AB* can be dissociated into A^+ and B^- ions, as expressed following,

$$AB \underset{recombination}{\overset{dissociation}{\rightleftarrows}} A^{+} + B^{-} \tag{2-7}$$

In thermal equilibrium, the relationship between the concentration of generated ions and the neutral ion-pairs can be expressed as [60]:

$$cK_D = n_{\pm 0}^2 K_R \tag{2-8}$$

where c is the density of the neutral ion-pairs; $n_{\pm 0}$ is the equilibrium free ion concentrations; K_D and K_R are the dissociation and recombination rate respectively. The dissociation is a thermally activated process, and therefore K_D can be written as [60]:

$$K_D = K_{D0} \exp\left(\frac{-E_D}{\varepsilon_0 \varepsilon_r kT}\right) \tag{2-9}$$

where K_{D0} is a constant, E_D is the activation energy for dissociation. The recombination rate K_R is related to ionic species mobility and is of the Langevin form [60],

$$K_R = \frac{(\mu_+ + \mu_-)}{\varepsilon_0 \varepsilon_r} \tag{2-10}$$

where μ_+ and μ_- are the mobility of free positive and negative ions respectively. The positively charged cations moving toward the cathode and the negatively charged anions moving toward the anode under an applied field will create hetero charges near the electrodes, deforming the electric field. The accumulated hetero charges may trigger the injection of electrons from the cathode or holes from the anode when the amount of them reaches a certain critical value [60].

2.2 Charge transport

Charge transport in insulating polymers is very complicated and depends primarily on the nature of charge carriers. Furthermore, the conduction demonstrates different field dependence over a specific range of electric fields. It is also believed that the impurities and defects contribute to the conduction processes. Therefore, charge conduction is not an elementary mechanism but consists of different transport mechanisms. There are several basic theories describing the charge transport in insulating materials, such as hopping conduction, Poole-Frenkel mechanism and space charge limited current theory (SCLC), which are presented below.

2.2.1 Hopping conduction

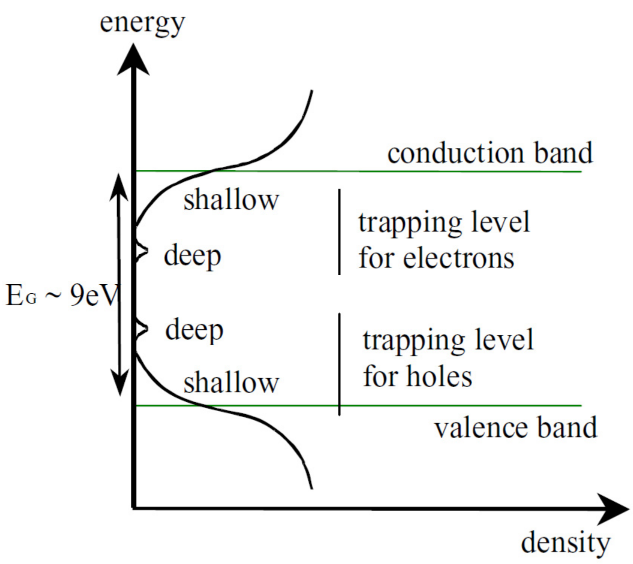

Figure 2-2. Schematic representation of state density in a disordered dielectric material. Shallow and deep traps are related to physical and chemical disorder respectively [62].

Polyethylene is considered to be a wide band-gap material, and the value of the forbidden gap as derived from calculation or experimental measurements is of the order of 8.8 eV [63], which implies polyethylene would have an intrinsic conductivity of 10^{-45} s/m [64]. However, this level of conductivity has never been measured as the reality of polyethylene is much more complex than the idealized band diagram, as present in Figure 2-2 [62]. Indeed, polyethylene molecules may have different conformations, which introducing “disorders” into the supramolecular organization, such as physical, conformational or topological disorders [62]. Consequently, the local disorder of chain segments creates localized energy states on the either side of the forbidden gap, which are accessible for charge carriers and are always referred to as “shallow traps” due to their typical energy level of less than 0.3 eV [65]. Additionally, in polyethylene, chemical defects can be found due to side chains, additives, reaction products and impurities, which introduces additional energy levels in the forbidden gap, generally at a deeper energy level of 1 eV [65]. Such “deep traps” related to the chemical disorder are believed to restrict charge transport, while the “shallow traps” are considered to assist the conduction process. In hopping conduction mechanism, it is assumed that a series of single level trap sites with an energy of φ are localized in the band gap of polymers, and the electrons trapped in these sites may jump over the potential barrier with a separation average distance d_a by receiving thermal excitation [38]. The probability of electrons hopping over the traps in the absence of electric field can be described as [38]:

$$P = v \cdot \exp\left(-\frac{\varphi}{k_B T}\right) \tag{2-11}$$

where v is the attempt-to-escape frequency in the order of 10^{12} to 10^{14} s^{-1}. When an electric field E is applied, the potential barrier will tilt down in the direction of electric field, as presented in Figure 2-3. The barrier height will be elevated along the field direction by term $+1/2qd_aE$ and will be reduced against electric field by $-1/2qd_aE$.

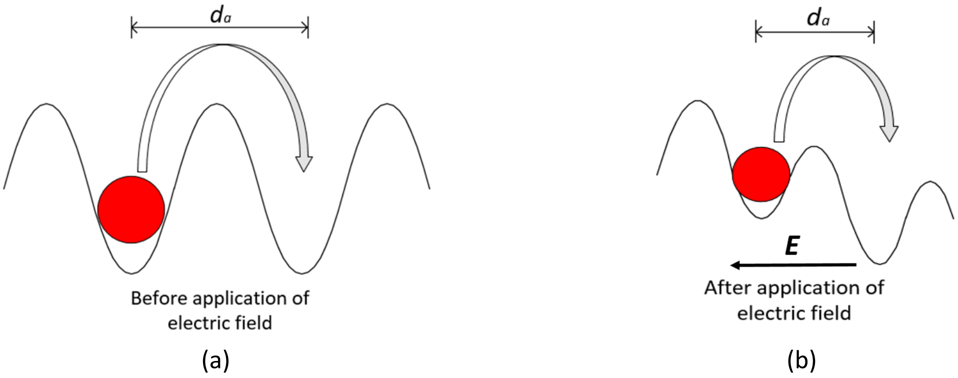

Figure 2-3: Schematic representation of hopping conduction: (a) before the application of electric field; (b) after the application of electric field [60].

Therefore, the net probability of charge carrier movement in the direction of electric field is given by:

$$\begin{aligned} P(E) &= v \cdot \exp\left(-\frac{\varphi - \frac{1}{2}qd_aE}{k_BT}\right) - v \cdot \exp\left(-\frac{\varphi + \frac{1}{2}qd_aE}{k_BT}\right) \\ &= v \cdot \exp\left(-\frac{\varphi}{k_BT}\right)\left[\exp\left(\frac{qd_aE}{2k_BT}\right) - \exp\left(\frac{-qd_aE}{2k_BT}\right)\right] \\ &= 2v \cdot \exp\left(-\frac{\varphi}{k_BT}\right)\sinh\left(\frac{qd_aE}{2k_BT}\right) \end{aligned} \tag{2-12}$$

and the hopping mobility of charge carriers can be expressed as [66]:

$$\mu = P(E)d_a/E = \frac{2d_av}{E} \cdot \exp\left(-\frac{\varphi}{k_BT}\right)\sinh\left(\frac{qd_aE}{2k_BT}\right) \tag{2-13}$$

hence the current density contributed by the hopping mechanism is of the form:

$$J = \mu nqE = 2qnvd_a \cdot \exp\left(-\frac{\varphi}{k_BT}\right)\sinh\left(\frac{qd_aE}{2k_BT}\right) \tag{2-14}$$

where q is the electronic unit charge; n is the concentration of charge carriers.

2.2.2 Poole-Frenkel mechanism

The Poole-Frenkel mechanism within the insulation bulk can be argued that it resembles the Schottky effect at the electrode-insulation interface [38], which has been introduced in section 2.1.1. According to this mechanism, the electric field E reduces the height of barriers that localize charge carriers within the insulation. The lowering of potential barrier by the Poole-Frenkel effect is double of which by the Schottky effect, as the coulombic force in the Poole-Frenkel effect exists between the electron and the ionised donor, instead of which is due to the image charge in the Schottky effect. The reduced barrier height has the form of [38],

$$\phi_{eff} = E_p - \Delta\varphi_p = E_p - 2\sqrt{\frac{q^3 E}{4\pi\varepsilon_0\varepsilon_r}} \tag{2-15}$$

where E_p is the potential barrier height in the absence of electric field, and the Poole-Frenkel expression of conductivity is of the form [38],

$$\sigma = \sigma_0 \exp\left(-\frac{E_p}{2k_B T}\right)\exp\left(\frac{1}{k_B T}\sqrt{\frac{q^3 E}{4\pi\varepsilon_0\varepsilon_r}}\right) \tag{2-16}$$

where $\sigma_0 \exp\left(-\frac{E_p}{2k_B T}\right)$ is defined as the low-field conductivity of the insulating material.

2.2.3 Space charge limited current

Space charge limited current (SCLC) is generally found in insulating thin films, and such theory is commonly based on an energy band diagram with traps [38]. In this theory, the discussion is illustrated in two parts: first the case of an ideal dielectric without traps will be considered, and the other case with traps.

For the trap-free dielectric, several assumptions are made as following:

- No thermally generated charge carriers (the charge source is only from injection);
- Ohmic contacts implying good injection;
- Only one type of charge carriers injected (electrons or holes);

The total current density in the dielectric is made up of the three components of drift, diffusion and displacement [38]:

$$J = \mu_e n_e qE - qD_n \frac{dn_e}{dx} + \varepsilon_0\varepsilon_r \frac{dE}{dt} \tag{2-17}$$

where n_e and μ_e are the density and mobility of electrons, D_n is the Fick's diffusion coefficient and E is the applied field, assuming steady-state conditions then $\frac{dE}{dt} = 0$, and the equation becomes:

$$J = \mu_e n_e qE - qD_n \frac{dn_e}{dx} \tag{2-18}$$

Recalling Poisson's equation and replacing the term n_e:

$$\frac{dE}{dx} = \frac{n_e q}{\varepsilon_0 \varepsilon_r} \tag{2-19}$$

$$J = \varepsilon_0 \varepsilon_r \mu_e E \frac{dE}{dx} - \varepsilon_0 \varepsilon_r D_n \frac{d^2 E}{dx^2} \tag{2-20}$$

Assuming that the space charge concentration to be constant within the whole bulk, then the diffusion term can be neglected:

$$J = \varepsilon_0 \varepsilon_r \mu_e E \frac{dE}{dx} \tag{2-21}$$

Integrating on both sides, and rearranging the equation, then the electric field E can be obtained:

$$E = \sqrt{\frac{2J}{\varepsilon_0 \varepsilon_r \mu_e}(x + x_0)} \tag{2-22}$$

where *x₀* is a constant of integration, and it is assumed to be much smaller than the sample thickness *d*. Integrating the above equation, that is, $V = \int_0^d E dx$, thus the relationship of the current density to voltage can be expressed as [38]:

$$J = \frac{9\varepsilon_0 \varepsilon_r \mu_e V^2}{8d^3} \tag{2-23}$$

The current is proportional to the square of the voltage and this is known as the Mott & Gurney square law [38]. The charge density in the dielectric is made up of two components, the intrinsic charge density and the injection term, therefore the current density can be thought of as being made up of two components as well, as expressed:

$$J = n_0 q \mu_e \frac{V}{d} (Ohmic\ contribution) + \frac{9\varepsilon_0 \varepsilon_r \mu_e V^2}{8d^3} (SCLC\ contribution) \tag{2-24}$$

where n_0 is the density of electrons intrinsic to the insulator. However, for the dielectric with traps, although all the injected electrons contribute to the space charge formation, only a portion of charge carriers contributes to the current due to the existence of trapping charge. Therefore, a fraction coefficient $\theta = n_c / n_t$ is taken into account, where n_c is the free charge density and n_t is the total charge density. Hence the current density can be reproduced as:

$$J = n_0 q \mu_e \frac{V}{d} + \theta \frac{9\varepsilon_0 \varepsilon_r \mu_e V^2}{8d^3} \tag{2-25}$$

The SCLC behaviour can be schematically described in Figure 2-4 [38]. The first region, labelled as Region 1, is dominated by Ohmic's law, i.e. the first component in equation 2-25. In the Region 2, when the applied voltage exceeds the V_{tr}, defined as the transition voltage above which the space-charge-limited contribution overwhelms the ohmic current, the SCLC behaviour is trap-limited, i.e. the second term in equation 2-25. As the voltage is raised to the so-called trap-filled limit, V_{TFL}, all the traps are filled and consequently the current increases at an infinitely fast rate with voltage, as shown in Region 3. Once the traps are filled and the fraction coefficient θ=1, the *J*-*V* characteristic curve with follow the trap-free SCLC relationship, as described in equation 2-24, when the applied voltage keeps increasing into Region 4.

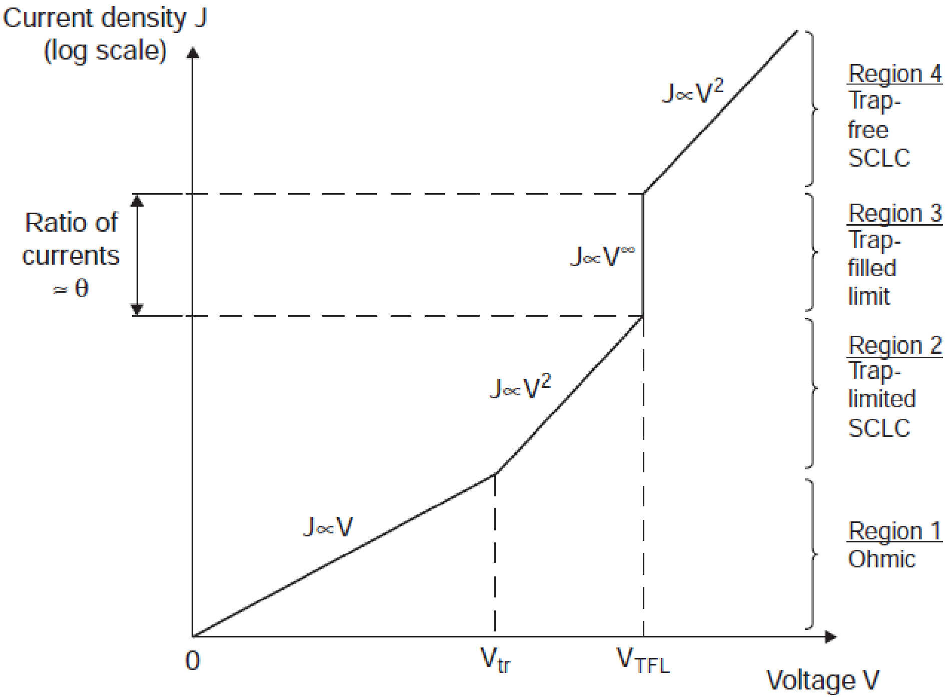

Figure 2-4. Schematic graph of an ideal space charge limited current behaviour [38].

Indeed, the energy levels of traps are broadly distributed, thus the trap-filled limit is not well defined, thereby the distinction between regions 2 and 3 is fuzzy in practice [38]. Since the current increases rapidly during region 3, breakdown usually takes place before the last region is reached. In general, SCLC holds in thin insulating films and depends strongly on insulation thickness [5].

2.3 Pulsed electro-acoustic method (PEA)

The pulsed electro-acoustic (PEA) method was first developed in 1983 by Takada el al. [50], then it has been improved gradually and widely used in academic research to investigate space charge in dielectric materials. As a mature space charge detection method, the PEA method plays an important role in measuring space charge distribution and understanding the electrical properties of dielectric materials.

2.3.1 The principle of PEA method

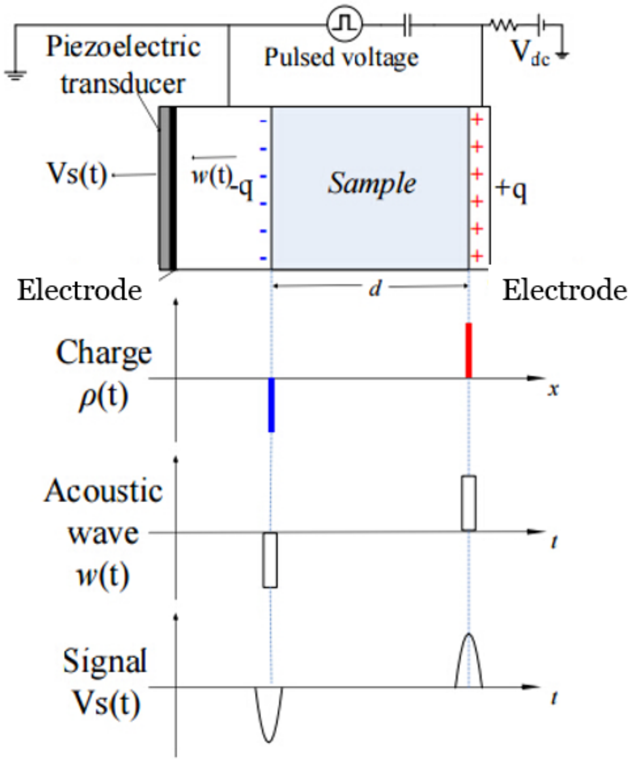

Figure 2-5. Basic principle of the PEA method [67].

The principle of the PEA method is based on the Coulomb force law ($\vec{F} = q\vec{E}$). An externally applied pulse electric field induces a perturbing force in the material in the presence of accumulated charge. The disturbance generates acoustic waves which propagate through the bulk. Then they will be detected by a piezoelectric transducer attached on one of the electrodes, which can convert the acoustic signals into electrical ones. The amplitude of the detected signals will be proportional to the charge amount and the time delay indicates the distance from the sensor, i.e. the position of the charge. These signals are amplified and transferred to an oscilloscope. After the appropriate calibration processing and mathematic treatment, the space charge distribution in the specimen can be obtained. The basic principle of the PEA method is illustrated in Figure 2-5 [67].

A typical measurement apparatus of the PEA system is presented in Figure 2-6 [68], which is mainly composed of following parts. The top and ground electrode systems, at which the dielectric specimen is sandwiched. Note that when the DC and pulse voltages are applied to the sample, a semi-conductive layer is usually inserted between the sample and the upper electrode to improve the acoustic impedance matching. A DC voltage and a pulse voltage are applied from the top electrode to the specimen via a protecting resistor (in the order of 10 kΩ) and a coupling capacitor (in the order of nF), respectively. A thin polyvinylidene fluoride (PVDF) film is usually used for the piezo-transducer, which is attached on the bottom surface of ground electrode, detecting the pressure wave and then transferring into electrical signals. Moreover, in order to prevent the acoustic reflection at the end of transducer, an absorber is placed beneath the transducer. An amplifier is closely linked to the piezo-transducer since the output voltage signal is usually very small. In addition, an electrically shielding box is needed to cover the detecting circuit, aiming to minimize any noise. Finally, the amplified voltage signal can be observed by using an oscilloscope, and be further calibrated by a digital signal processing.

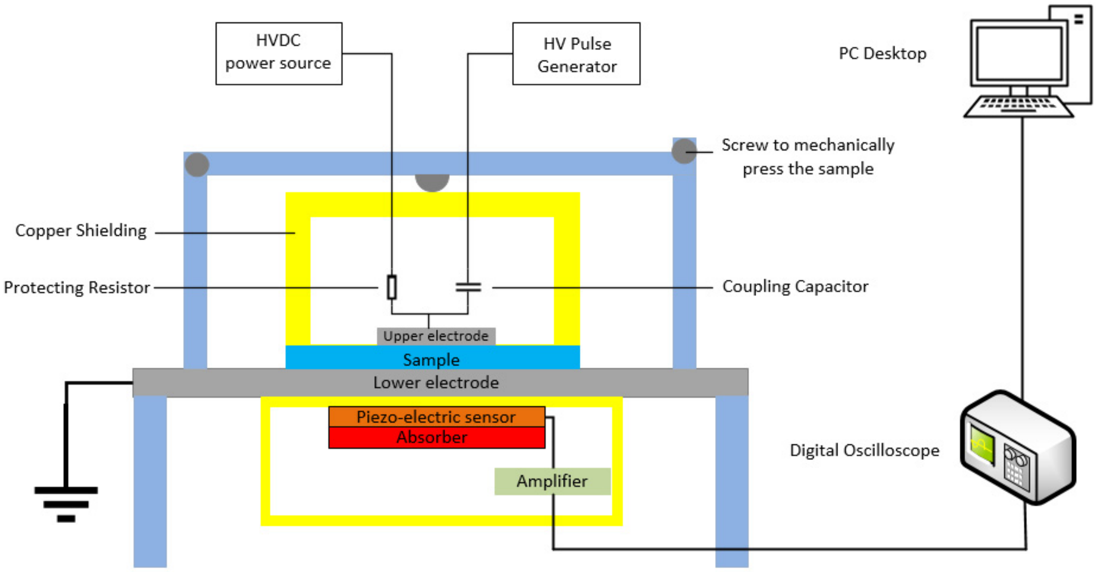

Figure 2-6. A typical PEA measurement system [68].

2.3.2 Modified PEA system for cables

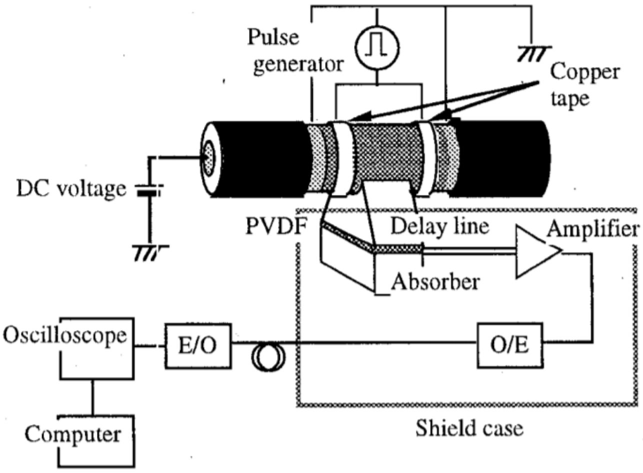

Figure 2-7. Space charge measurement system with the PEA method for cables [69].

The measurement of space charge in the cable insulation is fundamental in the development of HVDC extruded cables, since space charge accumulation distorts the field distribution severely under DC voltage. The first space charge measurement in a coaxial cable by the PEA method was carried out by Fukunaga et al [70], through a system similar to that shown in Figure 2-7 [69], where the ground electrode is of a coaxial structure, providing a close contact between the cable and the electrode, and a piezo-transducer of PVDF is tightly wound around the coaxial-shaped electrode in order to prevent acoustic wave reflection at the interface. Hozumi et al. successfully observed the accumulation of hetero-charges in an XLPE cable of 3 mm thickness by using such cable PEA systems, as presented in Figure 2-8 [71].

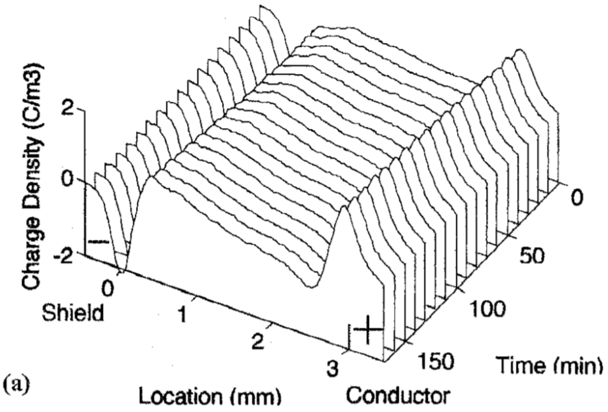

Figure 2-8. Space charge profile evolving with time measured in a 3 mm thick XLPE cable insulation when +70 kV DC voltage was applied [71].

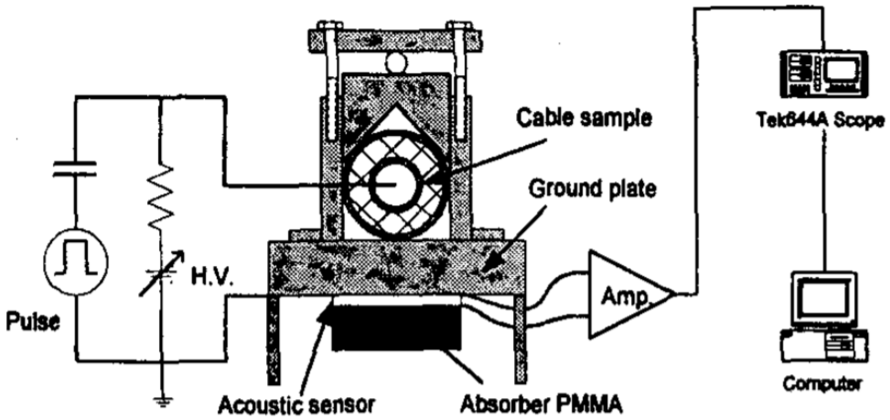

Figure 2-9. Schematic diagram of modified cable PEA system with flat ground electrode [72].

However, a possible limitation to this application is that the measurement system is only suitable to a specific diameter of cables. Fu et al. proposed a solution of replacing the curved cell by introducing a flat ground electrode, as presented in Figure 2-9, and in this way, the improved system can be used to measure space charge in cables of different sizes [72] [73]. To further investigate the space charge behaviour in XLPE cable in practical situations, the induced-current heating technique was introduced by Bodega et al, and the schematic diagram is represented in Figure 2-10 [74]. By means of a current transformer, an AC current is induced in the cable conductor, and a temperature gradient can be formed across the cable insulation due to the Joule losses. By using this technique, the effect of temperature gradient on space charge accumulation in medium-size XLPE insulated cables has been investigated by Fabiani et al., and the results indicated that the temperature gradient of 20 °C greatly contributed to the charge accumulation at an electric field of 20 kV/mm, even leading to the field inversion [75].

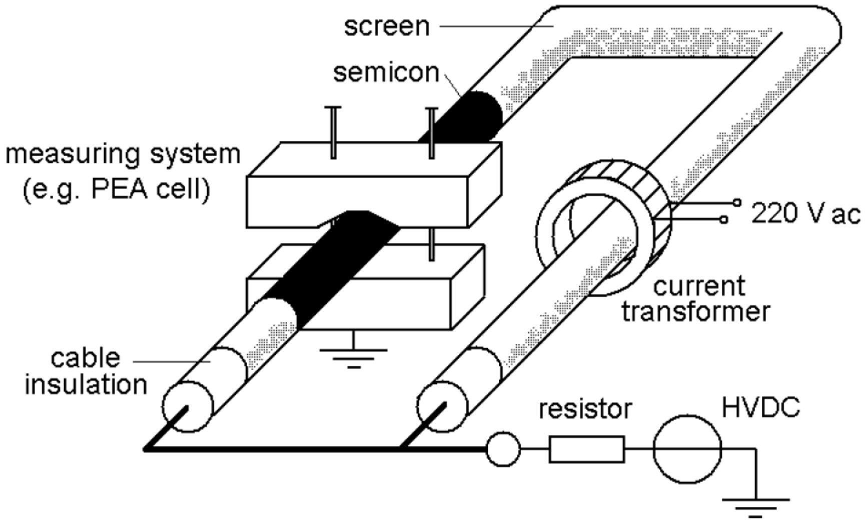

Figure 2-10: Schematic representation of the induced-current heating technique [74].

However, there are still several limitations of the cable PEA systems. Due to the great complexity of the signal processing, it is necessary to consider the divergence of the voltage pulse and of acoustic wave across the insulation, in order to get an accurate space charge profile. Particularly, the acoustic wave can be highly attenuated and distorted due to the large thickness of insulation under test. The grounding system requires particular care in order to avoid spurious signals in the output waveform. In addition, for space charge measurement in full-size cables, the outer tape and screen along the measuring area must be removed.

2.3.3 Space charge waveform recovery method

Generally, the PEA signal collected by the oscilloscope does not directly represent the space charge distribution in samples. In fact, the output waveform can be distorted due to the frequency response of the piezo-transducer and amplifier, which two in series operates as a high-pass filter with a cut-off frequency that may lie in the range of the frequency content of the acoustic signal, as shown in Figure 2-11, where U_P is the output voltage signal produced by the transducer; C_T is the static capacitance of the transducer (in the order of nF); R_A is the input impedance of the amplifier (50 Ω).

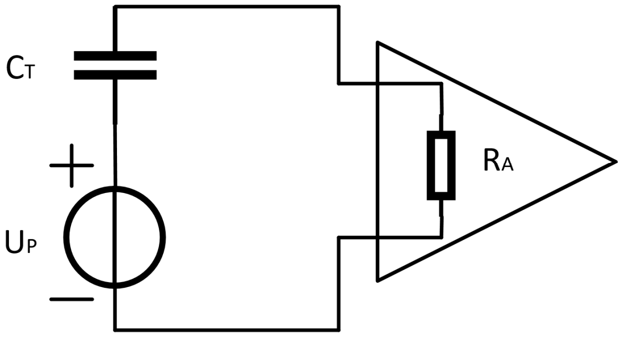

Figure 2-11. Simplified circuit consists of piezoelectric sensor and amplifier.

The capacitor C_T and the resistor R_A compose a high pass filter circuit, and its cut-off frequency can be presented as following:

$$f_c = \frac{1}{2\pi R_A C_T} \tag{2-26}$$

Due to the limitation of frequency response of the detection circuit, the distorted output signal could be mistaken as space charge formation inside the sample. For example, a positive overshoot peak following the induced charge peak at the electrode could not be the result of real measured hetero charge accumulation, but of the frequency response of the measurement system, as shown in Figure 2-12a [76] [77]. Therefore, a deconvolution technique is used to obtain the transfer function of the PEA system and recover the space charge signals. The calibrated space charge profile is shown in Figure 2-12b.

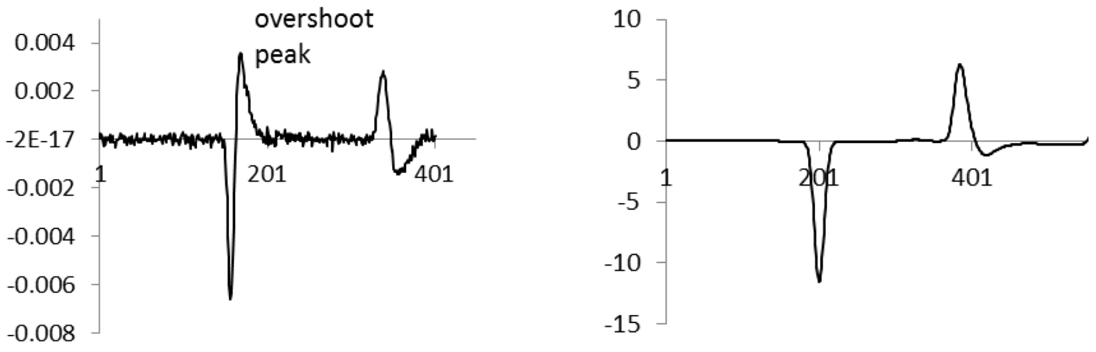

(a) (b)

Figure 2-12. (a) A Typical PEA output signal. (b) The space charge profile after calibration [77].

Since the distortion of the signal is a kind of systematic error of the measurement system, the obtained voltage signal $r_s(t)$ is described as the following convolution of the impulse response of the system $h(t)$ and the charge distribution $x(t)$:

$$r_s(t) = h(t) \times x(t) = \int_{-\infty}^{+\infty} h(t-\tau)x(\tau)d\tau \tag{2-27}$$

Therefore, by obtaining the impulse response *h(t)*, the charge distribution is calculated using the so-called "deconvolution" technique. In frequency domain, the above equation can be expressed as following:

$$R_S(\omega) = X(\omega) \times H(\omega) \tag{2-28}$$

where $R_S(\omega)$, $X(\omega)$ and $H(\omega)$ are Fourier transforms of $r_s(t)$, $x(t)$, and $h(t)$ in frequency domain respectively. In general, $H(\omega)$ is called a "transfer function" of the measurement system, and this function could be evaluated when a relatively low DC electric stress (reference voltage) is applied to the sample over a short duration of time to ensure no space charge accumulates inside the insulation. Under this reference voltage, the signal derived from the induced charge on the electrode can be treated as an impulse (delta function) $x_0(t)$, and the signal itself is the impulse response of the measurement system. The data is called a "reference signal" $r_0(t)$, and should be composed of two same shape peak. However, the pressure wave generated at the upper electrode might be distorted during propagation through the sample by attenuation or dispersion, thus the signal derived from the lower ground electrode is adequate for calibration.

Fast Fourier Transform (FFT) is applied on the impulse function $x_0(t)$ at the outer electrode interface and the reference signal $r_0(t)$ from the induced charge, as shown below:

$$X_0(\omega) = \int_{-\infty}^{+\infty} x_0(t)e^{-j\omega t}dt = FFT[x_0(t)] \tag{2-29}$$

$$R_0(\omega) = \int_{-\infty}^{+\infty} r_0(t)e^{-jwt}dt = FFT[r_0(t)] \tag{2-30}$$

Thus, the transfer function of the system can be obtained in the frequency domain as:

$$H(\omega) = \frac{R_0(\omega)}{X_0(\omega)} \tag{2-31}$$

Consequently, the charge density in frequency domain X(ω) can be given as:

$$X(\omega) = \frac{R_S(\omega)}{H(\omega)} \tag{2-32}$$

Finally, by applying Inverse Fast Fourier Transform (IFFT) on $X(\omega)$, the space charge distribution over the sample thickness can be obtained.

However, when considering the coaxial geometry of cable samples, the measured signal could be affected due to divergence of the pulse electric stress and the acoustic wave transmission, as illustrated in Figure 2-13 [78]. The non-uniform pulse electric stress and the divergent pressure wave will distort the real space charge distribution. Furthermore, attenuation and dispersion of acoustic wave may occur during the propagation through the thick insulation of polymeric material. The detected acoustic wave signals at the piezoelectric transducer could be affected by the above factors, and the compensations and corrections to them need to be considered.

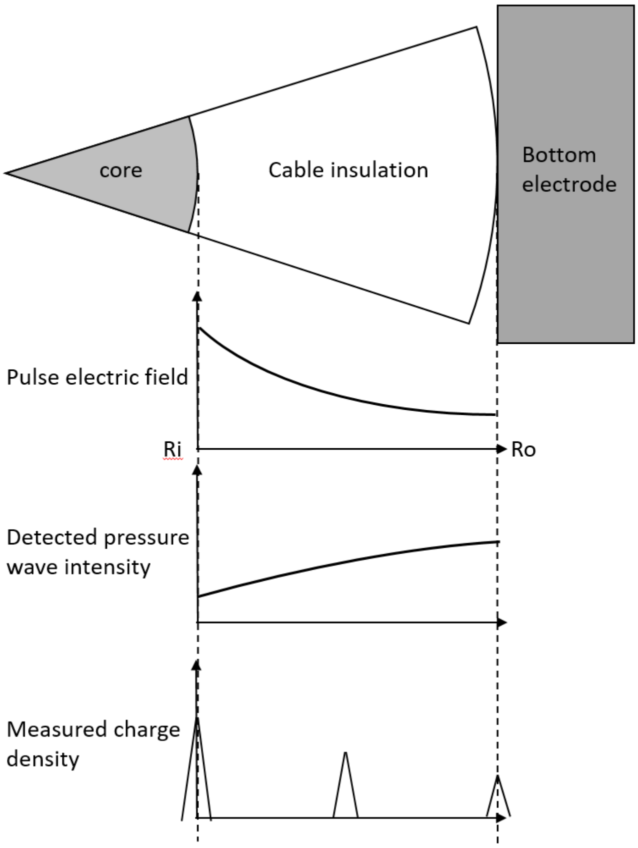

Figure 2-13. Schematic representation of pressure wave propagation in coaxial cable (not to scale) [78].

The pulsed electric field e_p across the cable insulation can be given by:

$$e_p(t,r) = \frac{v_p(t)}{r\ln\left(\frac{b}{a}\right)} \tag{2-33}$$

where a and b are the inner and outer radii of the cable insulation respectively and v_p is the applied pulse voltage. The above equation indicates that the pulsed electric stress decreases across the insulation from the inner to the outer electrode. With the variation of the pulsed electric stress, the space charge density near the inner electrode will induce a higher acoustic signal than that close to the outer. The acoustic wave propagation equation in cylindrical coordinate is presented as:

$$\frac{1}{{u_s}^2}\frac{\partial^2\phi_s(t,r)}{\partial t^2}=\frac{\partial^2\phi_s(t,r)}{\partial r^2}+\frac{1}{r}\frac{\partial\phi_s(t,r)}{\partial r} \tag{2-34}$$

where the u_s is the velocity of acoustic wave; ϕ_s is the velocity potential of vibrating motion in the medium. The solution of the above equation is:

$$\phi_s(t,r)=\frac{A_0}{\sqrt{r}}e^{jk(r-u_s t)} \tag{2-35}$$

where A_0 is a constant which is determined by the boundary condition; $k=\omega/u_s$, and ω is the angular frequency of the acoustic wave. Therefore, the pressure wave per unit area at position *r* is [79]:

$$p(t,r)=\rho_s\frac{\partial\phi_s(t,r)}{\partial t}=-\frac{j\rho_s u_s A_0 k}{\sqrt{r}}e^{jk(r-u_s t)} \tag{2-36}$$

where ρ_s is the density of medium. This equation describes the propagation of an acoustic wave in an elastic medium in the radial direction, indicating the amplitude of the pressure wave generated by the space charge should decrease along the radial direction when it travels to the outer sheath. The factor can be described by the following equation:

$$\frac{p(t+\Delta t,b)}{p(t,r)}=\left(\frac{r}{b}\right)^{\frac{1}{2}} \tag{2-37}$$

where $p(t,r)$ and $p(t+\Delta t,b)$ are the the acoustic waves produced at position *r* and detected at the outer sheath *b*, and Δt is the time of the acoustic wave travelling from position *r* to *b*.

Assume that there are two charge layers with the same density at the inner and the outer electrode respectively. The acoustic wave pressure produced at the inner electrode is (b/a) times bigger than that at the outer electrode due to the divergent pulsed electric stress. Moreover, the detected wave pressure at the sensor, which is generated at the inner electrode, is $(a/b)^{1/2}$ times to its original value because of the acoustic transmission divergence. Therefore, the detected charge density at the inner electrode is $(b/a)^{1/2}$ bigger than which at the outer electrode. Consequently, the signal after the deconvolution must be corrected by the geometry factor $(b/r)^{1/2}$, where *r* lies between the inner and the outer radius [80].

In addition, attenuation and dispersion of waves may occur when acoustic waves propagate through the cable sample. In the linear visco-elastic medium, the wave number *k* should be replaced by its complex form of:

$$k(j\omega)=\beta(\omega)-j\alpha(\omega) \tag{2-38}$$

where α and β are defined as the attenuation and dispersion factor respectively. By application of the Fourier transform, the acoustic wave pressure can be presented as:

$$P(\omega,r)=P(\omega,a)e^{-\alpha(w)(r-a)}e^{-j\beta(\omega)(r-a)} \tag{2-39}$$

where *P(ω,r)* and *P(ω,a)* are the Fourier transforms of the acoustic wave at the position *r* and at the inner radius *a* respectively; *(r-a)* is the distance between the position in the insulation bulk and the inner electrode. The attenuation coefficient *α(ω)* and the dispersion coefficient *β(ω)* are satisfied as [78]:

$$\alpha(\omega)=-\frac{1}{b-a}\ln\left|\frac{P(\omega,b)}{P(\omega,a)\sqrt{\frac{a}{b}}}\right| \tag{2-40}$$

$$\beta(\omega)=\frac{1}{b-a}\left|\phi(\omega,b)-\phi(\omega,a)\right| \tag{2-41}$$

Hence, the transfer function of the cable PEA system at position *r* is given by:

$$G(\omega,r)=\frac{P(\omega,r)}{P(\omega,a)}=e^{-[\alpha(\omega)+j\beta(w)](r-a)} \tag{2-42}$$

The above transfer function can be used in the frequency domain to compensate the attenuation and dispersion factors during the acoustic wave propagation at different positions, and the actual acoustic pressure profile across the insulation can be obtained by applying the inverse Fourier transform [78] [80].

2.4 Summary

The theoretical background of charge generation and transport in insulating polymers has been reviewed to provide a basis of space charge modelling for the present research. The space charge detection technique adopted in this study, the PEA method, has also been illustrated, which will be applied to measure the space charge distribution in both flat and cylindrical geometry polymeric insulation samples.

Chapter 3 Electric field calculation in HVDC cable insulation

The electric field distribution in HVDC cable system does not follow the same rules as for AC stress, and till now the field estimation in HVDC extruded cable is still very challenging for cable design. Several calculations of the electric field distribution within the HVDC extruded cable insulation have been published, and such approaches are serving as an importance reference for HVDC cable design [81] [82]. However, the limitations of such models have been recognized as the results are generally different from the experimental observations [56]. In this chapter, first, the differences in the electric field distribution between AC and DC cables will be discussed. Both the traditional conductivity model and the bipolar charge transport model are introduced and employed to simulate the space charge and field distribution in a medium voltage size polymeric insulation cable. Comparisons are made between the two models based on the experimental data and simulation results. The transient field distribution in DC cable under the polarity reversal is investigated.

3.1 Differences in electric field distribution between AC and DC cables

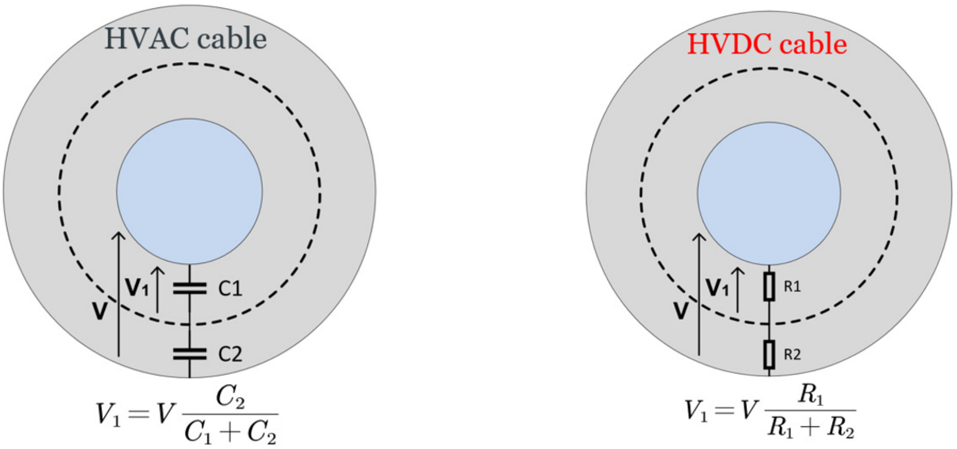

$$V_1 = V\frac{C_2}{C_1+C_2}$$

$$V_1 = V\frac{R_1}{R_1+R_2}$$

(a) (b)

Figure 3-1. Schematic representation of the electric potential at any point in cables: (a) in AC cables; (b) in DC cables.

As shown in Figure 3-1a, in AC cables, the electric potential along the radius of the insulation is controlled by capacitance. Therefore, the electric field E_{AC} depends on the permittivity ε of the dielectric, which changes little within the working range of temperature and field [83]. On the contrary, the electric potential at any point in DC cables is determined by the resistance, and the electric field E_{DC} becomes conductivity σ dependent, which in turn depends on the temperature and E_{DC}.

By assuming the permittivity of the insulation is constant with temperature, the electric field E_{AC} at any radius in AC cables can be drawn easily, as presented in following,

$$E_{AC}(r) = \frac{U_0}{r\ln(r_o/r_i)} \tag{3-1}$$

where U_0 is the applied voltage on the dielectric (in AC regime, it is the phase-to-ground voltage); r is the position along the radius; r_i and r_o is the inner and outer radius of the cable insulation respectively. A typical electric field distribution within the insulation of a HVAC cable is shown in Figure 3-2, and it is called a capacitive field distribution [5]. It can be observed that the maximum field strength E_{MAX} in a HVAC cable always occurs at the conductor/insulation interface, while the minimum field strength E_{MIN} always occurs at the insulation/metallic screen interface.

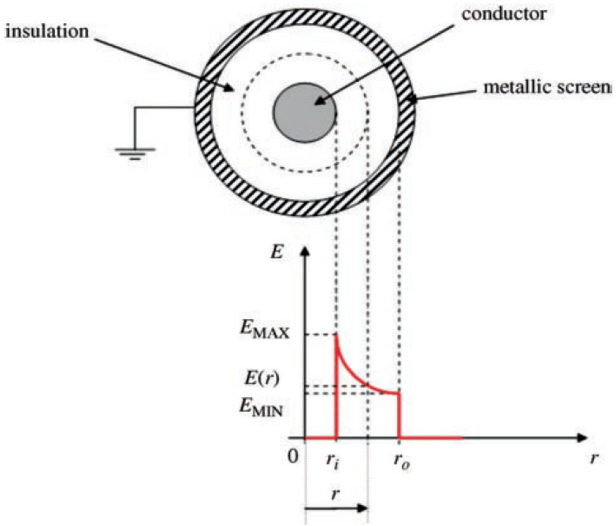

Figure 3-2. Electric field distribution in a HVAC cable insulation (capacitive field distribution) [5].

Following Maxwell's equation, the steady state electric field in DC cables is given as following [75]:

$$E_{DC}(r) = E_0\frac{r_0\sigma_0}{r\sigma(r)} \tag{3-2}$$

where E_0 and σ_0 are the electric field and conductivity at the reference position r_0, $\sigma(r)$ is the conductivity along the cable radius. Figure 3-3 presents the electric field distribution in a HVDC cable under different load conditions, and such temperature-dependent electric field is called a resistive field distribution [13]. When the DC field is first applied, the electric field is a quasi-capacitive field distribution. Due to the joule heating from the conductor, a temperature gradient would be formed across the insulation thickness, and the inner part near the conductor withstands the highest temperature. In this situation, the conductivity of the inner insulation increases significantly; therefore, the electric field near the conductor decreases considerably, but increases in the outer area. Generally, when the cable is fully loaded, the electric field can be reversed so that the highest stress transfers from the inner to the outer insulation. The field inversion limits the temperature rating of HVDC cables [84], and therefore, it is very important to calculate the electric field distribution at different operational stages, due to the high dependence between conductivity and temperature.

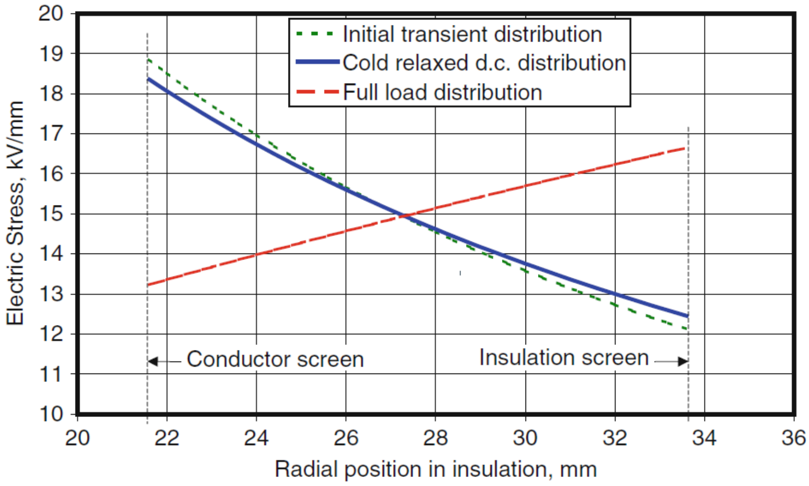

Figure 3-3. Electric field distribution in a HVDC cable under different load conditions (resistive field distribution) [13].

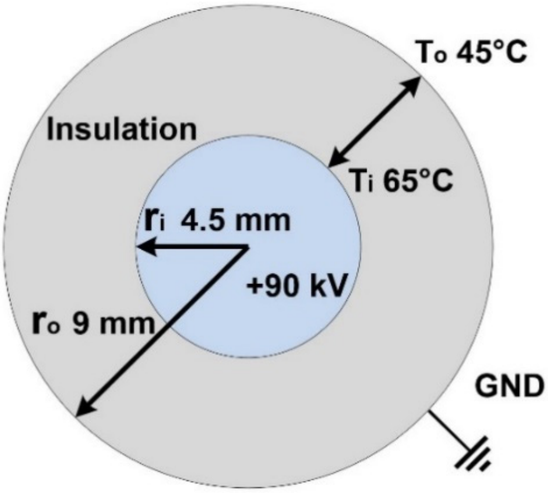

Figure 3-4. Schematic representation of the medium-voltage XLPE cable sample.

Anticipating DC field distribution in polymeric insulation is more challenging when considering space charge phenomena. In AC situation, the flow of charges inverts its direction too fast to allow space charge accumulating inside the dielectrics, namely, the space charge field can be neglected in AC cables. However, in DC cables, the space charge can build up in the bulk of insulation under various temperature and field, and the presence of space charge can lead to the local field enhancement, which may accelerate material ageing or cause electrical failures.

Over the two decades, the understanding and measurement of space charge has become the focus of the development of HVDC extruded cable technology. In order to study the space charge behaviour in the HVDC extruded cables in the presence of temperature gradient, measurements have been taken on a medium-voltage size XLPE cable by Fabiani et al. by means of the PEA detection method [75]. The inner radius (r_i) of the degassed XLPE cable insulation is 4.5 mm, and the outer radius (r_o) is 9 mm, providing an insulation thickness of 4.5 mm, as shown in Figure 3-4. A positive voltage of 90 kV was applied at the inner electrode, so the average electric field was about 20 kV/mm. A steady temperature gradient was applied across the insulation. The inner temperature was set to be 65°C and the outer temperature was 45°C. The experimental results showed the temperature gradient could enhance the charge accumulation greatly, and further distort the electric field in cable insulation, as shown in Figures 3-5 and 3-6 [74].

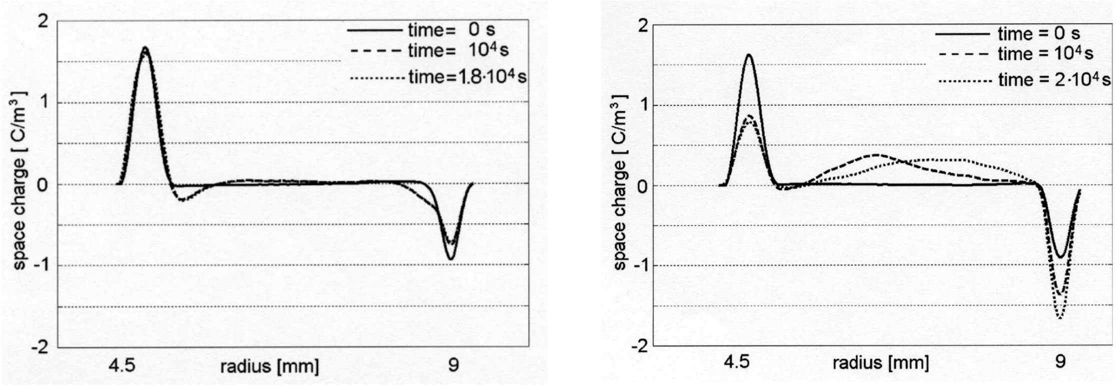

(a) (b)

Figure 3-5. Space charge profiles of XLPE MV-size cables with an average field of 20 kV/mm. (a) no temperature gradient. (b) with a temperature gradient of 20°C (65-45°C) [74].

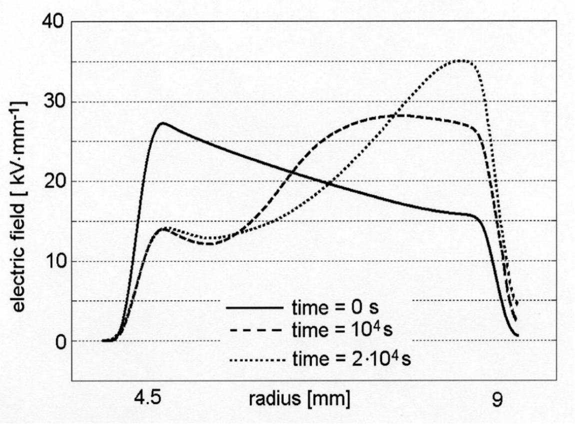

Figure 3-6. Electric field distribution across the insulation under a steady temperature gradient (65-45°C) in a MV size XLPE cable [74].

Numerical modelling of space charge and field distribution can assist to comprehend and predict material performance. In this chapter, two field estimation methods are introduced to calculate the electric field and space charge distribution in this medium voltage XLPE cable. All the electrical and thermal conditions were set to be same as the experimental measurements, so the results of both models can be compared with the experimental observations.

3.2 Conductivity model

It has been revealed that the volume conductivity of the cable insulation depends on both temperature and field, and thus the conductivity model was developed to anticipate the field distribution in loaded DC cable systems. This kind of methods is serving as an important reference for DC cable design, and actually started with the work of McAllister et al. in 1994. [82] [85] [86] [87]. Such macroscopic approaches consider the charge accumulation within the insulation resulting from conductivity gradient, and they can simulate either a positive or a negative charge accumulation inside the bulk. In their work, charge accumulation is considered to be the consequence of a non-uniform electrical conductivity, and the effects of temperature and field on conductivity are considered.

3.2.1 Model descriptions

Generally, this kind of model considers the cable insulation as a weakly conductive continuum in which a conductivity gradient is induced by the non-uniform electric field and the temperature gradient across the insulation. Due to the local non-homogeneity of the material, the current density at any point along the radius is not uniform, thereby forming space charge. Based on the current continuity equation, in a dielectric sample where a DC current of density j is flowing, a space charge density ρ can be acquired when a divergence takes place between the incoming and outgoing charge flow:

$$\nabla \cdot \vec{j} = -\frac{\partial \rho}{\partial t} \tag{3-3}$$

where j is the current density, ρ is the space charge density and t is the time. According to Gauss' Law and Ohm's Law,

$$\rho = \nabla \cdot \left(\varepsilon_0 \varepsilon_r \vec{E}\right) \tag{3-4}$$

$$\vec{j} = \sigma \vec{E} \tag{3-5}$$

By combining these three equations, the space charge density can be described in the dielectric material as:

$$\rho = -\frac{\varepsilon_0 \varepsilon_r}{\sigma} \frac{\partial \rho}{\partial t} + \vec{j} \cdot \nabla\left(\frac{\varepsilon_0 \varepsilon_r}{\sigma}\right) \tag{3-6}$$

Space charge ρ accumulates if the ratio between relative permittivity ε_r and conductivity σ were not uniform across the insulation, in the case of $j \neq 0$. The permittivity can be considered as a constant within the range of temperatures and DC fields, but the conductivity has to be considered as a function of both temperature and field [83]. An expression of the conductivity with Arrhenius' Law has been widely used to describe the conductivity of the extruded cable insulation [88],

$$\sigma(E,T) = A_c \exp\left(\frac{E_a}{k_B T}\right) \frac{\sinh(B_c|E|)}{|E|} \tag{3-7}$$

where E_a is the thermal activation energy; k_B is the Boltzmann's constant; constants A_c and B_c are determined by the characteristics of the insulation material. The parameters in the above equation can be obtained by fitting the conductivity function with the experimental results of conduction current measurements on the planar samples of the material under a range of temperatures and fields. In this model, a time-varying conductivity gradient could be formed across the DC insulation due to the presence of temperature gradient and non-uniform electric field, driving the charge dynamics, and the electric field and space charge distribution can be calculated straightforward. The simulation flow chart is shown in Figure 3-7.

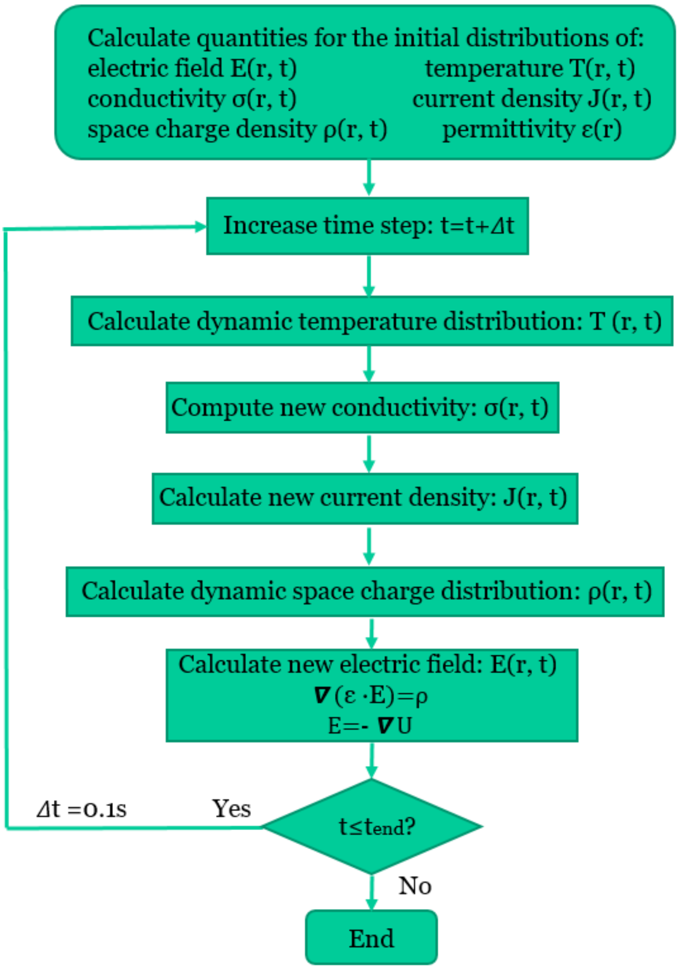

Figure 3-7. The simulation flow chart of the conductivity gradient model.

With the assumptions of the radial space charge distribution within the cable insulation is the same along the whole cable, independently on the axial and the angular position, the conductivity gradient model is resolved in 1-dimension, function of radius. The finite element method (FEM) software, COMSOL, has been used to build this 1-D time-dependent model in the cylindrical coordinate. Two different modules, Heat transfer (ht) and electric current (ec) have been coupled and utilized. The medium-voltage size XLPE cable insulation, which is presented in Figure 3-4, is equally divided into 200 partitions, and the specific quantities are assumed to be constant within each partition and within a time interval *Δt*.

3.2.2 Simulation results

A steady temperature gradient that derived from the thermal Ohm' Law has been applied across the insulation, where the inner temperature $T(r_i)$ is set to be 65℃ and the outer temperature $T(r_o)$ is 45℃.

$$T(r) = T(r_o) + \frac{\ln\left(\frac{r_o}{r}\right)\left(T(r_i) - T(r_o)\right)}{\ln\left(\frac{r_o}{r_i}\right)} \tag{3-8}$$

Table 3-1. Parameters used for the conductivity model [74].

Parameter	Value	Unit
A_c	$1*10^{14}$	Am^{-2}
B_c	$2*10^{-7}$	$V^{-1}m$
E_a	1.48	eV

The parameters used in the conductivity model are shown in Table 3-1, and they were obtained from fitting the conductivity function with the conduction current measurements on the thermally pre-treated XLPE specimens [74]. However, it should be noted that the adopted activation energy is fairly high in comparison with the values usually found in the literature for XLPE [88]. Although it has been claimed that the adopted activation energy does not characterize the XLPE insulation alone, it also includes the effect that the semi-conductive electrodes have on the conduction in the XLPE. In literature [89], it has been reported that the semicon layer can enhance the charge injection and further affect the charge behaviour in XLPE. However, there is still lack of evidence to directly illustrate how the semicon layer affects the conduction mechanism in polymeric insulation. The parameters are only considered from fitting the semi-empirical equation by conduction current measurements, and their physical justifications are still need to be further investigated.

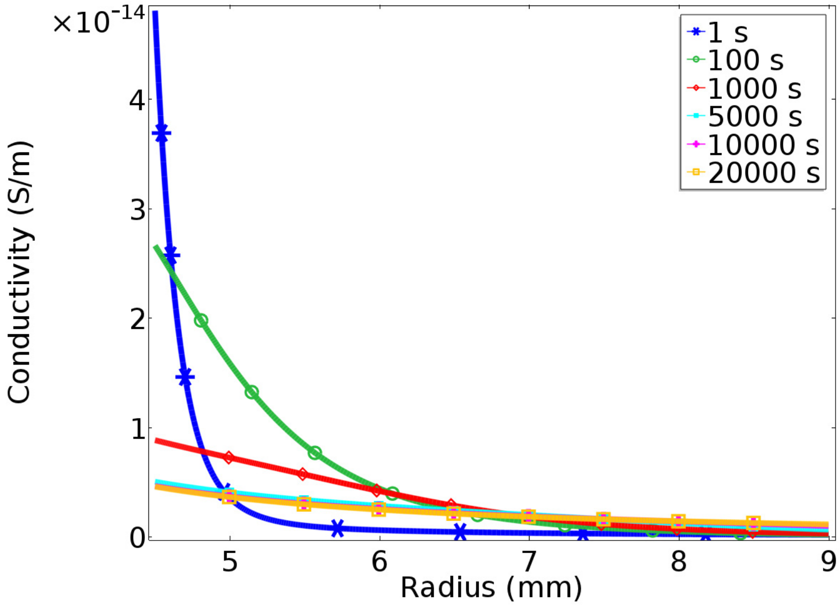

Figure 3-8. The conductivity gradient across the cable insulation in the presence of temperature gradient.

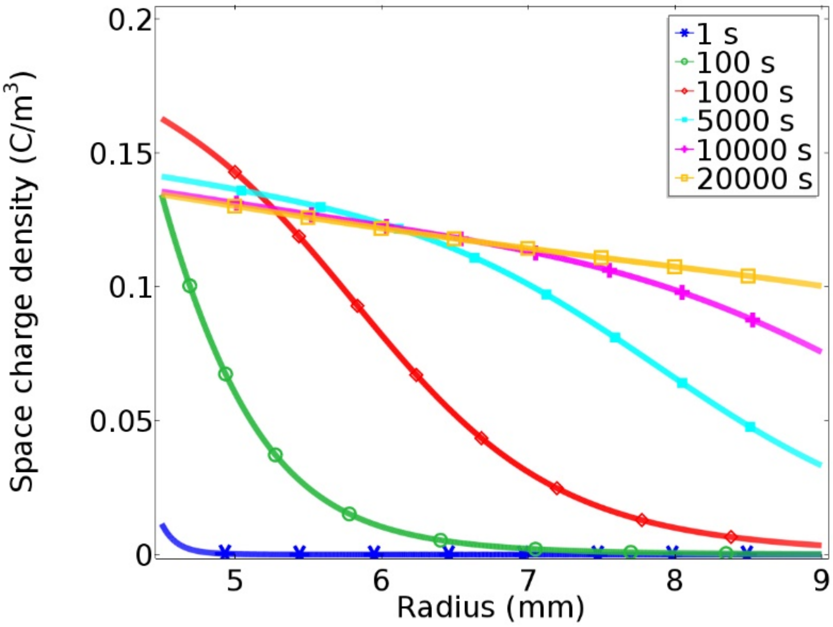

Figure 3-9. The space charge distribution in the MV size cable calculated by the conductivity model.

The conductivity gradient across the cable insulation is shown in Figure 3-8. Due to the temperature gradient and the divergent field over the insulation thickness at the start, the conductivity at the inner part is considerably high, but it is low at the outer insulation. The conductivity gradient decreases with time gradually, and then maintains at a relatively gentle slope, as the field distribution changes with time. Figure 3-9 presents the space charge distribution evolving with time in the extruded cable sample calculated by the conductivity model. It can be observed that only one-polarity (positive) charges accumulated inside the insulation bulk, and the sign is the same as the voltage applied at the inner electrode. At the beginning, very limited charges can be observed at the outer electrode, conversely, much more charges are accumulated at the inner insulation. The accumulation of charge is believed to generate from the non-uniform current density along the radius. Due to the presence of the temperature gradient and the divergent field, an extremely large conductivity gradient is formed across the insulation, therefore charges accumulate very quickly at this stage, especially at the inner part of insulation. As the steady field distribution is resistive under DC stress, the outer part will withstand higher electric stress due to a lower conductivity, and the such resistive field distribution can reduce the conductivity gradient and slow the charge accumulation. Until t=20000 s, the average of the space charge density in the insulation bulk is about 0.12 C/m^3.

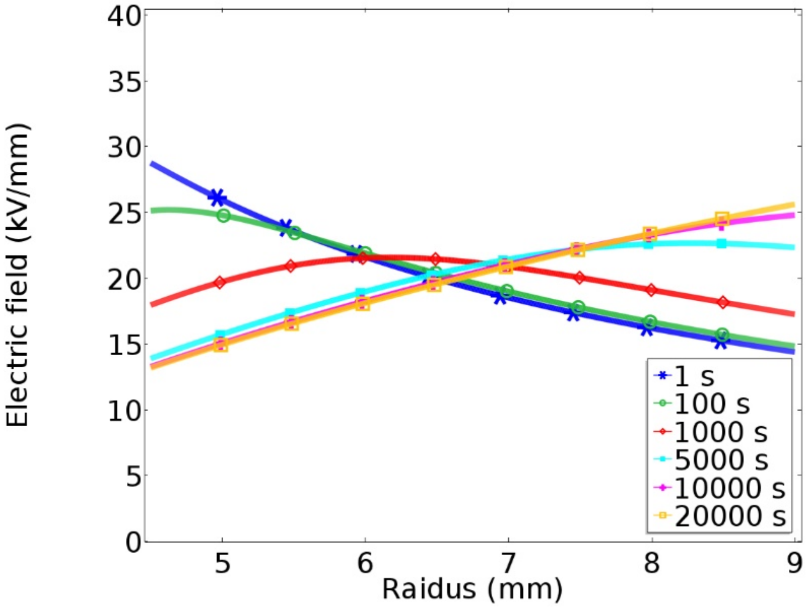

Figure 3-10. Electric field distribution in the cable insulation calculated by the conductivity model.

The calculated electric field distribution is shown in Figure 3-10. When the DC field is first applied, the electric field distribution is quasi-capacitive, which is mainly dependent on the permittivity of insulation, and the insulation close to the conductor withstands the highest electric stress. Because of the presence of a steady temperature gradient (65-45°C), the conductivity at the inner side is extremely large while that of the outer area is relatively small. Therefore, the electric field near the conductor will decrease considerably, but increase in the outer area. Under this 20°C temperature gradient, the field inversion phenomenon is predicted by this model so that the highest stress transfers from the inner to the outer insulation.

Although the simulation results from the conductivity model can describe the space charge and field distribution evolving with time in the cable insulation, there are still some differences when compared with the experimental results shown in Figures 3-5b and 3-6. The space charge distribution calculated by the conductivity model cannot be compared with the experimental data, as only one-polarity charge is simulated in the conductivity model. Meanwhile, the predicted electric field distribution near the outer screen at t=20000 s is about 25 kV/mm, which is fairly underestimated compared with the experimental data of 35 kV/mm. It must be emphasized that the space charge considered here is not dependent upon the operation of any space charge generation mechanism, in particular, the space charge distribution is calculated from the non-uniform current density resulting from the conductivity gradient across the insulation bulk. It is considered that the accumulated charges are contributed from all types of charge carriers, including holes, electron and ionic charges, as the parameter conductivity considers the overall contribution that each type of charge carriers has on the conduction process.

The conductivity model is widely used, as only a few macroscopic parameters (e.g. conductivity as a function of field and temperature) of the insulation material are required, making it applicable to many practical situations (such as different geometries and external conditions). Moreover, the calculation is relatively simple and timesaving. Therefore, this macroscopic model is widely implemented to predict the electric field distribution for HVDC cable design. However, the limitations of such models have been recognized as the simulation results are generally different from the experimental observations [56]. As described above, the conductivity gradient model considers the extruded insulation as a homogeneous material, and the calculated field and charge distributions are continuous and regular. Nevertheless, it is well established that the localized space charge accumulation can be formed in the HVDC extruded cable insulation, due to the complicated charge conduction mechanism such as charge trapping associated with the highly non-uniform microstructure of the extruded insulation [90] [58].

3.3 Bipolar charge transport model

An alternative to the macroscopic modelling is the bipolar charge transport theory, which was developed based on the approaches used in semiconductor physics, providing well descriptions of the charge generation and transport mechanisms. In the following section, the theory and the simulation results of the bipolar charge transport model will be presented.

3.3.1 Historical evolution of the bipolar charge transport theory

The bipolar charge transport theory was firstly proposed by Alison and Hill in 1994 for simulation of charge profiles in degassed XLPE insulation [91]. This primary model features the double injection of charge carriers along with the extraction at both electrodes without considering the existence of potential barriers. Moreover, charge carriers were assumed to transport with a constant mobility and the carriers could be trapped in deep trapping sites. Their simulated results supported the qualitative interpretation of space charge dynamics. However, the numerical results were not well matched with the experimental data due to the simple and limited descriptions on charge migration and trapping processes. In the same year, Fukuma et al. revised the bipolar charge transport model by introducing the Schottky injection mechanism at the interface of electrode/dielectrics. Furthermore, charge transport procedure was described by a hopping conduction mechanism which was dependent on the electric field and temperature. With these updates, the simulated results could fit the measured data from Li and Takada well [92]. In 1999, Kaneko et al. reported a similar revised model to simulate the formation of space charge packets in XLPE films under high electric field [93]. Bipolar charges were generated by a Schottky mechanism and transport followed a hopping mechanism. Charge recombination was taken into account and no deep trapping level was considered. Results were compared with the experiment data including space charge profiles and external current, nevertheless the fit was not totally satisfactory.

Table 3-2. Features of the principal bipolar charge transport model.

Reference	**Charge generation**	**Charge extraction**	**Charge transport**	**Charge trapping**	**Charge recombination**
Alison and Hill (1994)	Constant source at both electrodes	Non-blocking electrodes	Constant effective mobility	One deep trap level, no detrapping	For mobile and trapped charge carriers
Fukuma et al (1994)	Schottky injection at both electrodes	Extraction potential barriers	Hopping conduction between sites of the same energy.	One deep trap level, no detrapping	For mobile charge carriers
Kaneko et al (1999)	Schottky injection at both electrodes	Non-blocking electrodes	Hopping conduction between sites of the same energy.	No deep trapping	For mobile charge carriers
Le Roy et al (2004-2006)	Schottky injection at both electrodes	Non-blocking electrodes	Effective mobility / Hopping conduction;	Trapping on one deep trapping level with detrapping	For mobile and trapped charge carriers

Based on the previous work, Le Roy et al. gave a description of bipolar charge transport theory in low-density polyethylene (LDPE) in 2004 [94]. In their work, bipolar trapping, transport and recombination were taken into account, and the potential barrier for charge extraction was removed, as no evidence of hetero charge accumulation is found based on the experimental observations in LDPE [95]. In 2006, they further improved the bipolar transport model by considering the detrapping process [57]. Two kinds of traps in polyethylene were considered in their approach: the conduction sites for hopping mechanism and the deep trapping sites. The model parameters have been adjusted by fitting the experimental data from space charge measurements and conduction current measurements. A good agreement has been achieved between the experiment and simulation, and a correlation between the measured electroluminescence and recombination rate has been proposed [96]. The features of the above charge transport models are concluded in Table 3-2.

The above models can present reasonable charge dynamics within the dielectrics and they have been further improved by many other researchers around the world, in order to predict the space charge distribution and understand the space charge processes within the insulation bulk under different voltage levels [97] [98] [99]. Generally, such models consider the charge generation arising from injection at the electrodes, the charge transport processes are described by taking into account trapping, detrapping and recombination. Their solution is always one dimensional, function of the thickness of plane sample, and time dependent. However, only few attempts have been made to develop the bipolar charge transport model in cable geometry [100]. Additionally, the temperature gradient across the insulation also needs to be taken into account, because temperature could have a huge impact on the space charge behaviour. In 2016, Le Roy et al proposed a modified bipolar charge transport model within a cylindrical configuration, and the radial temperature distribution was taken into account [100]. Nevertheless, the source of charges is the electronic injection defined simply by a modified Schottky law at each electrode, which is considered to be unsatisfactory for describing the charge injection under low DC field accurately.

In this study, the bipolar charge transport model is modified for simulating space charge behaviour in a cable geometry. The temperature gradient across the insulation has been taken into account. Based on many experimental observations, a threshold electric field at which the charge injection takes place is introduced, in order to define the boundary condition more precisely.

3.3.2 Model descriptions

The bipolar charge transport theory starts from the injection of both positive and negative charge carriers at the interface of the insulation/electrodes when the applied electric field exceeds the threshold field. The injected electrons and holes migrate into the bulk of dielectrics towards the opposite electrodes under the influence of the electric field, forming the conduction current. Due to the localized energy states existing in the band-gap of the dielectrics, these “traps” may capture holes and electrons, forming trapped charge. Moreover, the trapped holes/electrons also have the possibility to escape from these "traps". In this model, deep trapping is taken into account through the existence of a single trapping level for each kind of carriers, and charge carriers have a given probability to escape from traps. When the charge carriers of opposite polarity encounter each other in the bulk or at the interface of electrode/dielectric, they recombine and give out energy normally in the form of light emission, i.e., electroluminescence, so the recombination of opposite polarity charges also needs to be considered. Therefore, four species are considered in the model, mobile electrons/holes, trapped electrons/holes, as shown in Figure 3-11 [62].

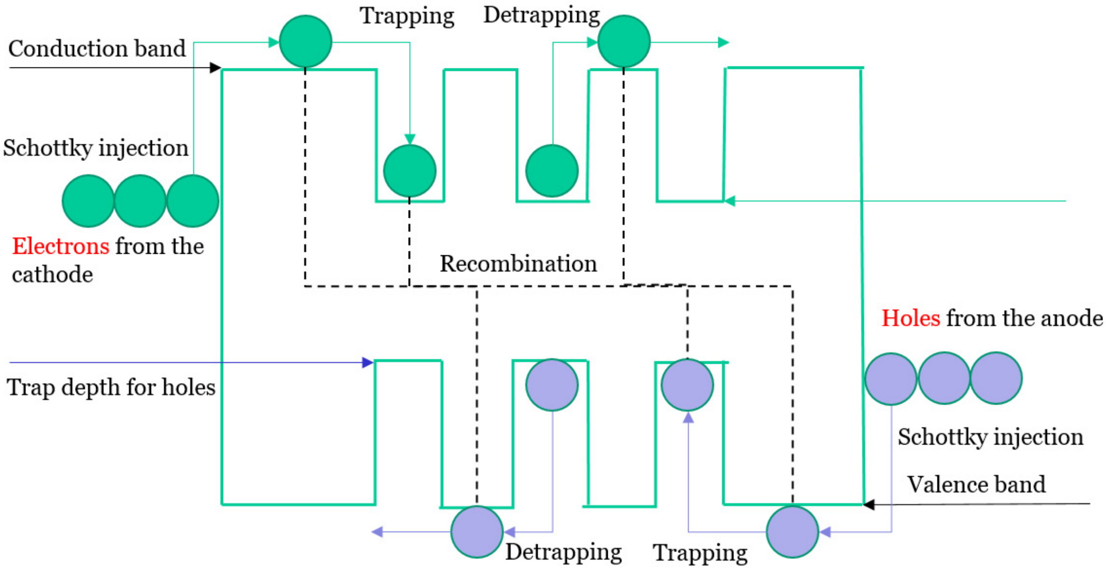

Figure 3-11. Schematic representation of the bipolar charge transport model [62].

In the bipolar charge transport model, three space and time dependent equations are presented to describe the charge behaviour in cylindrical geometry as following, neglecting diffusion,

$$\frac{\partial^2 V(r,t)}{\partial r^2} + \frac{1}{r}\frac{\partial V(r,t)}{\partial r} = -\frac{\rho(r,t)}{\varepsilon_0 \varepsilon_r} \tag{3-9}$$

$$\frac{\partial n_{a\mu,at}(r,t)}{\partial t} + \frac{1}{r}\frac{\partial (j_a \cdot r)}{\partial r} = s_{a\mu,at}(r,t) \tag{3-10}$$

$$j_a(r,t) = \mu_a(r,t) n_{a\mu}(r,t) E(r,t) \tag{3-11}$$

where *j* is the conduction current density; *n* is the charge density; *E* is the electric field; *ρ* is the net charge density; ε_0 is the vacuum permittivity, ε_r is the relative dielectric permittivity, which is considered as a constant (2.3 for polyethylene). Here *a* refers to the type of charge, and the subscript *μ* or *t* refers respectively to mobile or trapped charge. *s* are the source terms which encompass the changes in local density by the processes other than transport (trapping, detrapping and recombination). The expressions for source terms of each species are given by:

$$\begin{aligned}
s_{e\mu} &= \frac{\partial n_{e\mu}}{\partial t} = -S_1 n_{ht} n_{e\mu} - S_3 n_{h\mu} n_{e\mu} - B_e n_{e\mu}\left(1 - \frac{n_{et}}{n_{oet}}\right) + D_e n_{et} \\
s_{h\mu} &= \frac{\partial n_{h\mu}}{\partial t} = -S_2 n_{et} n_{h\mu} - S_3 n_{h\mu} n_{e\mu} - B_h n_{h\mu}\left(1 - \frac{n_{ht}}{n_{oht}}\right) + D_h n_{ht} \\
s_{et} &= \frac{\partial n_{et}}{\partial t} = -S_2 n_{h\mu} n_{et} - S_0 n_{ht} n_{et} + B_e n_{e\mu}\left(1 - \frac{n_{et}}{n_{oet}}\right) - D_e n_{et} \\
s_{ht} &= \frac{\partial n_{ht}}{\partial t} = -S_1 n_{ht} n_{e\mu} - S_0 n_{ht} n_{et} + B_h n_{h\mu}\left(1 - \frac{n_{ht}}{n_{oht}}\right) - D_h n_{ht}
\end{aligned} \tag{3-12}$$

where $s_{e\mu}$, $s_{h\mu}$, s_{et}, s_{ht} are the source terms for each species; S_0, S_1, S_2, S_3 are the recombination coefficients for different opposite species; B_e, B_h are the trapping coefficients for mobile electrons/holes; $n_{e\mu}$, n_{et}, $n_{h\mu}$, n_{ht} respectively indicate the densities of each species; n_{oet}, n_{oht} are the trap densities for electrons and holes. D_e, D_h are the detrapping coefficients for electrons and holes of the form [101]:

$$D_{e,h}(r,t) = v \cdot \exp\left(\frac{-e \cdot w_{tre,trh}}{k_B T(r)}\right) \tag{3-13}$$

where w_{tre} and w_{trh} are the potential barriers for charge carriers escaping from traps. The charge carrier recombination is accounted by considering different coefficients S_i for several electron-hole pairs. These coefficients are of the Langevin form [100], function of the carrier mobility, hence function of temperature, which can be written as follows:

$$\begin{aligned}
S_0 &= S_{et,ht}(r,t) = 0 \\
S_1 &= S_{e\mu,ht}(r,t) = \frac{\mu_e(r,t)}{\varepsilon_0 \varepsilon_r} \\
S_2 &= S_{et,h\mu}(r,t) = \frac{\mu_h(r,t)}{\varepsilon_0 \varepsilon_r} \\
S_3 &= S_{e\mu,h\mu}(r,t) = \frac{\mu_e(r,t) + \mu_h(r,t)}{\varepsilon_0 \varepsilon_r}
\end{aligned} \tag{3-14}$$

Conduction between shallow traps is described using a temperature-dependent hopping type mobility of the form, for each kind of charge carriers:

$$\mu_{e,h}(r,t) = \frac{2 d_a v}{E(r,t)} \exp\left(\frac{-e w_{\mu e,\mu h}}{k_B T(r)}\right) \sinh\left(\frac{e E(r,t) d_a}{2 k_B T(r)}\right) \tag{3-15}$$

where d_a is the the average distance between traps (in the order of nm) and the form of which has been described in literature [101]; e is the elementary charge; T is the temperature inside the dielectric, function of radius; k_B is the Boltzmann's constant; $w_{\mu e}$ and $w_{\mu h}$ are the hopping barrier heights for electrons and holes respectively. v is the attempt to escape frequency.

The Schottky injection of charge carriers takes place at the interface between the conductor and the insulator when the applied field is higher than the threshold field, which is of the form:

$$\begin{aligned} j_e(r_o,t) &= AT^2(r)\exp\left(\frac{-ew_{ei}}{k_B T(r)}\right)\exp\left(\frac{e}{k_B T(r)}\sqrt{\frac{eE(r,t)}{4\pi\varepsilon_0\varepsilon_r}}\right) \\ j_h(r_i,t) &= AT^2(r)\exp\left(\frac{-ew_{hi}}{k_B T(r)}\right)\exp\left(\frac{e}{k_B T(r)}\sqrt{\frac{eE(r,t)}{4\pi\varepsilon_0\varepsilon_r}}\right) \end{aligned} \tag{3-16}$$

where w_{ei} and w_{hi} are the injection barrier heights for electrons and holes respectively. The conventional boundary condition is only defined by the Schottky injection law at the electrodes, as shown in Figure 3-12a. From the previous work done by Liu et al, a value of threshold field of 10 kV/mm has been identified for charge injection in polyethylene [102]. Therefore, in this study, when the applied field exceeds the critical value (10 kV/mm), the boundary is defined by the Schottky injection law at both electrodes. However, there are still few space charges can be detected when the bulk is subjected to relatively low DC electric field. These charge carriers are suggested to be generated due to the Ohmic conduction at the interface between metal and dielectrics, and such contribution is considered as a linear field-dependent function [103], which is defined as a first order function that connects the zero point with the value of Schottky injection current density at the threshold to avoid discontinuity during the numerical modelling. In this model, the Schottky injection law dominates when the applied electric field exceeds the threshold, and the conduction of Ohmic type takes over under the low field, as shown in Figure 3-12b.

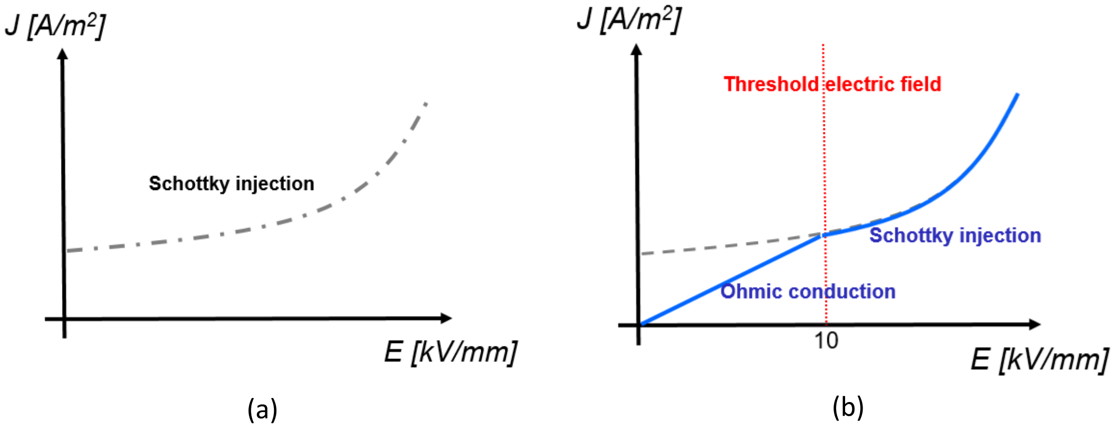

Figure 3-12. Schematic modified boundary condition as a function of electric field (not to scale): (a) conventional condition; (b) modified condition.

It should be noted that the extraction barriers of charge carriers are not considered, and the extraction fluxes for holes at the cathode and for electrons at the anode follow the transport equation. The simulation procedure is explained in the flow chart as shown in Figure 3-13, and N is the number of the time steps. The time step Δt in the computation must satisfy the Courant-Friedrich-Levy relation (CFL), involving that the charge displacement within Δt is less than the size Δr, as presented below:

$$\Delta t < \frac{\Delta r}{\mu E} \tag{3-17}$$

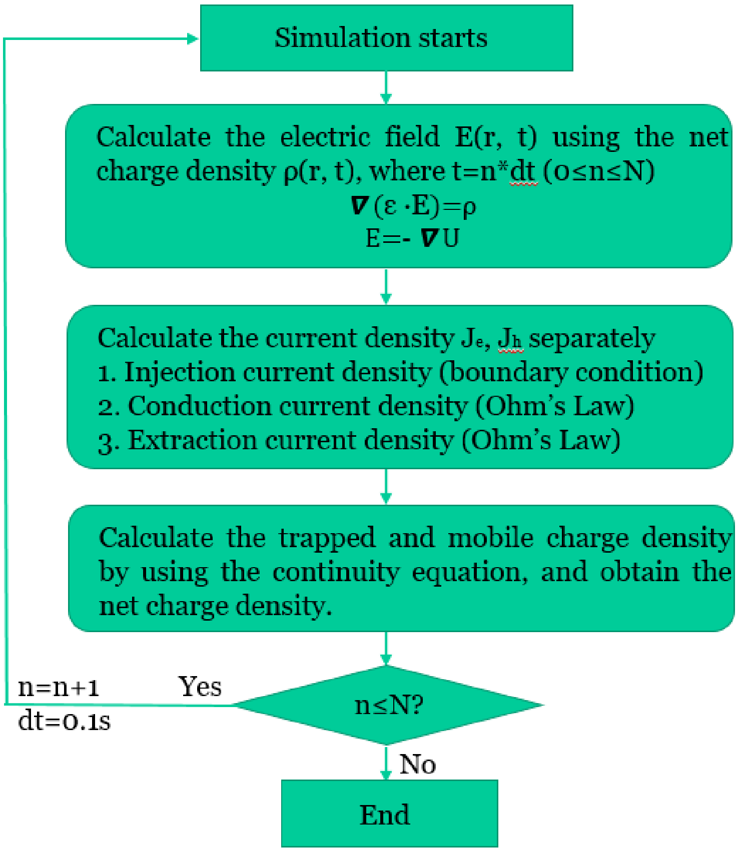

Figure 3-13. Flow chart of bipolar charge transport model.

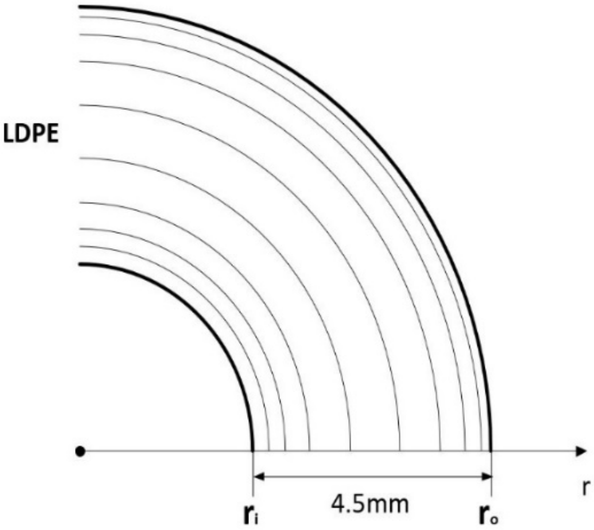

Figure 3-14. The schematic representation of the cable geometry and the one-dimensional grid used for the simulation.

It is assumed that the radial space charge distribution within the cable insulation is the same along the whole cable, independently on the axial and the angular position. Therefore, the bipolar charge transport model is resolved in 1-dimension, function of radius. The bipolar charge transport model can be implemented by using either MATLAB coding of partial differential equation (PDE) solvers, or by building model with COMSOL Multiphysics. The obtained simulation results from both methods are consistent, which has been proven by the author.

In this chapter, the simulation results of the bipolar charge transport model are obtained from COMSOL Multiphysics. The “Transport of Diluted Species (tds)”, the “Heat Transfer in Solids (ht)” and the “Electrostatics (es)” modules have been utilized to simulate the charge dynamics migrating in electric field. Figure 3-14 presents the schematic discretization grids used for the simulation. The thickness of the cable sample is divided into 200 divisions of different sizes of Δr. In order to optimize the simulation results, the Δr is set to be smaller close to the electrodes. The smallest cell Δr next to the electrodes is of the order of 0.5 µm, and the maximal is about 100 times as thick as the smallest one.

3.3.3 Simulation results

In this section, simulations have been performed on the same MV size cable with the same thermal and electrical conditions. The parameters used in the bipolar charge transport model are given in Table 3-3, and they are mostly the ones that have been optimized from measurements achieved on space charge for a plane parallel LDPE [57]. The injection barrier height at the interface of aluminum/polyethylene has been experimentally measured in literature [104], which is about 5 eV for electron injection. However, when applying the theoretical value in Schottky injection law, the simulated current density is much lower than the experimental observation, as the theoretical value does not consider the local conditions of the interface and it cannot be used in the simulation. The range of the injection barrier height has been concluded by other charge transport model in polyethylene-based material, which is from 1.1 to 1.3 eV [57] [101]. The lower the injection barrier height, the more mobile charge carriers can be injected. The hopping barrier heights are deduced from the space charge and conduction current measurements at different temperatures, and the simulated charge mobility is in the range of 10^{-13}-10^{-15} $m^2V^{-1}s^{-1}$. The detrapping barrier height refers to the depth of deep traps, and it can be estimated from the space charge decay results, which is always in the range of 0.9-1eV. The trapping coefficient affects the probability of mobile charges being trapped, and a larger trapping coefficient leads to a larger amount of trapped charges, which limits the charge movement in the insulation bulk in consequence. The recombination coefficients follow the Langevin form, function of charge mobility, and hence in the range of 10^{-2}-10^{-4} $m^3C^{-1}s^{-1}$.

It has been found that the recombination coefficients lay in this range have limited impacts on current density, so the charge density is weakly affected [57].

Table 3-3. Parameters used in the bipolar charge transport model [57].

Parameter		Value	Unit
Injection barrier height	w_{ei} for electrons w_{hi} for holes	1.27 1.20	eV eV
Trapping coefficient	B_e for electrons B_h for holes	0.05 0.05	s^{-1} s^{-1}
Hopping barrier height (for mobility)	$w_{\mu e}$ for electrons $w_{\mu h}$ for holes	0.71 0.65	eV eV
Detrapping barrier height	w_{tre} for electrons w_{trh} for holes	0.96 0.99	eV eV
Trap density	n_{oet} for electrons n_{oht} for holes	100 100	C/m^3 C/m^3

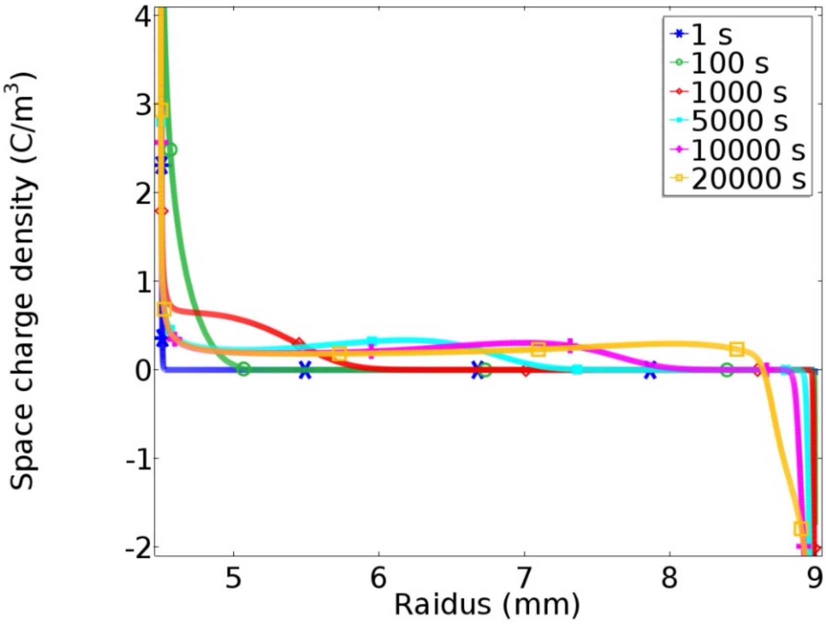

Figure 3-15. The calculated space charge distribution in MV size cable with a steady temperature gradient across the insulation.

When the DC voltage is applied, holes and electrons are injected from the anode and the cathode respectively, moving towards the opposite electrode under the influence of electric field, as shown in Figure 3-15. It is observed that the amount of holes penetrated into the volume increases with the time, but the electrons seem to remain in the vicinity of the cathode and the movement of them is not obvious as holes. Until t=20000 s, the bulk has been charged adequately with holes and electrons. The presence of extensive homo charges near the electrodes strongly decrease the electric field, especially at the anode, leading to an approximately non-injecting electrode shortly after the application of voltage, as presented in Figure 3-16.

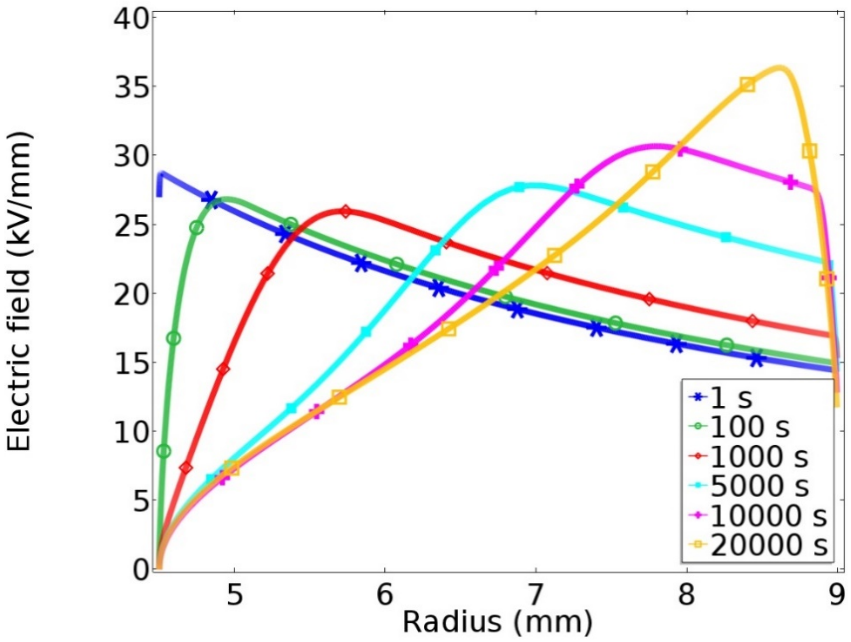

Figure 3-16. The electric field distribution within the insulation computed by the bipolar charge transport model.

The field variation within the insulation follows the movement of positive and negative charge carriers. With the increasing time, it can be observed that the maximal electric field location shifts from the anode to the cathode gradually. Namely the so-called stress inversion phenomenon, which has been widely reported in loaded HVDC cables, can be simulated by the bipolar charge transport model. At t=20000 s, the maximal electric field at the outer insulation has reached 36 kV/mm, which is very close to the experimental data. It can be argued that the simulation results from the bipolar charge transport model, such as the movement and distribution of charge carriers, are more comparable with the experimental observations shown in Figures 3-5b and 3-6.

3.4 Comparisons of the two models on simulating electric field in DC cable insulation

Both models are able to present appropriate features on charge behaviour and electric field distribution in a MV size DC cable insulation. The field inversion can be observed with both models under the steady temperature gradient. However, there are still some differences when compared with the experimental observations. First, the space charge distribution performed by the conductivity model is very different from the experimental results shown in Figure 3-5b, as only one-polarity charge is considered. Meanwhile, the final electric field distribution predicted by the macroscopic model at the outer side is 25 kV/mm, which is fairly underestimated compared with experiment data. In contrast, both the charge movement and field variation simulated by the bipolar charge transport model are very consistent with the experimental observations.

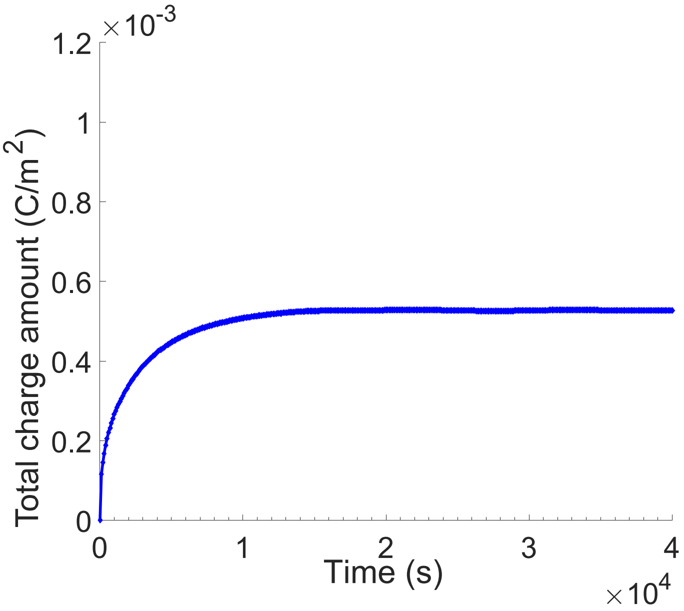

Figure 3-17. The total charge amount calculated by the macroscopic model.

Figure 3-17 shows the total charge amount evolving with time calculated by the conductivity model. The amount of charges increased dramatically in the first 10000 s and then maintained at 5.2×10^{-4} C/m^2 for the rest of time. The formation of the accumulated charges in the conductivity model is considered to be originated from the inhomogeneity of the conductivity across the insulation. At the initial stage, when the conductivity gradient along the radius of the insulation is steep, due to the presence of temperature gradient and the divergent field, charges would accumulate quickly. Then the variation of electric field would decrease the conductivity gradient and counterbalance the dissimilarity of the current density along the insulation. It has to be announced that the accumulated charges may be contributed from all types of charge carriers, including holes, electron and ions, as the parameter conductivity considers the overall contribution that each type of charge carriers has towards the conduction process. However, each kind of charge carriers behaves differently on the conduction process. The mobility, the possibility of being trapped and de-trapped and even recombination could be different from others, therefore, it might be not appropriate to consider the overall contribution of them. Besides, no information is provided about charge injection at the interface, but the charge accumulation at the interface affects the electric field distribution greatly. Additionally, the equivalent insulation is considered to have a conductivity function of which the parameters do not depend on the position. However, on the one hand, the conductivity at the interface of the electrode/insulation may differ from the one inside the bulk, due to the surface effect [105]. On the other hand, the impurity concentration could be non-uniform along the insulation thickness, which also contributes to the inhomogeneity of dielectric properties.

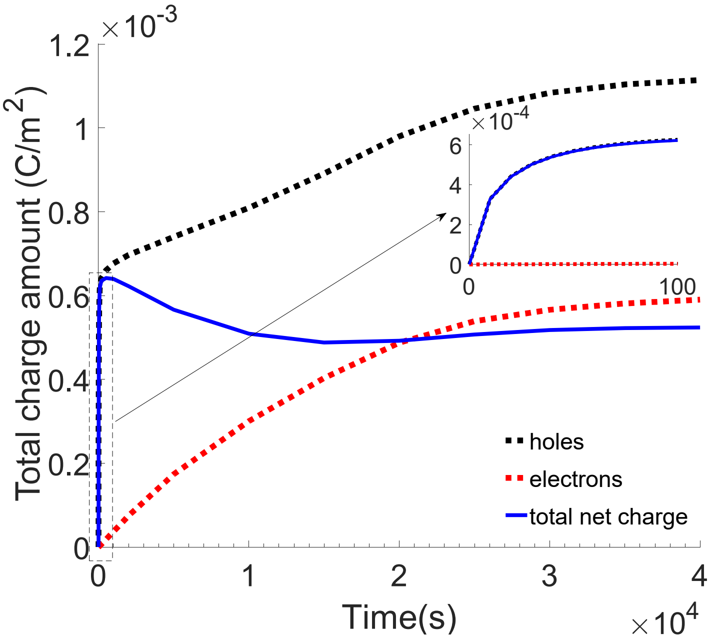

Figure 3-18. The charge amount for holes and electrons simulated by the bipolar charge transport model.

The total charge amount of holes and electrons (including trapped and mobile) inside the bulk computed by the bipolar charge transport model are shown in Figure 3-18. Shortly after the application of DC voltage, much more holes are injected from the anode compared with electrons, and this large amount of positive charges strongly decreases the field strength at the anode, which suppresses the injection of holes. This is a consequence of a higher temperature at the inner side and a lower Schottky injection barrier for holes. Therefore, the total net charge amount inside the bulk increases very rapidly in the first 100s. Due to the injection of electrons and the interaction between holes and electrons, the total net charge amount decreased and maintained at about 5.1×10^{-4} C/m^2 since 15000s, which is approximate with the total charge amount calculated by the conductivity model at the stationary state. It can be argued that the charges accumulate at the disuniformities of conductivity may be as the overall contribution of each kinds of charge carriers. Note that the bipolar charge transport model does not consider the ionization process, in spite of this, both the charge movement and the field variation seem to be more consistent when compared with the experimental data, as it gives very well descriptions on charge injection from the electrodes and charge transportation mechanisms inside the bulk. However, it is more complex when using the model in practical situations, as many parameters need to be taken into account carefully. The parameters related to charge generation and transportation mechanisms cannot be obtained with a straightforward way by independent experiments. Currently, the parameters used in the simulation is still based on the LDPE, and they need to be further optimized for a XLPE material. Moreover, the treatment of physical processes like ionization and hetero-charge build-up is not considered, which also limits its performance. The differences between the two models on simulating charge and field distribution in HVDC cable are summarized in Table 3-4.

Table 3-4. Comparison between the conductivity model and the bipolar charge transport model.

	Conductivity gradient model	Bipolar charge transport model
Features	• Fewer parameters • Simple and practical • Maybe accountable for ionic charge carriers	• More accurate and reliable • Well descriptions on charge generation and transport processes
Challenges	• Only one-polarity charge is simulated • The parameters of the conductivity function are independent of the position • No descriptions on charge injection at the boundary	• The parameters cannot be obtained straightforward, and the parameters still need to be further optimized for a XLPE material. • Ionic charge behaviour is not considered yet.

3.5 Space charge behaviour and transient field distribution in polymeric cable under voltage polarity reversal

The operation stages of the HVDC cable system has been described in detail in literature [85], including raising up the voltage, switching off the voltage and the voltage polarity reversal. It is known that high electric stress may occur at the conductor immediately after reversing the polarity of the applied voltage. Especially in the case of a loaded cable, the temperature gradient across the cable insulation promotes the space charge accumulation, which may result in unacceptable stress on the dielectric when the polarity of the applied voltage reverses. This problem has been limiting the application of extruded HVDC cables to VSC technology only, which allows to reverse the power flow direction by reversing the current flow, without permitting any voltage reversal. Indeed, polarity reversal withstand is extremely important for the resistance of the insulation to DC breakdown, as it has been shown that the breakdown resistance is reduced by approximately 10% on polarity reversal [3]. A great research effort has been made to solve this problem. Consequently, new XLPE-based compounds are being developed and the industrially produced extruded HVDC cables are able to withstand the voltage polarity reversal [54].

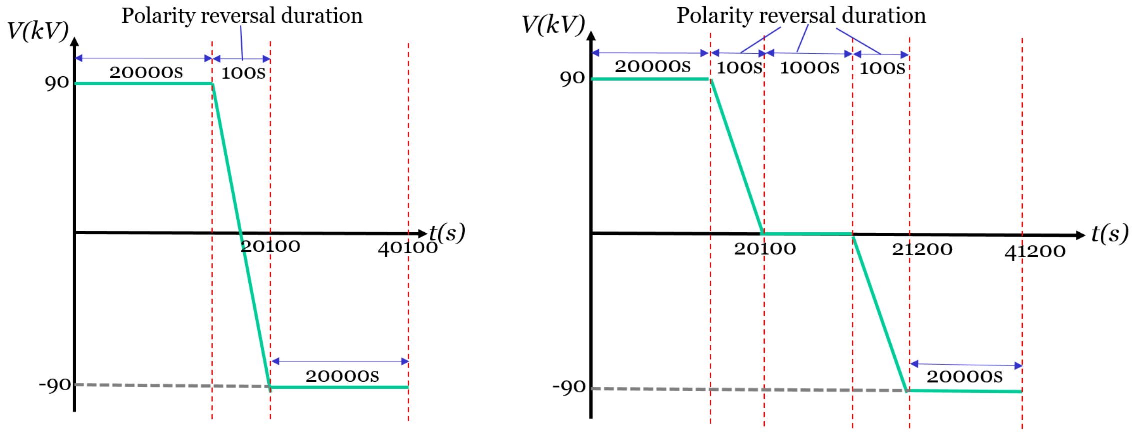

(a)

(b)

Figure 3-19. The schematic representation of applied polarity reversal voltage waveforms (not to scale): (a) a fast polarity reversal without earthing; (b) a slow polarity reversal with earthing [5].

In order to study the space charge behaviour and its effect on the transient field distribution under polarity reversal, the bipolar charge transport model is employed to simulate the space charge dynamics in polymeric cable insulation subjected to the two different types of voltage waveform, as presented in Figure 3-19. In the fast type of polarity reversal, as shown in Figure 3-19a, a positive voltage of 90 kV is applied at the conductor for 20000 s, then voltage is ramped linearly down to a negative voltage of -90 kV within 100 s and maintained at the same level for 20000 s. In the case of a slow polarity reversal, the polarity reversal is achieved by ramping down the voltage to zero which lasts 100 s, thereafter the cable conductor is left grounded for a period of 1000 s, then the voltage is ramped up to the opposite polarity in 100 s and then maintained for 20000 s, as shown in Figure 3-19b. Simulation is performed in the same MV size polymeric cable in the presence of a same temperature gradient (65-45°C), and the parameters used for the bipolar charge transport model are from Table 3-3, in order to investigate the space charge and field distribution in the insulation bulk after being subjected to the reversed voltage.

Since the anode and the cathode are reversed when the polarity of the applied voltage reverses, the direction of electric field need to be considered, and the electric field is set to be positive when the field direction is outward radial. Following the modified boundary condition setting at each electrode, which has been described in Section 3.3.2, the injection and extraction of holes at both interfaces are presented in Figure 3-20, and the electrons will be injected and extracted in a similar way. After the application of a positive DC voltage at the conductor, the holes will be injected following the Schottky injection law from the conductor and be extracted following the transport equation at the outer sheath. The field strength at the conductor is reduced due to the accumulated homo charges, and the linear conduction equation takes over under the low DC field. When the field direction is reversed, the outer sheath becomes the anode from which the holes will be injected, and the holes will be extracted at the conductor under the negative field.

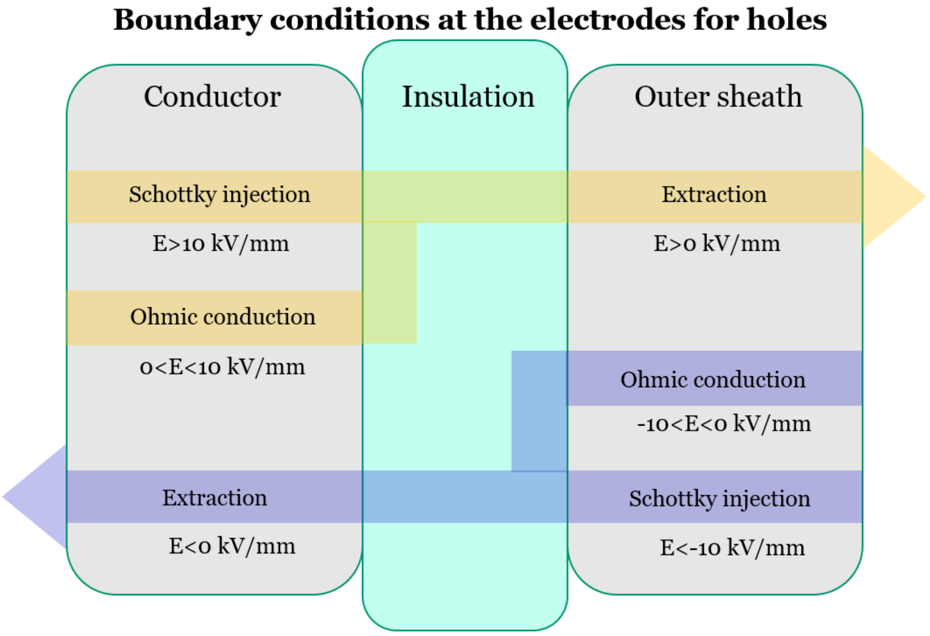

Figure 3-20. The boundary conditions for holes' injection and extraction at each interface.

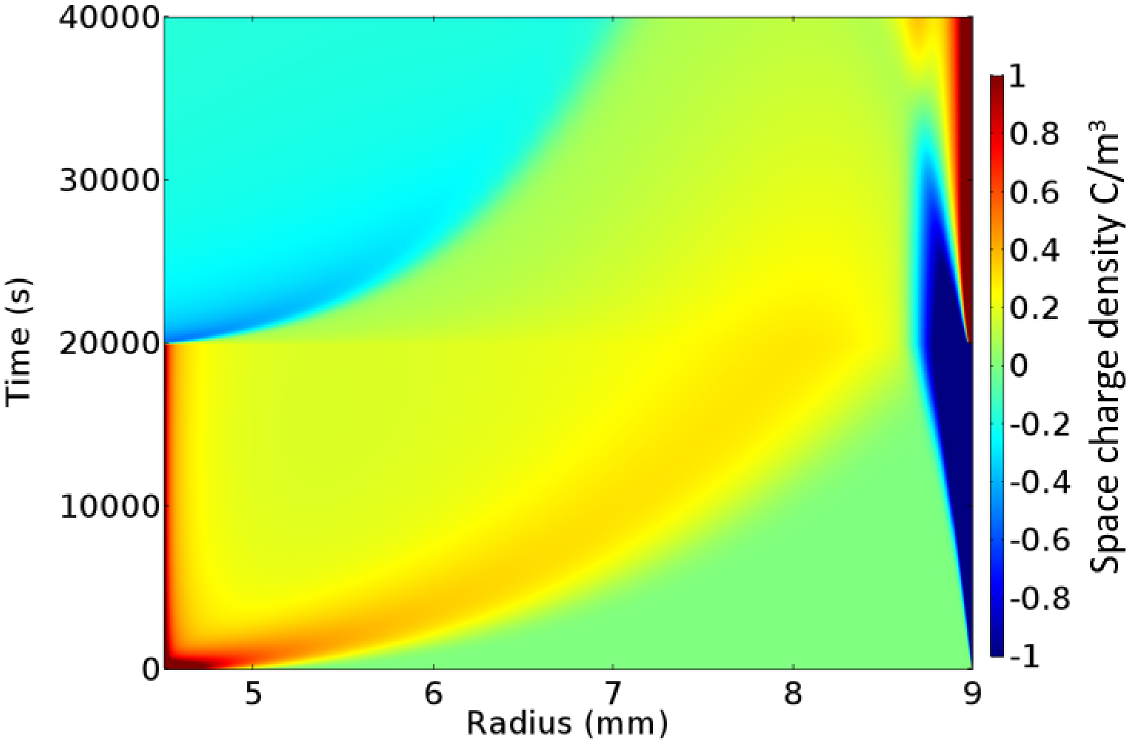

Figure 3-21. Space charge distribution along the insulation radius evolving with time under the fast voltage polarity reversal.

The simulation result of space charge profiles in the case of a fast polarity reversal is presented in Figure 3-21. The charge distribution in the first 20000 s is the same with the results given in section 3.3.3, and it should be noted that the axis of the space charge density has been truncated for observing the space charge distribution more clearly. Considerable positive charge carriers are injected and they penetrate much deeper than the electrons due to the higher mobility and the lower injection barrier height. After the polarity reversal, the electrons are injected from the inner electrode, and they migrate gradually into the bulk due to the higher temperature at the inner part. In contrast, the holes injected from the outer sheath seem to remain in the vicinity of the outer electrode, owing to lower mobility related to lower temperature, and they offset the accumulated electrons near the outer sheath gradually.

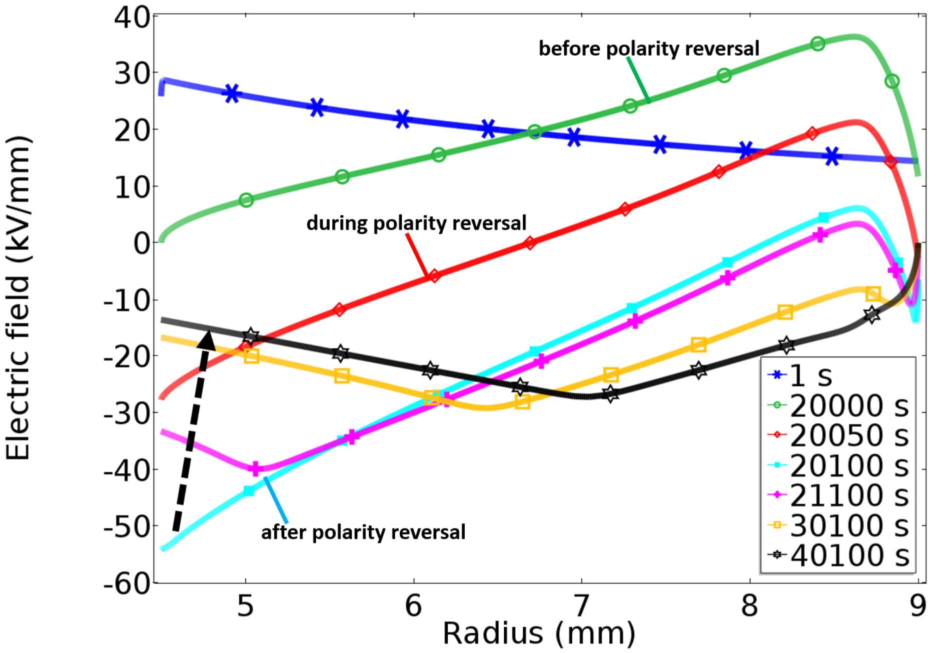

Figure 3-22. The calculated electric field distribution in polymeric cable insulation subjected to a fast voltage polarity reversal.

The corresponding electric field distribution within the insulation bulk is given in Figure 3-22. In the first 20000 s, the maximum field strength transfers from the inner to the outer part. Immediately after the polarity reversal, by superimposing the local field generated from the space charge accumulation, the electric field strength at the conductor reaches about -55 kV/mm. This is because the formation of considerable homo charges near the anode becomes hetero charges when the voltage polarity is reversed, which enhance the field strength greatly. Even if the overstress is not as high as to exceed the breakdown strength of the insulation, it can however accelerate the degradation reactions by the electrostatic energy associated with the accumulated charge and cause the formation of weak points in the insulation material, triggering ageing processes [4]. It has been confirmed by experimental data that the polarity reversal causes a reduction in the life of the insulation material [43]. The electrons are injected from the conductor under the reversed voltage, and the accumulated positive charges near the inner electrode are gradually extracted, leading to a reduced field strength at the conductor at last.

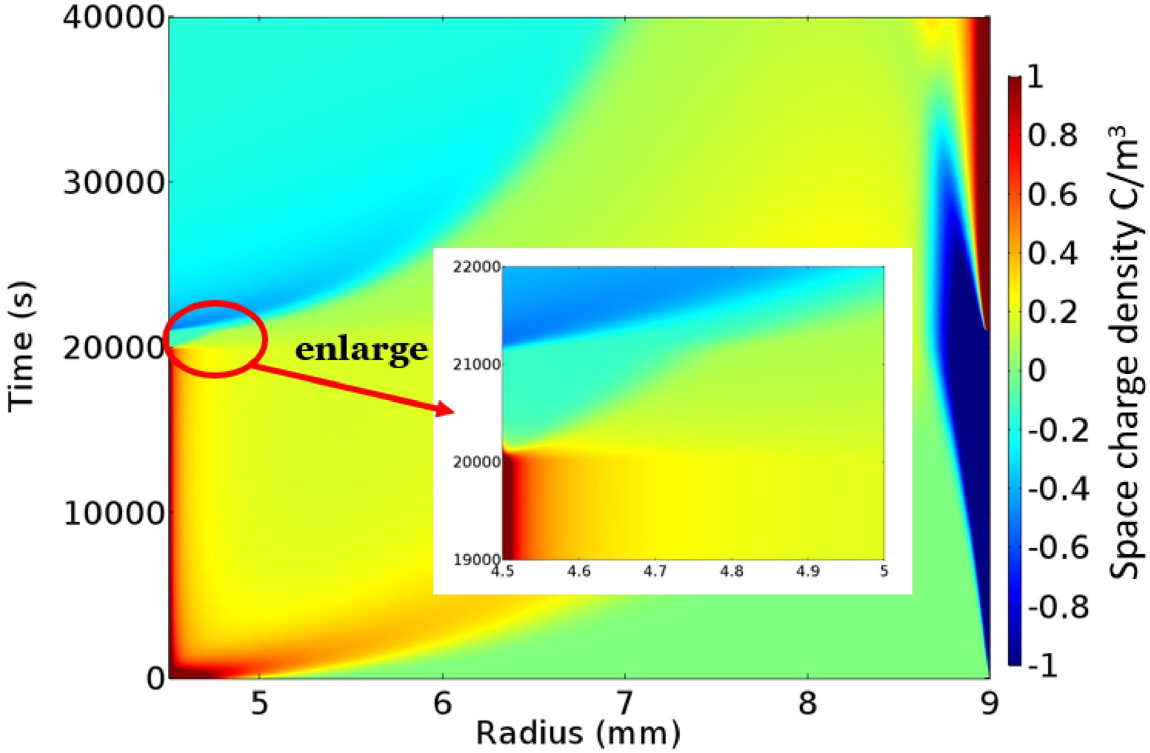

Figure 3-23. Space charge distribution along the insulation radius evolving with time under the slow voltage polarity reversal.

In the case of a slow polarity reversal, the space charge profiles evolving with time are displayed in Figure 3-23, and the overall trend of space charge profiles is similar with the result in the case of a fast polarity reversal. The only difference is the positive charge accumulation near the conductor can be significantly eased by grounding the conductor to earth before the application of the reversed polarity voltage, as pointed out in the enlarged figure. The calculated electric field distribution within the insulation bulk is shown in Figure 3-24. It can be observed that, after the polarity reversal, the field strength at the conductor is enhanced to about -45 kV/mm, which is fairly lower compared with the result in the case of a fast polarity reversal. Indeed, if the cable conductor can be grounded for a longer time, much less space charges will be present within the insulation bulk due to the extraction or to the injection of charge carriers with the opposite polarity, and the field strength at the conductor immediately after the polarity reversal will be lower. At last, the final electric distribution is very similar to the result in the case of a fast polarity reversal.

In conclusion, the bipolar charge transport model is quite adequate to simulate the space charge behaviour and field distribution within the cable insulation subjected to transient voltage, taking into account the operation stages of the HVDC cable systems. In addition, a slow polarity reversal is considered to be preferable as it leads to a much lower field strength at the conductor immediately after the application of the reversed voltage.

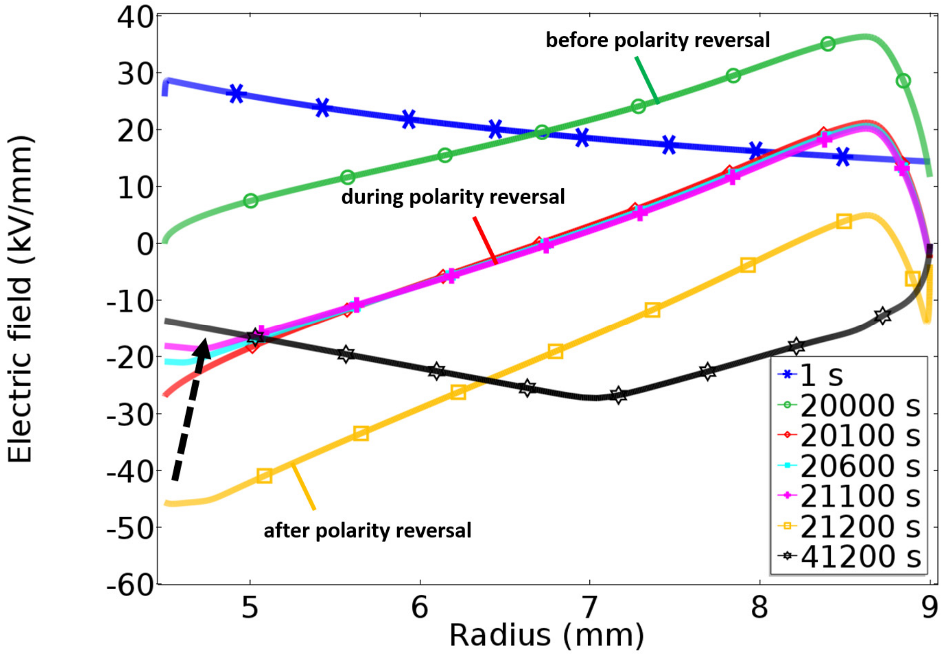

Figure 3-24. The calculated electric field distribution in polymeric cable insulation subjected to a slow voltage polarity reversal.

3.6 Summary

Both the conventional conductivity model and the bipolar charge transport model are introduced and employed to simulate the space charge and field distribution in the MV size polymeric cable insulation. Based on many experimental observations, a threshold electric field at which the charge injection takes place is introduced into the bipolar charge transport model. The bipolar charge injection, the charge conduction mechanism, the charge trapping, detrapping and recombination processes are taken into account in the bipolar charge transport model. In the presence of a steady temperature gradient, the field inversion phenomenon has been observed by both models. Compared with the previous experimental results in the same size polymeric cable under the same electrical and thermal conditions, the simulation results from the bipolar charge transport model are more consistent, and the well-described charge injection and charge transport mechanisms are believed as the main reason for the better performance of the bipolar charge transport model. It is suggested that the ionic charge behaviour need to be further considered into the new modelling approach, which will be introduced in the Chapter 5, and the parameters used for simulation still need to be optimized for a XLPE material. In addition, the bipolar charge transport model is also used to investigate the transient field distribution in cable under the polarity reversal. The considerable field enhancement near the conductor after the polarity reversal has been simulated. It seems the slow polarity reversal is more preferable than the fast one, as the space charge accumulation could be released to some extent during the grounding stage. In consequence, the bipolar charge transport model is suitable to investigate the space charge behaviour under various transients, such as considering the operation stages of the HVDC cable systems.

Chapter 4 Thermal transient effects on space charge behaviour in DC cable insulation

In practical operation of HVDC cable system, the load current flowing in the cable conductor varies with the transmission power according to daily cycles, which would change the temperature gradient across the insulation. Due to high temperature dependence of charge generation and transport mechanisms, it is essential to consider thermal transient effects into the numerical modelling, in order to predict the electric field distribution of the HVDC cable subjected to load cycles. In this chapter, the temperature dependence of charge generation and transport is described and a simple heat transfer model is built within COMSOL to simulate the transient temperature distribution across the insulation. Section 4.2 deals with the impacts of thermal transients with a changing current flowing in the conductor, in order to observe the space charge behaviour and field variation in cable insulation. Furthermore, simulation is also performed by considering a cyclic load, aiming to investigate the electric field distribution under different load conditions.

4.1 Thermal effects and the heat transfer model

Previous research has revealed that space charge accumulation in polyethylene-based material can be highly affected by temperature [106] [107] [108]. Generally, a higher temperature at the electrodes implies a higher charge injection, and also a higher charge mobility. In this study, the space charge and field distributions subjected to time-varying thermal conditions are investigated by modelling via bipolar charge transport theory. The charge injection at the boundaries is described by the Schottky injection law when the applied field exceeds the threshold (10 kV/mm), and for holes the equation is given by,

$$j_h(r_i,t) = AT^2(r)\exp\left(\frac{-ew_{hi}}{k_B T(r)}\right)\exp\left(\frac{e}{k_B T(r)}\sqrt{\frac{eE(r,t)}{4\pi\varepsilon_0\varepsilon_r}}\right) \tag{4-1}$$

A linear conduction function of Ohmic type is used to describe the injection current density when the field strength is below the threshold, and the calculated injection current density from the anode at different temperatures is given in Figure 4-1. It can be observed that the charge generation source is highly dependent on the temperature in the presence of 20 kV/mm electric field. The charge conduction mechanism is described by using a hopping type mobility as a function of field and temperature, as given below,

$$\mu_{e,h}(r,t)=\frac{2d_a v}{E(r,t)}\exp\left(\frac{-ew_{\mu e,\mu h}}{k_B T(r)}\right)\sinh\left(\frac{eE(r,t)d_a}{2k_B T(r)}\right) \tag{4-2}$$

The impacts of electric field and temperature on the mobility for holes and electrons are shown in Figures 4-2a and 4-2b respectively. The variation of temperature from 25℃ to 65℃ has a larger impact on the value of the mobility (increase by more than one order of magnitude), compared with the variation of electric field from 10 kV/mm to 40 kV/mm.

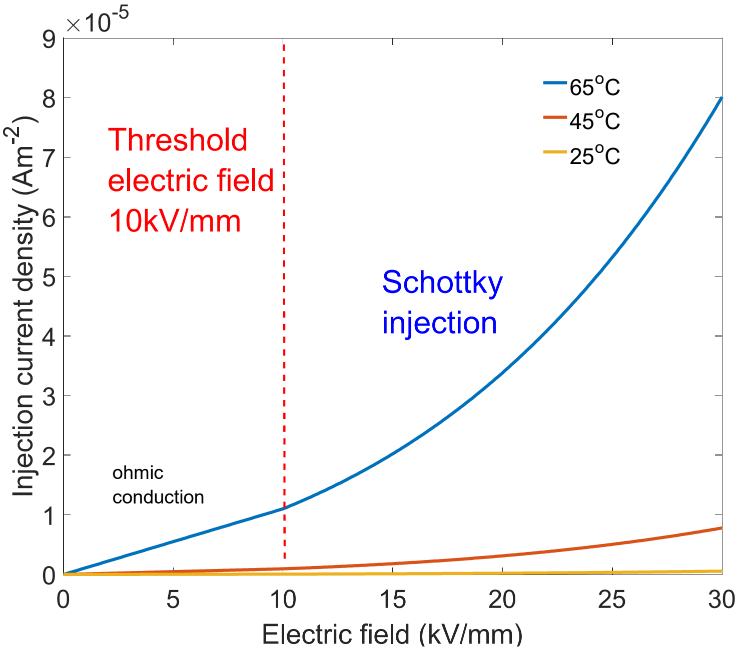

Figure 4-1. Calculated injected current density from the anode at different temperatures.

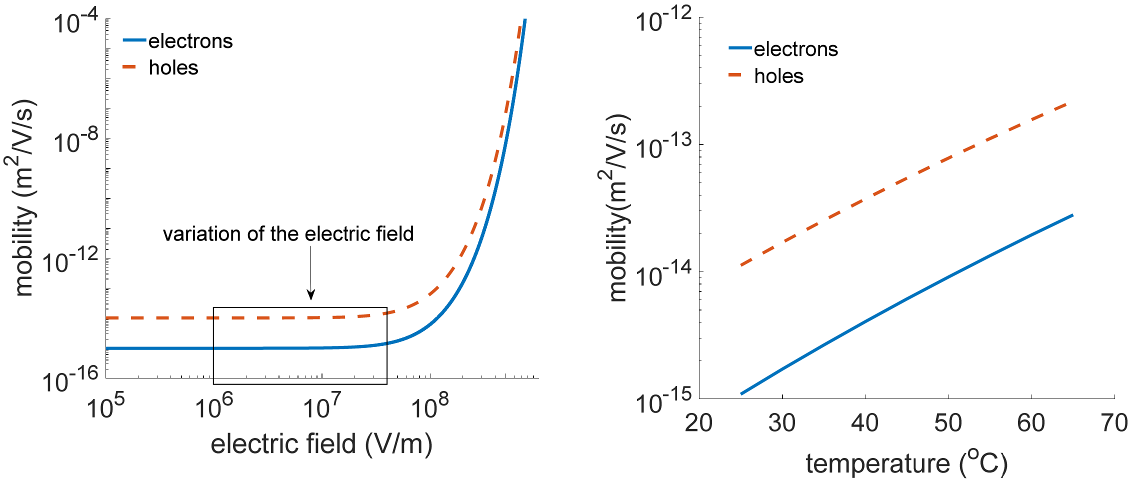

(a)

(b)

Figure 4-2. (a) Calculated mobility as a function of electric field at 25°C. (b) Calculated mobility as a function of temperature at electric field of 20 kV/mm.

In order to achieve a time-varying thermal gradient across the cable, a load current is applied in the core of the MV size cable, which has been used for simulation in last chapter. Heat transfer is described as the movement of energy due to temperature dissimilarity. Based on the time-dependent heat transfer equation shown as following, the dynamic temperature distribution over the insulation thickness could be obtained via modelling of COMSOL Multiphysics.

$$\rho_d C_p \frac{\partial T}{\partial t} = \nabla \cdot (k \nabla T) + Q \tag{4-3}$$

where ρ_d is the material density; C_p is the heat capacity at constant pressure; k is the thermal conductivity; Q is the heat generated from the conductor, of the form:

$$Q = \frac{I^2 \rho_{al}}{A^2} \tag{4-4}$$

where A is the cross section area of the conductor, about 50 mm^2; I is the load current; ρ_{al} is the resistivity of the cable core, which can be expressed as:

$$\rho_{al} = \rho_{20}(1 + \alpha_{20}(T_c - 20)) \tag{4-5}$$

where T_c is the conductor temperature; ρ_{20} is the resistivity of aluminium at 20°C (2.8264×10^{-8} Ω·m); α_{20} is the temperature coefficient of aluminium at 20°C (4.03×10^{-3} 1/K), and these parameters are from IEC standard 60287 [109]. The outer surface of the insulation is cooled by convective heat flux with a heat transfer coefficient of 30 W/(m^2·K), which is used to described the heat transfer at the interface between polymeric material and air environment. The external temperature is set to be the room temperature of 20°C. The parameters used for computing dynamic temperature distribution in the cable is given in Table 4-1.

Table 4-1. Parameters used for heat transfer model [110]

Parameter	Conductor (Al)	Semicon	XLPE
Thermal conductivity (W/(m·k))	205	0.4	0.3
Density (kg/(m^3))	2700	1100	925
Heat capacity at constant pressure (J/(kg·k))	910	2400	2300

It has been identified that, when a current of 300 A is applied to the core of the MV size cable, a quasi-equilibrium (about 65°C-45°C) can be reached after 5000 s heating, and the thermal condition can be maintained in the rest of time, as shown in Figure 4-3. Similarly, a temperature gradient of 10°C (about 40°C-30°C) can be formed after 5000 s with a load current of 200 A flowing in the cable conductor. It must be emphasized that, the simulated thermal conditions in this study cannot be compared with the real temperature distribution in the practical DC cable application. Indeed, the cable structure consists of conductor, inner semicon layer, insulation layer, outer semicon layer, metallic screen, sheath and armouring, etc., and each of them is made of material of different thermal properties. Additionally, the ambient environment can affect the temperature distribution greatly. In this study, for sake of simplification, only the conductor, inner-semicon layer and insulation layer are considered, and the outer insulation surface is considered to be exposed to the air. The aim is to investigate the space charge behaviour in the cable insulation subjected to a time-varying temperature gradient.

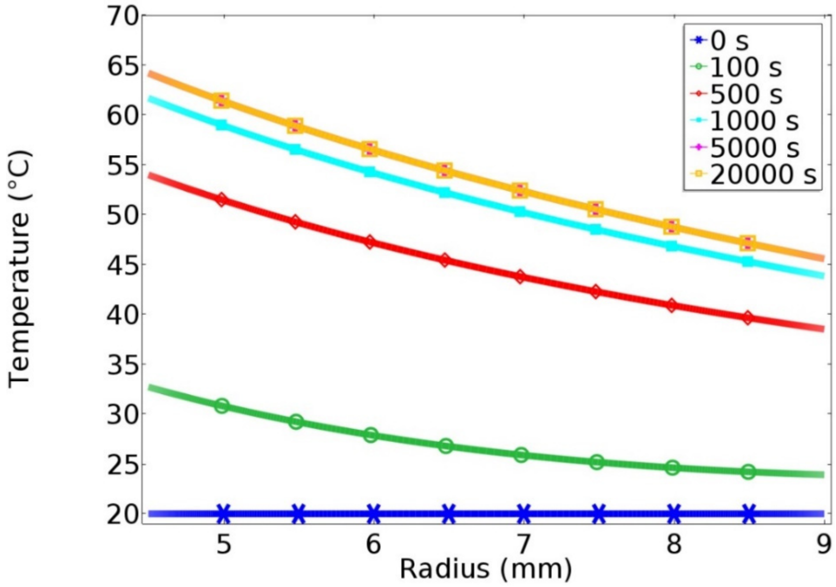

Figure 4-3. Dynamic temperature distribution across the cable insulation with a load current of 300 A.

4.2 Thermal transient effects with a changing load current

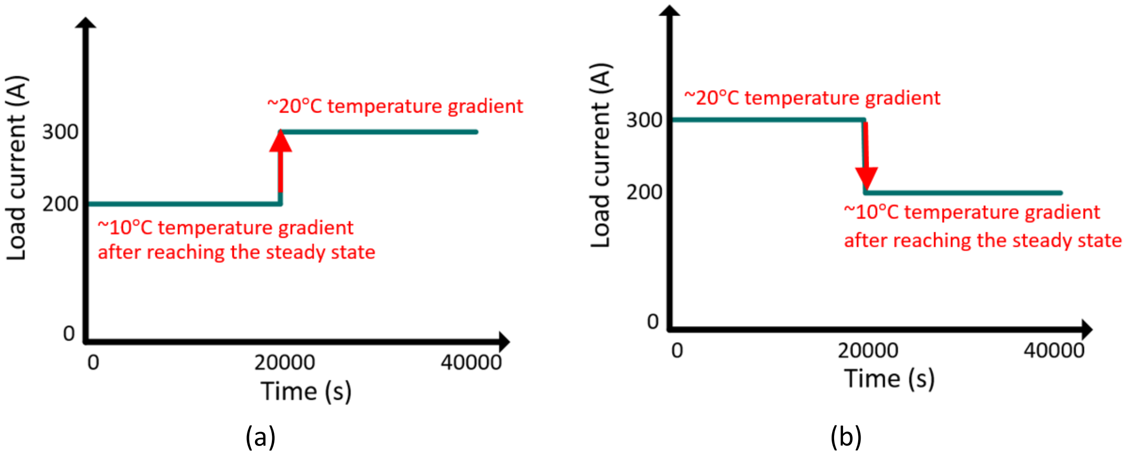

Figure 4-4. (a) The load current changes from 200 A to 300 A. (b) Another load current changes from 300 A to 200 A.

In loaded HVDC cable systems, the current flowing in the conductor varies with the transmission power, and the temperature gradient over the insulation thickness changes at different load conditions. Therefore, it is essential to investigate the space charge dynamics and field distribution under thermal transient. Two cases are considered here, in the first case, the load current flowing in the cable conductor is set to be 200 A in the first 20000 s, then is raised to 300 A for the rest 20000 s. In this situation, the temperature gradient inside the bulk is raised and maintained at 40-30℃ in the first period, and then raised and maintained at 65-45℃ in the rest of time, as illustrated in Figure 4-4a.

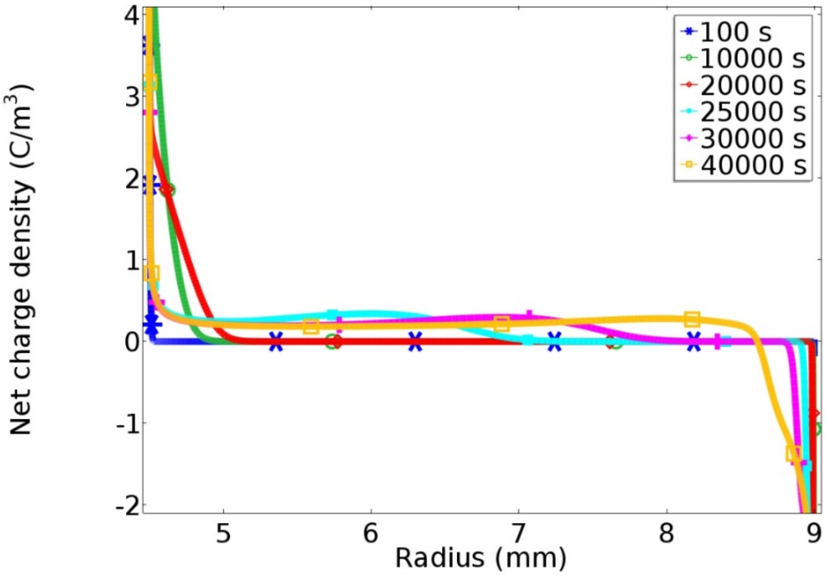

Figure 4-5. The simulated space charge profiles with a changing current (200-300 A) flowing in the core.

Under this thermal transient state, the space charge behaviour and field variation are calculated by employing the bipolar charge transport model. Figure 4-5 shows the space charge density profiles evolving with time. Both the holes and electrons can be observed near the electrodes at the beginning but it seems that they do not penetrate into the volume. Until 20000 s, both positive and negative charge carriers still remain near the electrodes. After 20000 s, the temperature across the insulation is increased significantly, so is the mobility for each type of charge carriers, therefore both holes and electrons can migrate into the bulk quickly. Compared with the results shown in Figure 3-15, the final space charge distribution is very similar. This is particularly surprising as the temperature distribution is very different in the first 20000 s, as if the initial low temperature distribution cannot affect the final charge distribution.

The electric field variation over the insulation thickness is presented in Figure 4-6. It can be observed that the maximal electric field location remains at the inner electrode in the first period (t<20000 s), and the variation is very limited. However, when the overall temperature increases and the temperature gradient is raised up to 20°C, the maximal electric field location shifts from the inner to the outer part gradually. In other words, the stress inversion phenomenon cannot be obtained when the general temperature is relatively low and the temperature gradient is small. Only when it comes to a higher temperature and a larger temperature gradient, the field distribution can be inversed.

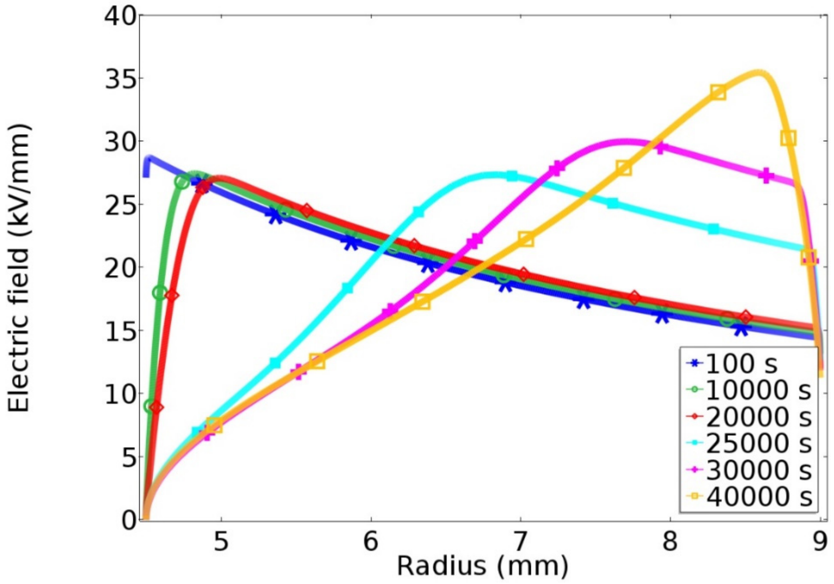

Figure 4-6. The simulated electric field distribution with a changing current (200-300 A) flowing in the core.

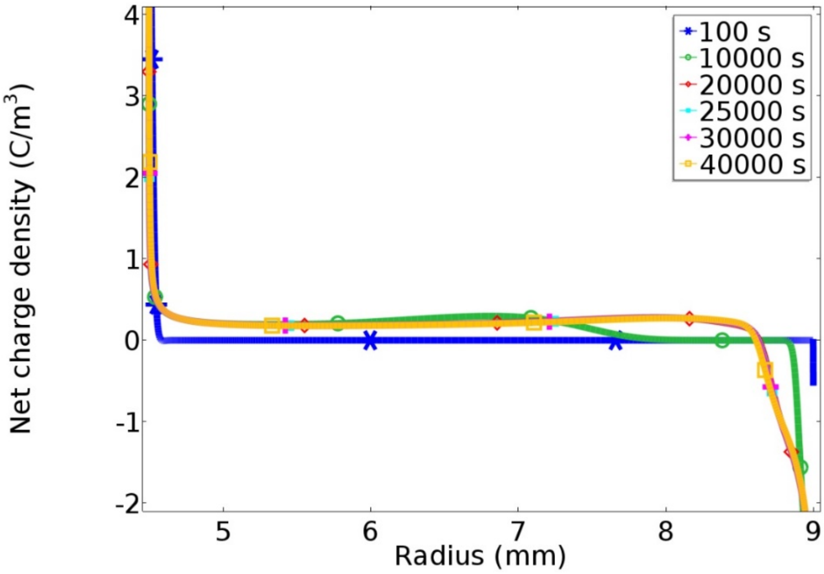

Figure 4-7. The calculated space charge distribution with a changing current (300-200 A) flowing in the conductor.

In another case, the load current is set to be 300 A in the first 20000 s, and then is lowered to 200 A for the rest 20000 s. Therefore, the temperature distribution is raised and maintained at 65-45°C in the first period, then is descended and maintained at 40-30°C in the rest of time, as presented in Figure 4-4b. Figure 4-7 shows the space charge distribution calculated from the bipolar charge transport theory. During the first period (t<20000 s), both holes and electrons penetrate into the volume quickly, due to the large temperature gradient formed in a short time. Interestingly, after the load current is reduced to 200 A, the charge movement almost remain unchanged, and it seems to be frozen at the same position. The electric field distribution also behaves in keeping with the space charge distribution, as presented in Figure 4-8. The maximal electric field location shifts from the inner to the outer insulation in the first period, and then it remains consistent in the rest of time. It can be explained by the highly temperature-dependent mobility of both positive and negative charge carriers, as illustrated in Figure 4-2b. The movement of charge carriers become extremely slow under this relatively low thermal condition. Moreover, much less charge carriers can be injected from the electrodes due to the low electric field and the low temperature in the second period.

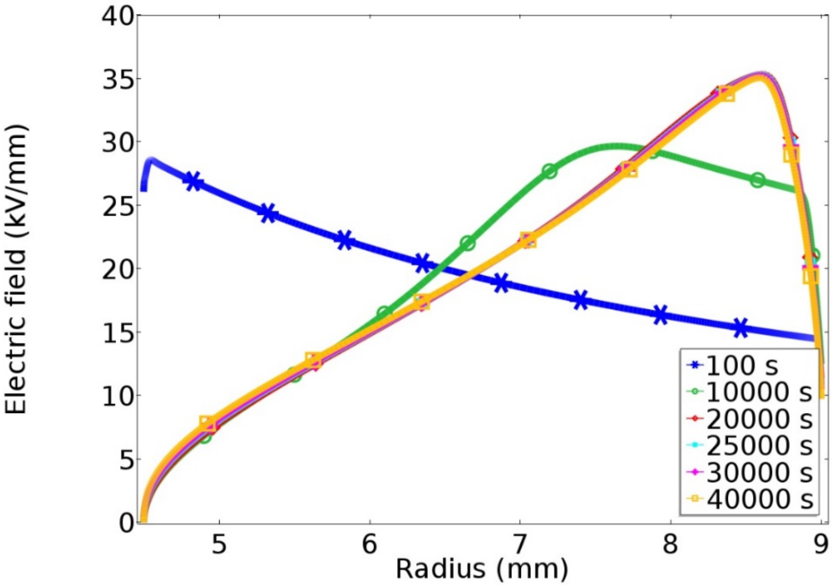

Figure 4-8. The calculated electric field distribution with a changing current (300-200 A) flowing in the conductor.

From the above results it can be concluded that the field inversion can only take place with a higher temperature and a larger temperature gradient. When the MV size polymeric cable is subjected to different temperature gradients with the applied DC voltage of 90 kV, the electric field distributions at the start and at t=50000 s are presented in Figure 4-9. It can be observed that the field inversion cannot take place when the insulation is subjected to a steady temperature gradient of 45-25℃ or in the case of 45℃ isothermal condition. And the value of the final maximum electric field near the cathode is higher in the case of a steady temperature gradient of 65-45℃ than the one in the case of 65-55℃, namely, the larger temperature gradient is, the more severe field inversion can be observed, which has been observed experimentally in literature [58] [111]. It is also worth noting that the predicted maximum electric field location does not change with the decreasing temperature across the insulation, in other words, the field inversion still presents even with a lower load current flowing in the core of cable.

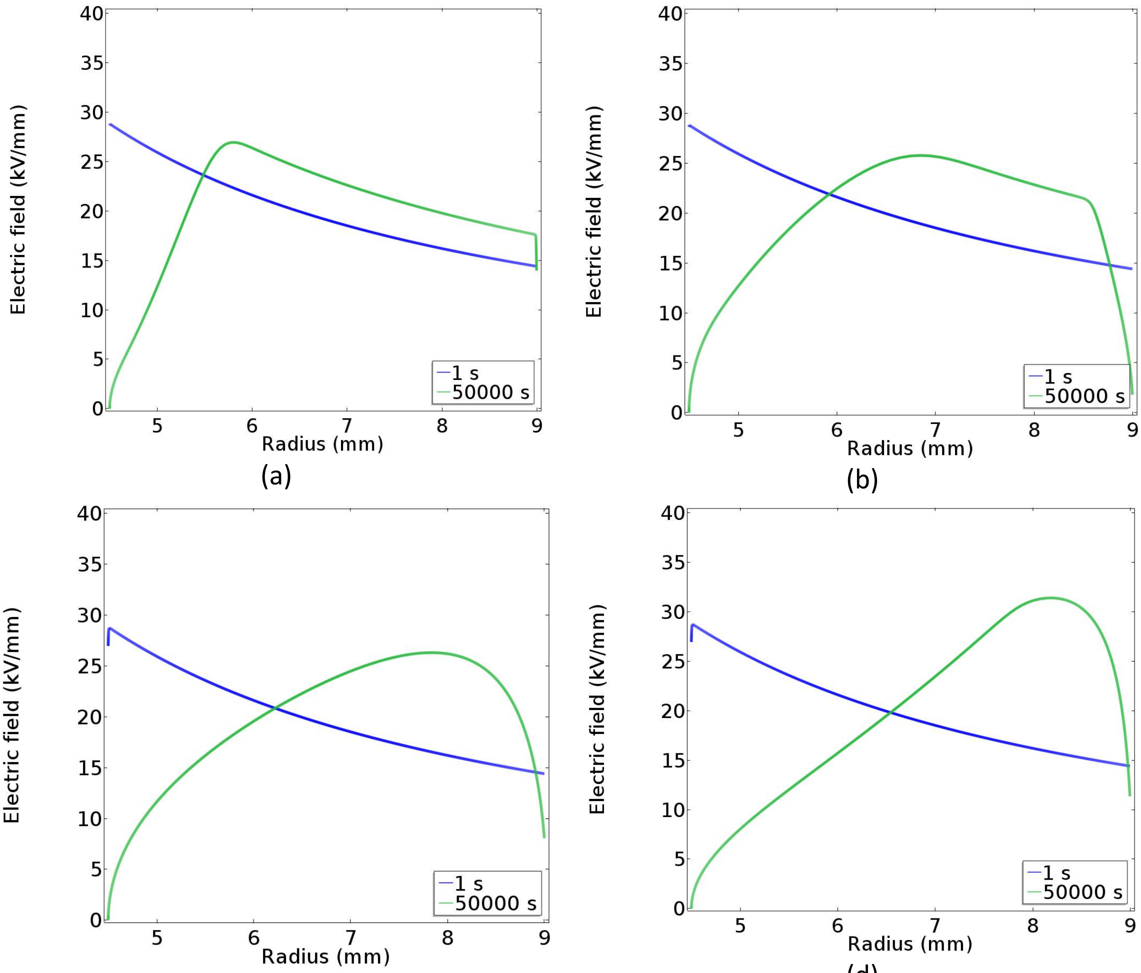

(a) (b) (c) (d)

Figure 4-9. The electric field distribution in polymeric cable at the applied voltage of 90 kV subjected to a steady temperature gradient of (a) 45-25°C (b) isothermal case 45°C (c) 65-55°C (d) 65-45°C.

4.3 Space charge and field distributions in DC cable subjected to cyclic load

Generally, apart from the statistical fluctuations due to the random time-varying nature of the supplied load (e.g. electric power generation from the wind farm) and the deterministic fluctuations associated with the seasonal characteristics of the loads, HVDC cable systems are subjected to daily load cycles [112]. A cyclic load profile shape is characterised by the ratio of time spent at high power to low power and the magnitude of high and low loads as is illustrated in Figure 4-10, where I_{rate} is the high load current and ΔT_{rate} is the time duration of high load periods; I_{low} is the low load current and ΔT_{low} is the time duration of low load periods. In daily load cycles, high load periods generally represent the on-peak demand in the day and low load periods represent the off-peak demand in the night. It is assumed that ΔT_{rate} lasts 16 hours with a current of 300 A flowing in the core of the MV size cable and ΔT_{low} lasts 8 hours with a current of 200 A flowing in the conductor in a single day. In this situation, the transient space charge and field distributions predicted by both traditional conductivity model and the bipolar charge transport model are given in the following. The simulation lasts 3 days, and starts with the high load period.

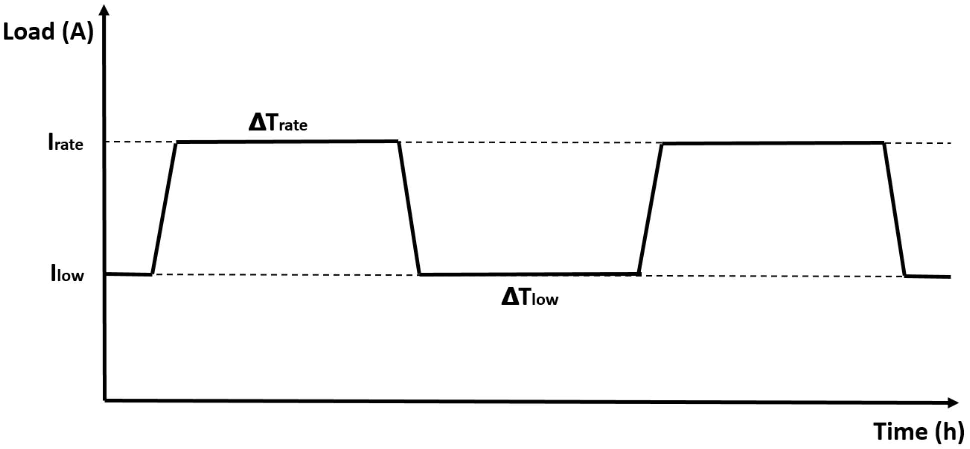

Figure 4-10. Generic cyclic load profile [112].

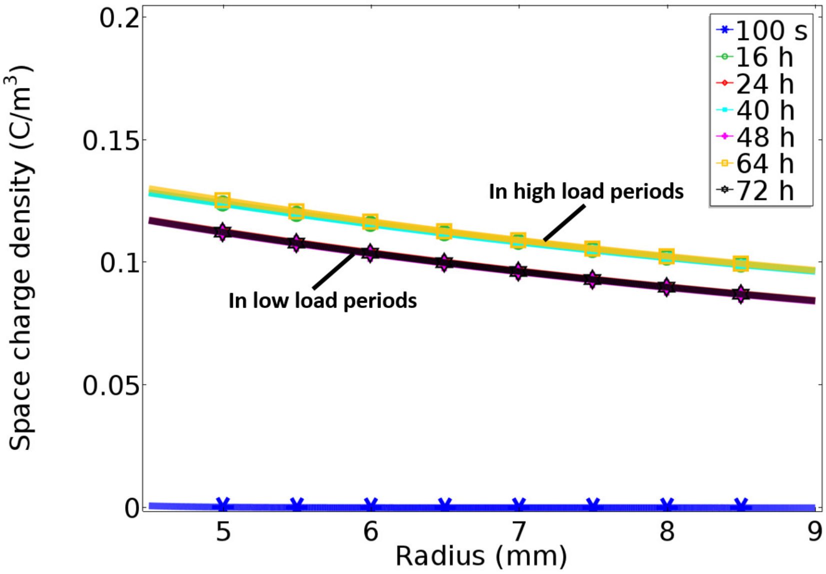

Figure 4-11. Space charge profile calculated by the conductivity model in daily load cycles.

As the Figure 4-11 presents, in the high load periods (0-16 h) (24-40 h) (48-64 h), three similar stationary charge distributions can be obtained, and the accumulated space charge densities are generally higher than the ones formed during the low load periods (16-24 h) (40-48 h) (64-72 h). It is due to the magnitude of the conductivity decreases significantly with the temperature dropping, and both the inversed field distribution and the lower temperature gradient contribute to form a gentler current density gradient across the insulation. Correspondingly, the electric field distributions in the high load periods are different from the ones formed in the low load periods, as presented in Figure 4-12, and the slopes of the electric field gradients in the high load conditions are bigger.

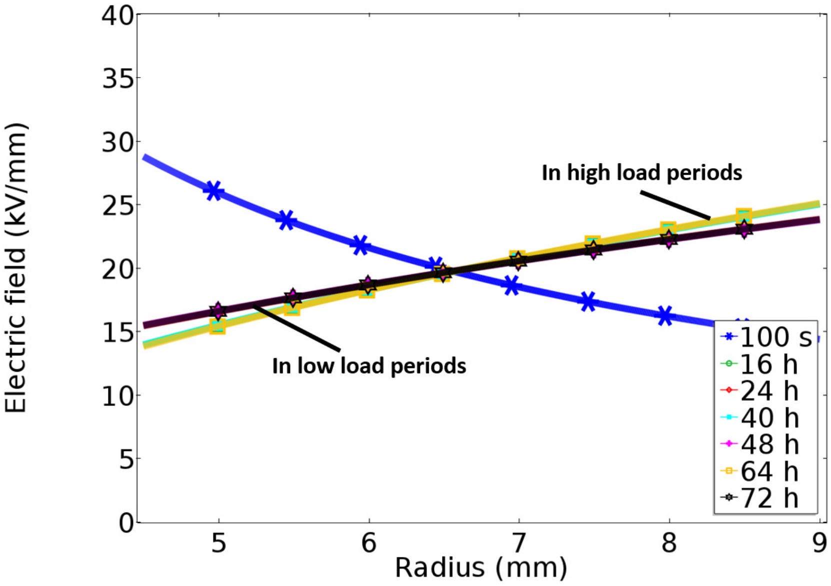

Figure 4-12. Electric field distributions calculated by the conductivity model in daily load cycles.

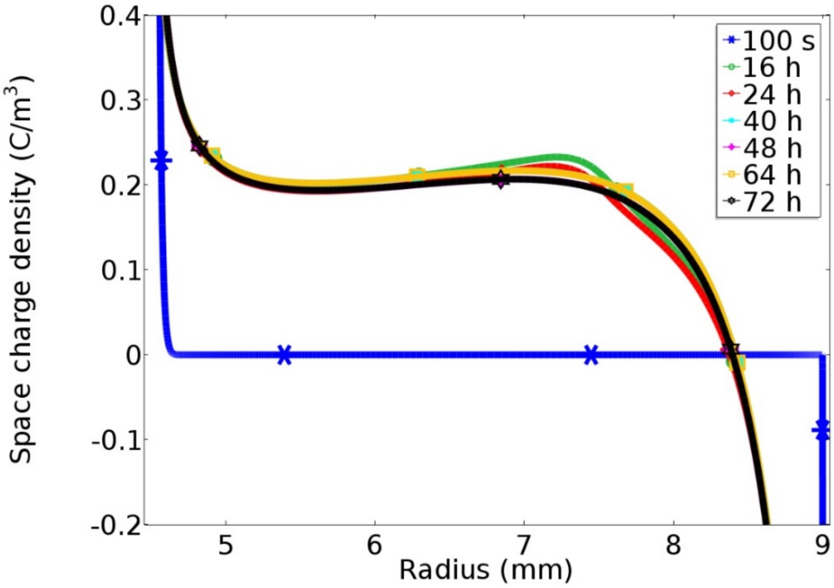

Figure 4-13. Space charge distributions calculated by the bipolar charge transport model in daily load cycles.

Figure 4-13 presents the transient space charge distributions under the daily load cycles simulated by the bipolar charge transport model. It should be noted that the y-axis has been truncated in order to better observe the movement of charges within the insulation bulk. The bulk has been charged adequately by both positive and negative charge carriers after the first high load period (0-16 h), and it can be observed that the following variation of space charge accumulation in different load periods is very limited. In the first high load period (0-16 h), the electric field strengths at both electrodes are decreased significantly by the presence of considerable homo charges, leading to poor injection current densities at both electrodes, and much less charge carriers can be injected with restricted movement during the low load periods due to the lower temperature. The high load periods may lead to a slightly larger charge accumulation inside the bulk and a gently higher maximum field strength at the outer insulation, as shown in Figure 4-14. The location of the maximum field strength always remains at the outer insulation, whether the cable is subjected to a high or low load current.

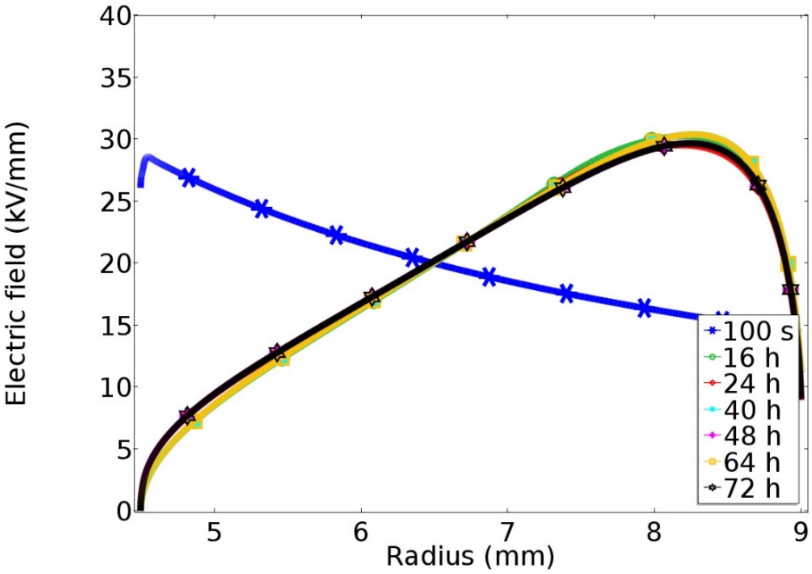

Figure 4-14. Electric field distributions calculated by the bipolar charge transport model in daily load cycles.

Both the output results calculated from the traditional conductivity model and the bipolar charge transport theory indicate that the effect of daily load cycle on the charge and field distribution in the cable insulation is inconspicuous. The final space charge and field distribution mainly depends on the high load period, and the impact of a low load current on the charge behaviour can be almost neglected. The maximum field strength always locates near the outer sheath. In consequence, the bipolar charge transport model is able to simulate the space charge behaviour in the cable insulation subjected to cyclic load by considering the temperature-dependent charge injection and conduction, and the electric field distribution under the high load period needs to be taken into account in DC cable design.

4.4 Summary

The bipolar charge transport model is employed to investigate the space charge behaviour in cable insulation subjected to transient temperature distribution. By applying a changing current to the cable core, it is found that the field inversion can only take place with a high load current which represents a higher general temperature and a larger temperature gradient, and this phenomenon can still present even with the temperature decreasing. Simulation has been performed to study the space charge dynamics in cable insulation subjected to daily load cycles. The results suggest that the maximum electric field strength is always maintained near the outer insulation, and both the charge and field distribution are mainly dependent on the high load period. These results need to be considered when designing the DC polymeric cable systems, since the temperature-dependent space charge accumulation is a degradation acceleration factor and the temperature distribution across the cable can change significantly with loading conditions.

Chapter 5 Modified bipolar charge transport model by considering ionization process

Cross-linked polyethylene, commercially known as XLPE, exhibits a desirable combination of properties for being applied as the main insulation of power cables. It is widely used in HVAC cable systems and now it has been also successfully applied in HVDC systems since the development of High Voltage Self-Commutated Voltage Converter (VSC) technology. However, space charge accumulation under DC field is one of the major technical problems in HVDC XLPE insulated cable operation and design. Previous research has verified that space charge in XLPE may be generated from the charge injection or from the ionization process of some dissociable chemical species, such as crosslinking by-products, antioxidants and other impurities. In the light of this, this chapter aims to simulate the space charge behaviour in XLPE by considering the formation of hetero charges. Space charge measurements have been carried out on LDPE, fresh and degassed XLPE samples, in order to observe and compare the homo charge and hetero charge formation. A modified bipolar charge transport model by considering the dissociation of impurities is proposed and employed to simulate the space charge behaviour in XLPE.

5.1 Hetero-charge formation

Many researchers have studied the space charge behaviour in polymeric insulation materials by using the space charge measurement techniques. Hozumi et al. found that hetero charges tend to be formed in XLPE cable insulation when the applied DC field is at 20 kV/mm, owing to dissociation of impurities within the insulation bulk [71]. Takeda et al. reported that the hetero charges were formed due to the presence of thermally dissociated antioxidant, and the crosslinking by-products such as acetophenone also assisted the hetero charge formation [113]. Sekii et al. also found that the combination of acetophenone and moisture is responsible for hetero charge creation [114]. By investigating the effects of crosslinking by-products on charge formation individually, Maeno et al. reported that acetophenone accounts for hetero charge accumulation, which presents presumably as a synergistic effect with water [115]. The impacts of thermal treatment on XLPE thick samples have been investigated by Fu et al., and it was found that the residues behave like ion-pairs which contribute to hetero charge formation [40]. With the observation of fast charge packets in XLPE samples under high DC field (over 20 kV/mm), it can be debated that the blocked extraction of injected charge carriers also assists the hetero charge formation [59]. In addition to these, the properties of the semicon/insulation interface may play a major role in charge accumulation, as the contained impurities may diffuse into the bulk, assisting the formation of hetero charges [116]. However, it is still difficult to distinguish whether the hetero charges are partially blocked charge carriers at the extraction electrodes or dissociated ionic charges, as the space charge measurement results only reveal net charge density, and the ionic charge behaviour in polymeric insulation is still indistinct.

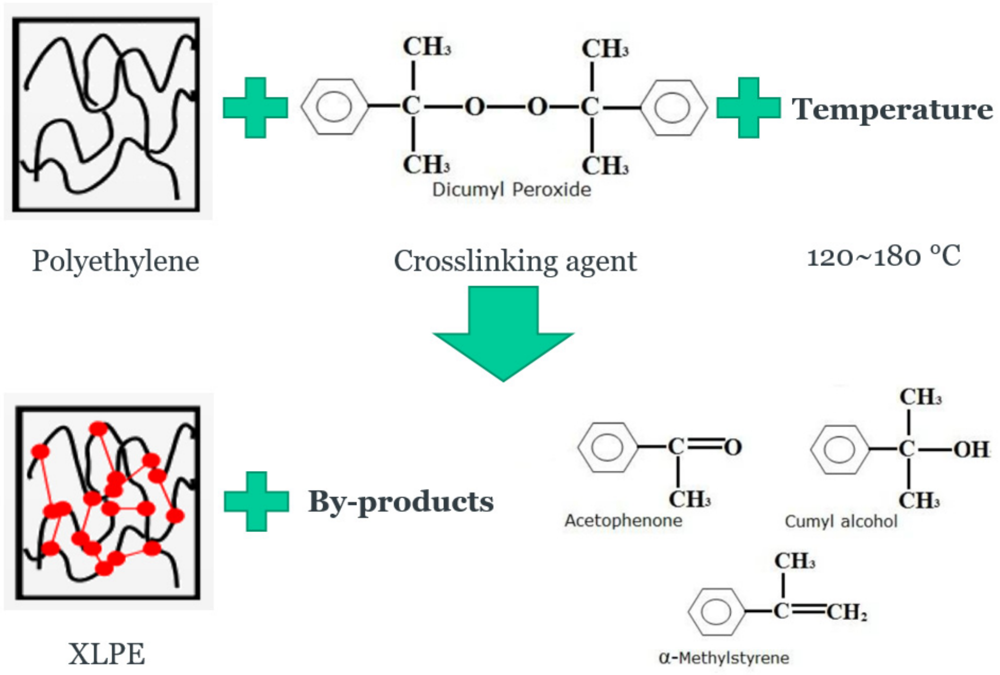

Figure 5-1. Crosslinking process induced by peroxide (crosslinking agent) [117].

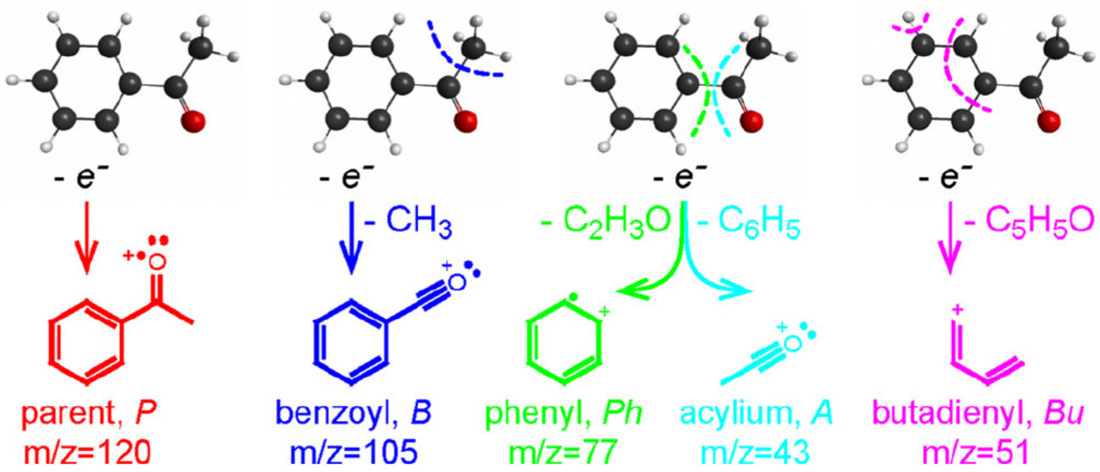

Figure 5-2. Schematic illustrations of acetophenone showing the dissociation pathways to produce the five most prominent peaks in the mass spectra [118].

Figure 5-1 illustrates the peroxide-induced crosslinking process, which is the most common way in crosslinking polyethylene by using Dicumyl peroxide (DCP) as the crosslinking agent in the medium and high voltage cable industry [119]. During this process, several crosslinking by-products are formed and the main ones are acetophenone, cumyl alcohol and α-methylstyrene, which are believed to contribute to hetero charge formation in HVDC XLPE insulated cable. Although the degassing stage can remove most of the volatile crosslinking by-products, the effect of remains still cannot be neglected [117]. The content of acetophenone has been measured in the acetophenone-soaked LDPE films before and after the space charge test respectively, and the results showed that the accumulation of hetero charges might be attributed to the dissociation of acetophenone [120]. By investigating the space charge behaviour in cumyl alcohol-soaked LDPE, it was speculated that the negative ions and protons, or the positive ion and electrons could be formed due to the dissociation of crosslinking by-products [121]. According to the dissociation pathways of acetophenone under the excitation schemes (such as laser radiation), electrons and positive ions can be formed, as shown in Figure 5-2 [118]. However, the ionic dissociation mechanism of the crosslinking by-products is still vague, and the types of ions created by introducing crosslinking by-products also need to be identified.

In addition to the laboratory experiments of measuring space charge, modelling and simulation can assist to comprehend and analyse material behaviour. The bipolar charge transport theory has been successfully applied to simulate the charge dynamics in low-density polyethylene, as illustrated in section 3.3.1, and some emphasis has been put on simulating space charge accumulation in XLPE sheets under DC field by considering the restricted charge extraction [122]. However, the bipolar charge transport model does not consider the hetero charge formation contributed from the ionization process. The numerical modelling of space charge originated from the dissociation of impurities is still in infant stage [123], hence, in this chapter, some assumptions and modifications are made on the bipolar charge transport model to study the hetero charge accumulation in XLPE.

5.2 Experimental procedure

Space charge distributions in three kinds of samples, including additive-free LDPE film, fresh and degassed XLPE flat samples, are measured under an applied DC field of 20 kV/mm at room temperature (25℃), by employing the PEA measurement system. The top and bottom electrode are semi-conductive material and aluminium respectively. LDPE has been chosen as the reference in this study, because it is not only the base material for XLPE, and it does not contain any by-products or additives able to dissociate. A DC field of 20 kV/mm has been chosen as it is not only higher than the threshold field at which the charge injection takes place in polymers, but also suitable to better observe the generation of ionic charges. Additionally, it is also the desired average electric field in further development of DC cables. The thickness of all the prepared samples is about 180 μm. The measurement has been repeated three times on each kind of samples to ensure the accuracy and validity.

5.2.1 Sample preparation

The additive-free LDPE film is supplied by the GoodFellow Cambridge Ltd., and the film with a thickness of 180 μm is cut into circular samples. The XLPE pellets used in this study are produced from the Borlink^{TM} Technology, which has been mixed with 2 % Dicumyl peroxide (DCP) already, and the crosslinking is performed by using a hot press. The initial temperature is set at 120°C for 5 minutes, and then the temperature of 180°C is applied to activate the crosslinking process for 10 minutes. The applied load (5 tons) is maintained during the cooling process and the samples are removed from the hot press once 100°C is reached and further cooled at room temperature. Degassing of the XLPE samples is carried out in a vacuum oven at a constant temperature of 80°C for 3 days, with the aim of expelling volatile residual by-products and to highlight any influence this may have on the material performance. The samples are then cooled down to room temperature and sealed in polyethylene bags, prior to tests. The sample preparation flow is shown in Figure 5-3.

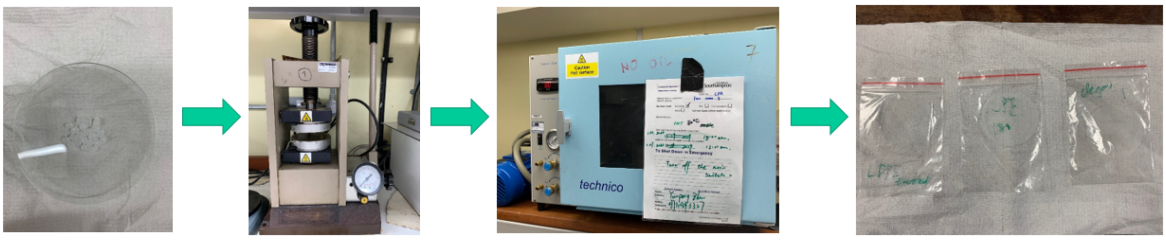

Figure 5-3. Sample preparation flow.

5.2.2 Space charge measurement

The space charge behaviour in LDPE film is shown in Figure 5-4. It is clear to observe the obvious homo charge distribution within the insulation bulk. A large amount of positive charge carriers is injected from the anode and they move towards the cathode, while the accumulation of negative charge carriers near the cathode is fairly limited. Actually, the charge detected at the interface of electrodes are contributed from the capacitive charge which is induced by the polarization of the dielectric material under a DC field, and the surface charge induced by the accumulated space charge inside the insulation bulk. Generally, the quantity of capacitive charges is much larger than the accumulated charges, which could hinder observing space charge accumulation inside the bulk. Moreover, the space charge modelling method only simulates the space charge dynamics inside the bulk. Therefore, in this study, in order to achieve the comparability of the measured data and the simulation results, the capacitive charges at the electrodes have been removed by utilizing the subtraction process proposed by Liu et al [102]. The accumulated charge density after subtraction, ρ_{acc}, can be obtained by applying equation 5-1,

$$\rho_{acc}(x) = \rho_{test}(x) - \frac{V_{applied}}{V_{ref}}\rho_{ref}(x) \tag{5-1}$$

where $V_{applied}$, V_{ref} are the applied voltage and the reference voltage respectively, and ρ_{test}, ρ_{ref} are the measured charge density and the reference one respectively.

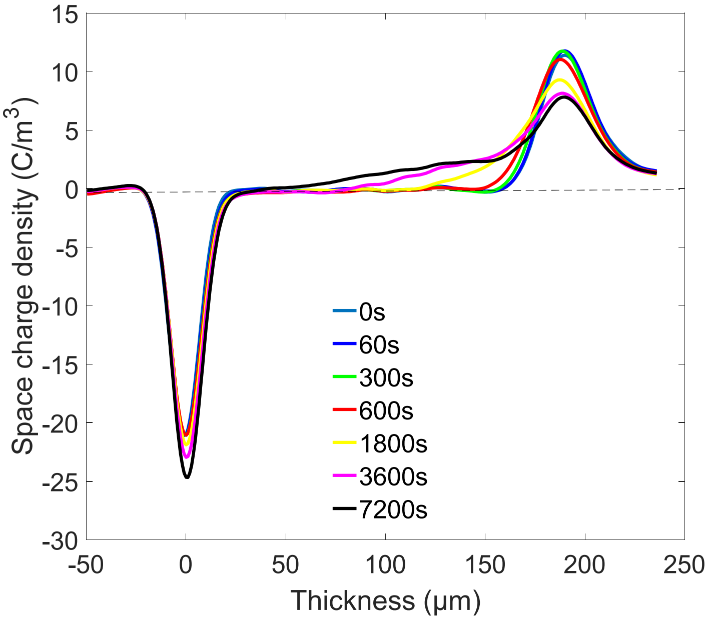

Figure 5-4. PEA measurement results in LDPE film at 20 kV/mm field under room temperature.

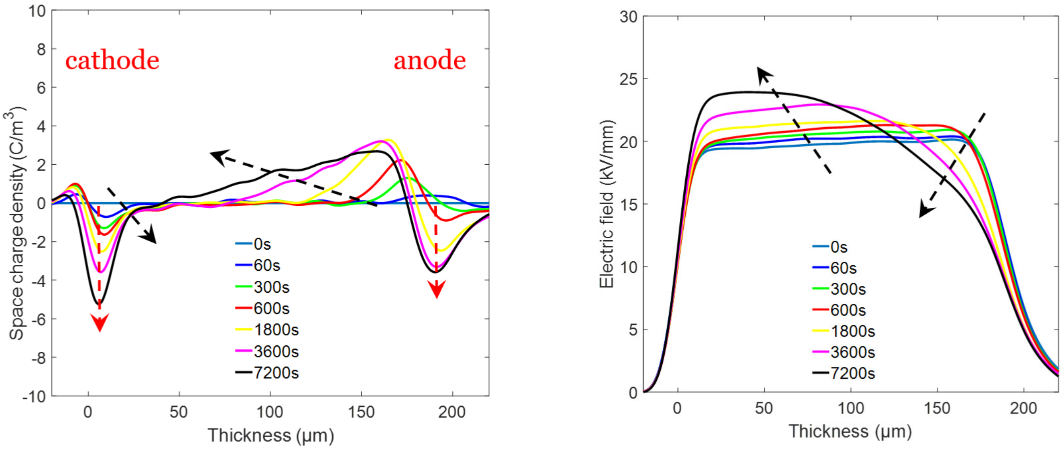

(a) (b)

Figure 5-5. (a) Space charge behaviour in LDPE film at 20 kV/mm field at room temperature (capacitive charge removed). (b) Electric field distribution over the insulation thickness of the LDPE.

Figure 5-5a presents the space charge behaviour in LDPE sample after the subtraction process, and only the accumulated charge inside the bulk and the induced charge at the electrodes remain. The movement of both positive and negative charge carriers can be observed much more clearly. The large positive charge accumulation affects the electric field distribution greatly, as presented in

Figure 5-5b. The field strength near the cathode is enhanced from 20 to 24 kV/mm, while it is strongly reduced in the vicinity of anode.

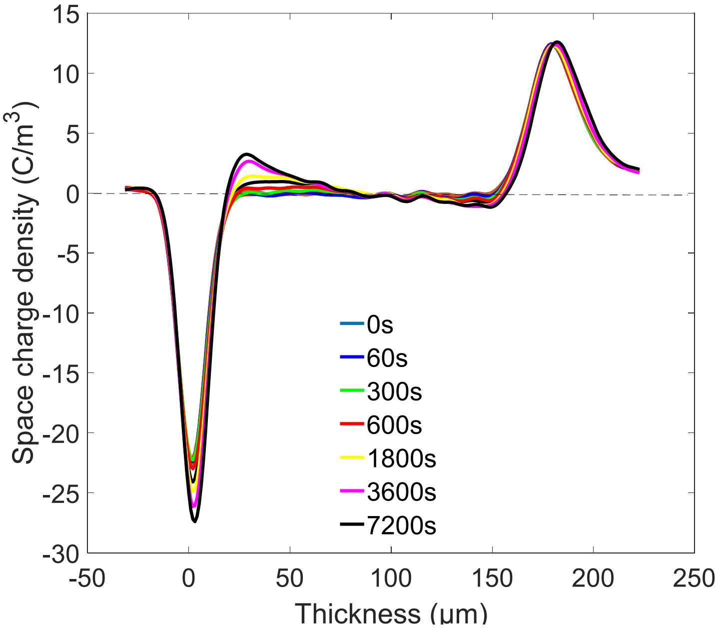

Figure 5-6. PEA measurement data in fresh XLPE samples at 20 kV/mm field at room temperature.

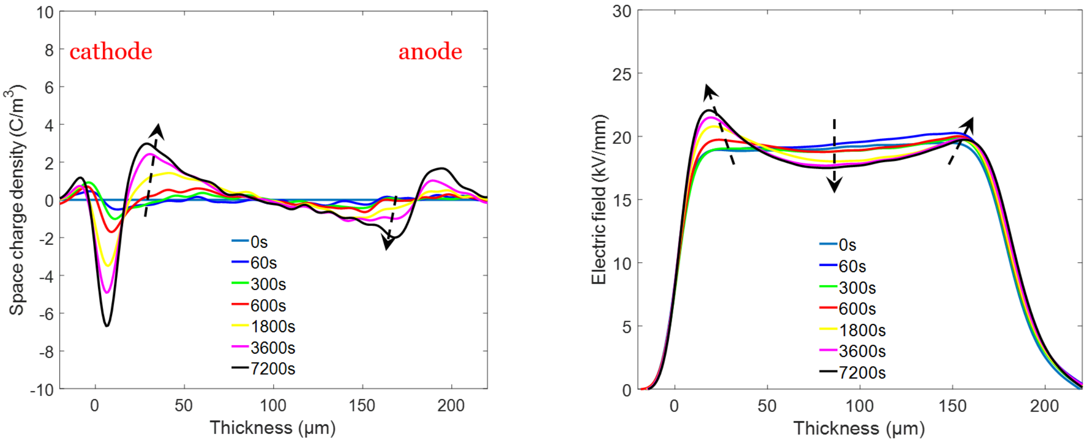

(a) (b)

Figure 5-7. (a) Space charge behaviour in fresh XLPE samples at 20 kV/mm field (capacitive charge removed). (b) Electric field distribution across the fresh XLPE film.

The space charge profiles in the fresh XLPE sample is shown in Figure 5-6. After removing the capacitive charge, the hetero charge formation in the fresh XLPE can be clearly observed, as given in Figure 5-7a. The accumulation of hetero charges at both electrodes increases with time. It seems that the amount of positive charge carriers near the cathode is larger than the amount of negative ones at the adjacent electrode. Due to the presence of hetero charge accumulation, the field distribution is deformed greatly, as shown in Figure 5-7b. After 2-hour poling, the maximum electric field location is in the vicinity of cathode, and the field strength in the middle of the dielectric is strongly reduced.

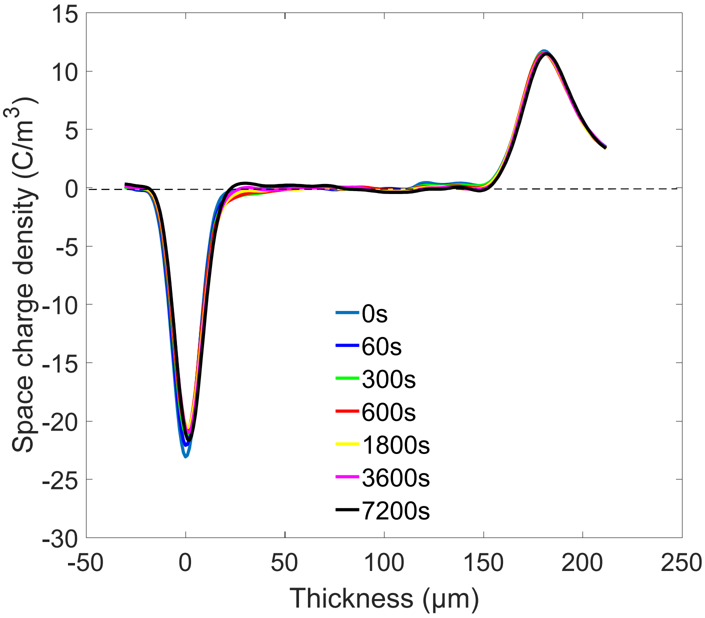

Figure 5-8. PEA measurement results in the degassed XLPE samples at 20 kV/mm field at room temperature.

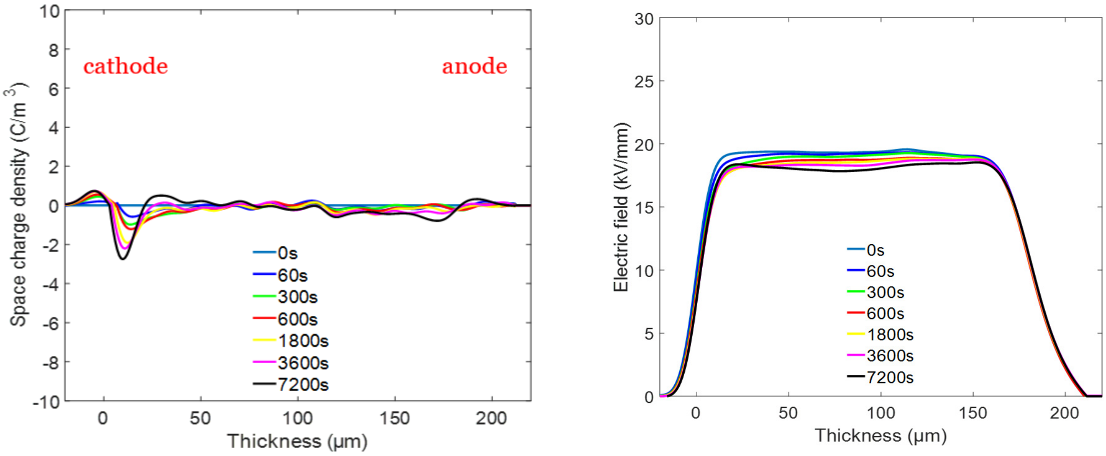

(a) (b)

Figure 5-9. (a) Space charge behaviour in degassed XLPE samples at 20 kV/mm field (capacitive charge removed). (b) Electric field distribution across the degassed XLPE film.

Figure 5-8 shows the space charge profiles in the degassed XLPE sample at the room temperature. Since most volatile crosslinking by-products have been removed from the bulk, only very limited charge accumulation can be detected inside the insulation bulk. After removing the capacitive charge at the electrodes, a small amount of hetero charges can be observed in the vicinity of both electrodes at last, as shown in Figure 5-9a. Due to the limited charge accumulation inside the bulk, the electric field distribution is nearly unchanged, as presented in Figure 5-9b.

From the experimental observations it can be concluded that, at an applied field of 20 kV/mm, homo charge distribution is dominant in LDPE, and the amount of accumulated charges (mainly positive charge) increases with time. Similar profiles are always measured for pure LDPE under low applied voltage at room temperature [124]. For fresh XLPE samples, the considerable accumulation of hetero charges can be detected in the vicinity of both electrodes, the presence of hetero charges enhances the electric field near the cathode effectively, which could lead to more charge carriers being injected from the electrode. It should also be noted that the negative charge carriers behave differently from the positive ones, and this is considered to be the combination effects of injection and ionization processes that work together. Compared with the measured data of the degassed XLPE samples under the same applied field, it can be speculated that the hetero charge formation is related to the ionization of the dissociable impurities, such as crosslinking by-products. The detected limited charge accumulation in the degassed XLPE indicates that there might be still some residual crosslinking by-products inside the bulk.

5.3 Space charge modelling methods

In this section, a bipolar charge transport model and the modified model by considering the ionization of dissociable species will be employed to simulate the space charge dynamics in LDPE and XLPE samples separately. The electrical and thermal conditions are set to be same as the experiments. Both models are implemented by using COMSOL Multiphysics. The “Transport of Diluted Species”, the “Heat Transfer in Solids” and the “Electrostatics” modules have been applied to simulate the charge dynamics migrating in electric field. The thickness of the sample is divided into 180 divisions equally.

5.3.1 Bipolar charge transport model

The basics of bipolar charge transport theory has been described in detail in section 3.3.2, and it features the bipolar injection of electronic charge carriers from the electrodes. The injected electrons and holes migrate towards the opposite electrode respectively, with the possibility to be imprisoned by “traps”. The trapped charge carriers can also be released as the free ones and the recombination may take place when the charge carriers with opposite polarity encounter, leading to electroluminescence. Generally, the holes and electrons (including trapped and mobile ones) are distributed along the insulation thickness as illustrated in Figure 5-10. The concentration gradient of holes is higher near the anode and lower at the cathode, and the electrons distribute conversely. Therefore, the net charge distribution is always presented as a homo charge accumulation.

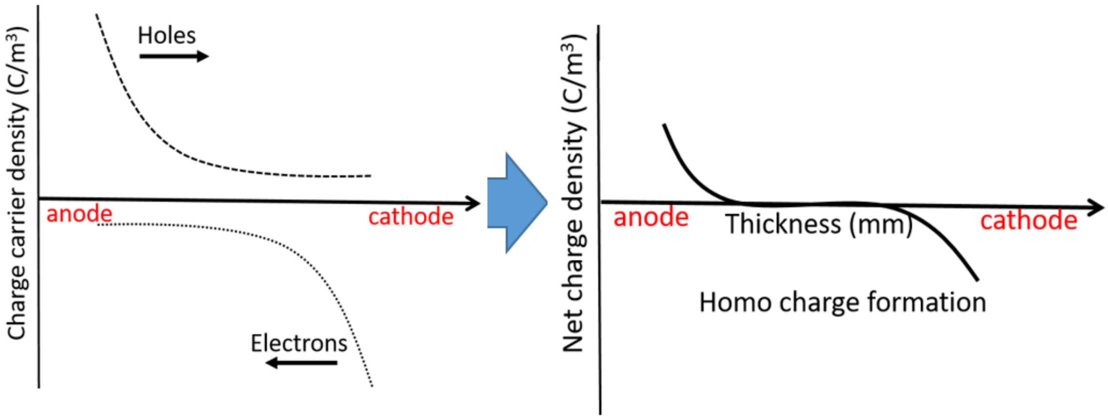

Figure 5-10. Schematic diagram of charge carrier distribution and net charge distribution modelled by bipolar charge transport model (not to scale).

Here the theory is used for modelling space charge behaviour in planar LDPE sample, and the three space and time dependent equations, the Poisson's equation, the continuity equation and the transport equation, are presented in plane geometry:

$$\frac{\partial E(x,t)}{\partial x} = \frac{\rho(x,t)}{\varepsilon_0 \varepsilon_r} \tag{5-2}$$

$$\frac{\partial n_{a\mu,at}(x,t)}{\partial t} + \frac{\partial j_a}{\partial x} = s_{a\mu,at}(x,t) \tag{5-3}$$

$$j_a(x,t) = \mu_a(x,t) n_{a\mu}(x,t) E(x,t) - D_f \frac{\partial n_a(x,t)}{\partial x} \tag{5-4}$$

where j_a is the conduction current density; n_a is the charge carrier density; a refers to the type of charge, and the subscript μ or t refers respectively to mobile or trapped charge; E is the electric field, ρ is the net charge density; ε_0 is the vacuum permittivity and ε_r is the relative dielectric permittivity for polyethylene. D_f is the diffusion coefficient, which is referred to describe the natural motion of chemical species based on the space gradient of particle concentration. The diffusion term is generally neglected in the transport equations when dealing with technical insulating polymer, so that only the drift current is considered, as the simulation work presented in Chapter 3.3. Reasons lay on the fact that concentration gradients are generally not very strong and also that the nature of charge carriers is essentially unknown and so it is for the corresponding diffusion coefficients. Indeed, after a study of its impact on the simulation results, it has been identified that the simulation results can hardly be affected if only a relatively small diffusion coefficient (such as 10^{-12} m^2/s) was considered. The aim of the addition of diffusion term is to get rid of numerical errors when dealing with ionic charge migrating in the modified model, which will be illustrated later.

The parameters used in the bipolar charge transport theory are almost consistent with the ones given in Table 3-3, and only the hopping type of mobility is replaced by a constant effective mobility of charge carriers to describe the charge migration process under the constant DC field at room temperature, as shown in Table 5-1.

Table 5-1. Parameters used for simulating space charge in LDPE [57].

Symbol		Value	Unit
Injection barrier height	w_{ei} for electrons w_{hi} for holes	1.27 1.20	eV eV
Trapping coefficient	B_e for electrons B_h for holes	0.05 0.05	s^{-1} s^{-1}
Charge carrier mobility	μ_e for electrons μ_h for holes	2×10^{-15} 1×10^{-14}	$m^2/(V\cdot s)$ $m^2/(V\cdot s)$
Detrapping barrier height	w_{tre} for electrons w_{trh} for holes	0.95 0.95	eV eV
Trap density	n_{oet} for electrons n_{oht} for holes	100 100	C/m^3 C/m^3

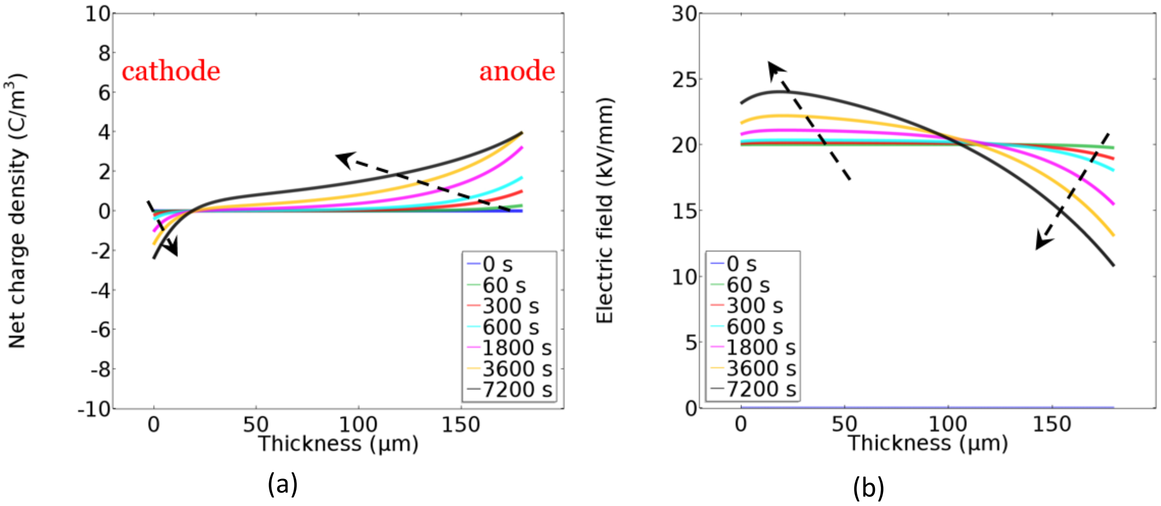

Figure 5-11. (a) The calculated space charge distribution in the LDPE sample at 20 kV/mm field. (b) Calculated electric field distribution over the thickness of LDPE film.

The simulated homo charge distribution in LDPE samples is presented in Figure 5-11a. After the application of DC voltage, much more holes are injected into the insulation bulk than the electrons, and the migration of holes is much deeper compared with the accumulation of electrons in the vicinity of cathode. This is because the assumptions of lower injection barrier height and higher charge mobility for holes as shown in Table 5-1. It can be observed that the positive charge carriers distributed extensively in the LDPE sample after 2 hours' polarization, while the penetration of negative ones is still very limited. The presence of the large amount of accumulated homo charges will distort the field distribution severely, as shown in Figure 5-11b. Following the movement of positive and negative charge carriers, the electric field strength near the anode decreases, but increases gradually at the cathode. Finally, the maximum electric field locates near the cathode and reaches a value of 24.5 kV/mm, which is consistent with the result experimentally observed in LDPE samples.

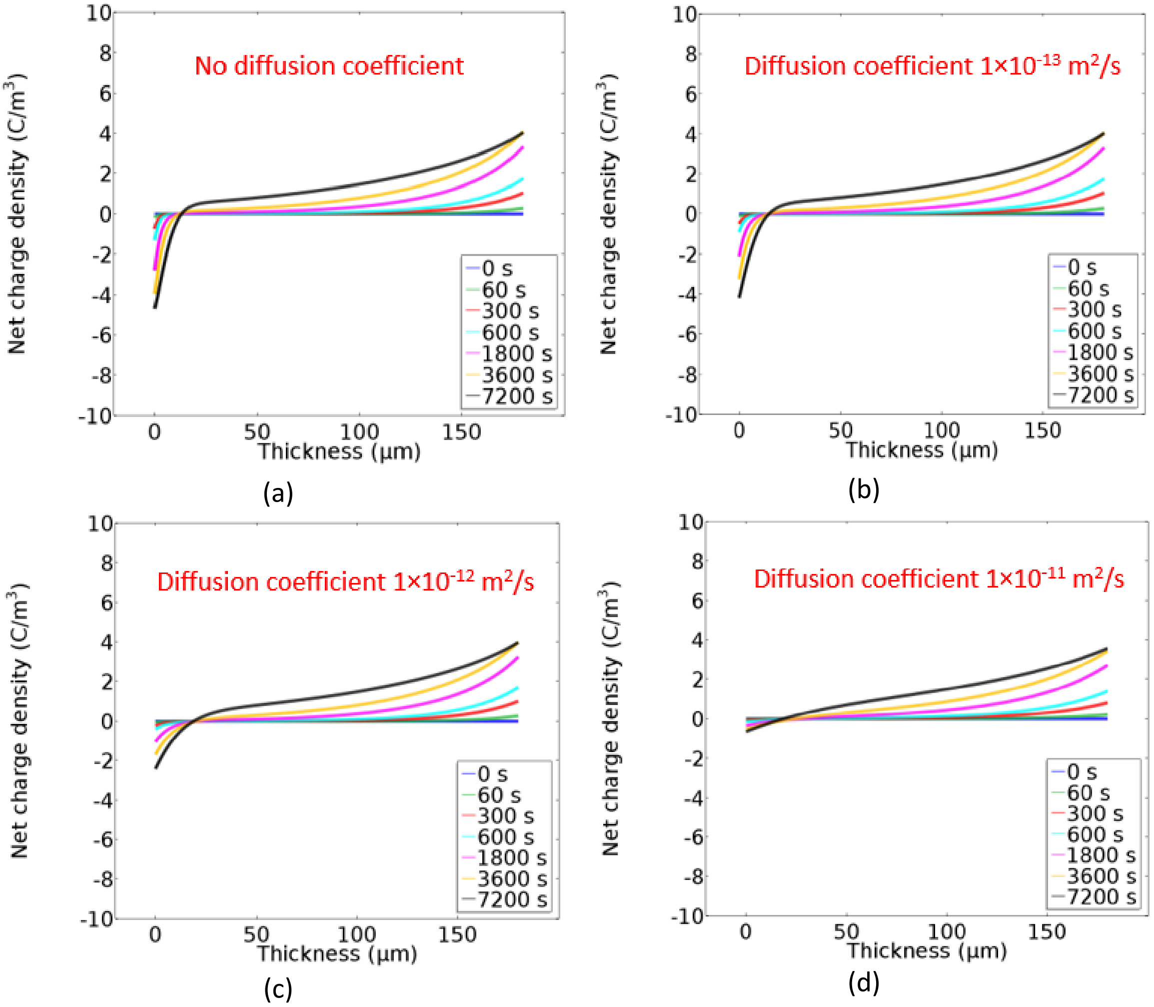

(a) (b) (c) (d)

Figure 5-12. The space charge distribution in LDPE (a) with no diffusion coefficient; (b) with a diffusion coefficient of 1×10^{-13} m^2/s; (c) with a diffusion coefficient of 1×10^{-12} m^2/s; (d) with a diffusion coefficient of 1×10^{-11} m^2/s.

By applying different values of the diffusion coefficient, the calculated space charge distributions in LDPE sample are given in the Figure 5-12. It is found that the diffusion term can lower the high concentration of charge carriers, leading to form a gentler charge concentration gradient. A lower diffusion coefficient has a limited impact on charge distribution, and a high value of diffusion coefficient, such as 1×10^{-11} m^2/s, may significantly alter the charge density where the charge carriers distribute intensively. Since the positive charge carriers distribute more uniformly, the concentration gradient of them almost remains unchanged with the increased diffusion coefficient. However, the concentration gradient of the negative charge carriers near the cathode is fairly high without considering diffusion, and it is affected greatly by the diffusion term. In consequence, the diffusion coefficient of 1×10^{-12} m^2/s is adopted in this simulation work, since it very slightly affects the overall charge distribution and it can ease the accumulation of ionic charge carriers at the boundaries.

5.3.2 Modified model by considering ionization

The space charge distributions in the fresh and degassed XLPE samples indicate that the formation of hetero charges mainly depends on ionization of impurities, like additives and crosslinking by-products. In order to simulate the space charge behaviour in XLPE by taking into account the charge carriers generated from the dissociation of impurities, some assumptions have been made and fed into bipolar charge transport model as follows. For the sake of simplification, only one type of uniformly distributed neutral ion-pairs *AB* is assumed to be the impurity within the insulation, instead of considering the various kinds of crosslinking by-products and antioxidants. The neutral ion-pairs can be thermally activated and dissociated into positive ions A^+ and negative ones B^- under the influence of electric field, as presented in the following equation:

$$AB \underset{recombination}{\overset{dissociation}{\rightleftarrows}} A^+ + B^- \tag{5-5}$$

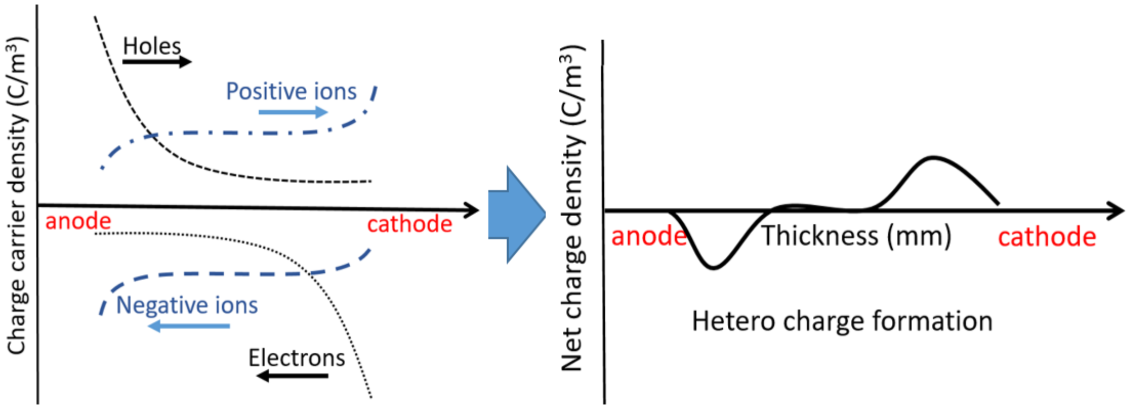

Figure 5-13. Schematic diagram of charge carrier distribution and net charge distribution modelled by the modified model by considering ionization of dissociable impurities (not to scale).

The generated positive and negative ions move towards the opposite electrode respectively under the influence of electric field and accumulate at the boundaries. Similar to the electronic charge carriers in the bipolar charge transport theory, the ionic charge carriers can also be captured by the traps and the trapped ones can be released as the mobile ones. The ions with opposite polarity can recombine together as ion-pairs. Thus in the modified model, five species are additionally considered, including neutral ion-pairs, mobile positive/negative ions and trapped positive/negative ions. The charge carrier distribution is schematically presented in Figure 5-13. The density of positive ions is always larger near the cathode, and the negative ions are concentrated in the vicinity of the anode, as the ions cannot be extracted due to their mass. Therefore, if the ionic charge carriers are distributed predominantly and offset the charge density of holes and electrons, the net charge distribution will exhibit as a hetero charge accumulation.

It has been proposed that the impurity molecule could be dissociated into ions when the thermal vibration energy overcomes the dissociation barrier [123], and the dissociation rate of the impurity is of the form:

$$D_d = v \cdot \exp\left(-\frac{w_d}{k_B T}\right) \tag{5-6}$$

where *v* is the attempt to escape frequency; w_d is the dissociation barrier at which the ion-pairs break down. However, such function does not consider the influence of electric field on the dissociation. If it is assumed that the dissociation barrier was correlated with the ionic bond strength, resembling the Poole-Frenkel mechanism [38], the dissociation barrier height can be changed in the field direction by the application of an external electric field, and thereby the dissociation rate applied in this study is expressed as:

$$D_d = v \cdot \exp\left(\frac{-w_d}{k_B T}\right) \exp\left(\frac{1}{k_B T}\sqrt{\frac{q^3 E}{\pi \varepsilon_0 \varepsilon_r}}\right) \tag{5-7}$$

The initial neutral ion-pair concentration is set to be N_0. Under the applied DC field, the generated positive and negative ions will be attracted to the opposite polarity electrode, forming the ionic conduction current. Following the assumptions made in the charge transport theory, it is also presumed that the generated positive and negative ions have the possibility to be trapped, detrapped and recombined with inverse polarity ions. Therefore, the source term for mobile negative ions $s_{n\mu}$, mobile positive ions $s_{p\mu}$, trapped negative ions s_{nt}, trapped positive ions s_{pt} can be expressed as:

$$s_{n\mu} = \frac{\partial n_{n\mu}}{\partial t} = -S_{ion1} n_{pt} n_{n\mu} - S_{ion3} n_{p\mu} n_{n\mu} - B_n n_{n\mu}\left(1 - \frac{n_{nt}}{n_{ont}}\right) + D_n n_{nt} + D_d N(x) \tag{5-8}$$

$$s_{p\mu} = \frac{\partial n_{p\mu}}{\partial t} = -S_{ion2} n_{p\mu} n_{nt} - S_{ion3} n_{p\mu} n_{n\mu} - B_p n_{p\mu}\left(1 - \frac{n_{pt}}{n_{opt}}\right) + D_p n_{pt} + D_d N(x) \tag{5-9}$$

$$s_{nt} = \frac{\partial n_{nt}}{\partial t} = -S_{ion0} n_{pt} n_{nt} - S_{ion2} n_{p\mu} n_{nt} + B_n n_{n\mu}\left(1 - \frac{n_{nt}}{n_{ont}}\right) - D_n n_{nt} \tag{5-10}$$

$$s_{pt}=\frac{\partial n_{pt}}{\partial t}=-S_{ion0}n_{pt}n_{nt}-S_{ion1}n_{pt}n_{n\mu}+B_{p}n_{p\mu}\left(1-\frac{n_{pt}}{n_{opt}}\right)-D_{p}n_{pt} \tag{5-11}$$

where B_n, D_n are the trapping and detrapping coefficients for negative ions respectively, and the recombination coefficients $S_{ion\ i}$ are of the Langevin form, function of the ionic charge carrier mobility:

$$S_{ion\ p,n}=\frac{\mu_{p,n}}{\varepsilon_0\varepsilon_r} \tag{5-12}$$

The concentration of the residual neutral ion-pairs varies with the dissociation and recombination processes, thus, the variation of the impurity density can be expressed as:

$$\Delta N(x)=\frac{\partial N(x)}{\partial t}=S_{ion0}n_{nt}n_{pt}+S_{ion1}n_{n\mu}n_{pt}+S_{ion2}n_{nt}n_{p\mu}+S_{ion3}n_{n\mu}n_{p\mu}-D_{d}N(x) \tag{5-13}$$

In this modified model, nine kinds of species are considered within the insulation bulk. In the case of positive/negative ions, it is difficult for them to be extracted at the electrodes due to the mass. Therefore, in this model, the ions are considered to be totally blocked after reaching the opposite polarity electrode. However, it should be noted that, without considering any diffusion coefficients, the accumulation of ionic charges (trapped or mobile) at the interface of electrodes/dielectric can lead to numerical errors.

Table 5-2 gives the parameters used in the modified model for simulating space charge behaviour in the XLPE samples. The initial ion-pair concentration in fresh XLPE samples is estimated from the proportion of crosslinking by-products (acetophenone 0.5-0.6 wt%) in the XLPE cable [117]. Considering the molar mass of acetophenone (120 g/mol), which has been identified to be most relevant with hetero charge formation; the density for XLPE of 920 kg/m^3; the initial concentration of neutral ion-pairs is set to be 40 mol/m^3. It has been observed that the space charge accumulation in LDPE behaves differently from that in XLPE, and the explanation could be addressed to the introduction of antioxidant and crosslinking, which increases the deep trap density and introduces deeper traps [125]. In this preliminary model, except from slightly raising the injection barrier height for holes, most parameters regarding to the holes and electrons remains unchanged, following the values given in Table 5-1, in order to evaluate if the dissociation of the impurity molecule can be accounted for the hetero charge formation in XLPE. It has to be claimed that the parameters used for simulating the ionic charge behaviour are estimated following the parameter setting of the bipolar charge transport model, and they are adjusted for fitting the space charge measurement results in the fresh XLPE samples. All the parameters except the initial ion-pair concentration are remained unchanged when simulating the space charge behaviour in fresh and degassed XLPE samples.

Table 5-2. Parameters used for simulating space charge in XLPE at room temperature.

Symbol		Value	Unit
Initial ion-pair concentration	N_0 for fresh XLPE	40	mol/m^3
	for degassed XLPE	0-4	mol/m^3
Dissociation barrier height	w_d for neutral ion-pairs	1.36	eV
Injection barrier height	w_{ei} for electrons	1.27	eV
	w_{hi} for holes	1.24	eV
Trapping coefficient	B_e for electrons	0.05	s^{-1}
	B_h for holes	0.05	s^{-1}
	B_n for negative ions	0.1	s^{-1}
	B_p for positive ions	0.1	s^{-1}
Charge carrier mobility	μ_e for electrons	2×10^{-15}	m^2/(V·s)
	μ_h for holes	1×10^{-14}	m^2/(V·s)
	μ_n for negative ions	1×10^{-16}	m^2/(V·s)
	μ_p for positive ions	2×10^{-16}	m^2/(V·s)
Detrapping barrier height	w_{tre} for electrons	0.95	eV
	w_{trh} for holes	0.95	eV
	w_{trn} for negative ions	0.99	eV
	w_{trp} for positive ions	0.99	eV
Trap density	n_{oet} for electrons	100	C/m^3
	n_{oht} for holes	100	C/m^3
	n_{ont} for negative ions	100	C/m^3
	n_{opt} for positive ions	100	C/m^3
Diffusion coefficient	For ions, holes and electrons	1×10^{-12}	m^2/s

The simulated space charge profiles in the fresh XLPE samples is given in Figure 5-14a, and it should be noted that the charge distribution is resulting from both the electronic charge carriers injected from the electrodes and the dissociated ionic charge carriers. Under the applied DC field, the neutral ion-pairs are dissociated into positive and negative ions, and the dissociated positive and negative ions move toward the opposite polarity electrode and accumulate near the electrodes, as presented in Figure 5-15a. Meanwhile, the holes and electrons are injected from both electrodes, and they migrate into the bulk toward the opposite electrode, as shown in Figure 5-15b.

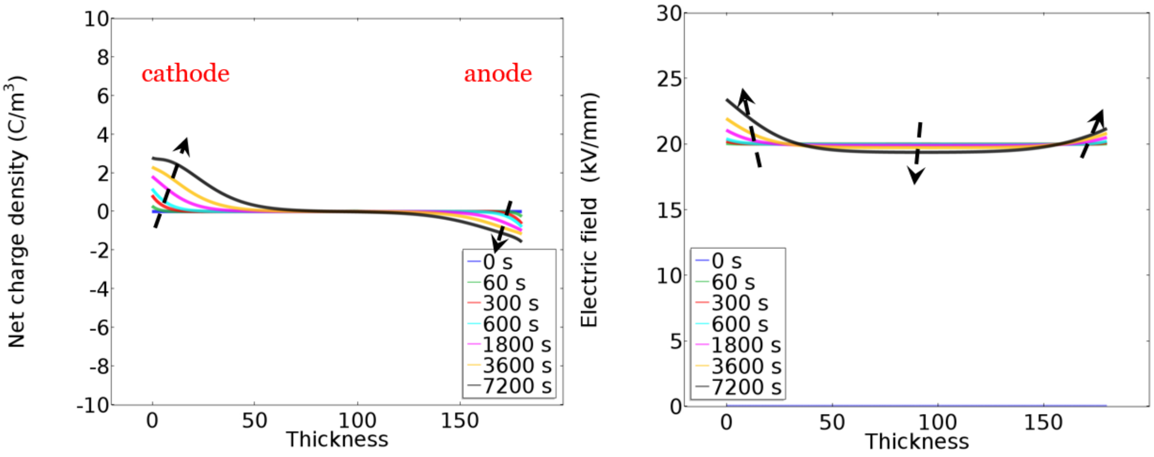

(a) (b)

Figure 5-14. (a) Simulated space charge accumulation evolving with time in fresh XLPE samples at 20 kV/mm field under room temperature. (b) Calculated electric field distribution across the fresh XLPE sample.

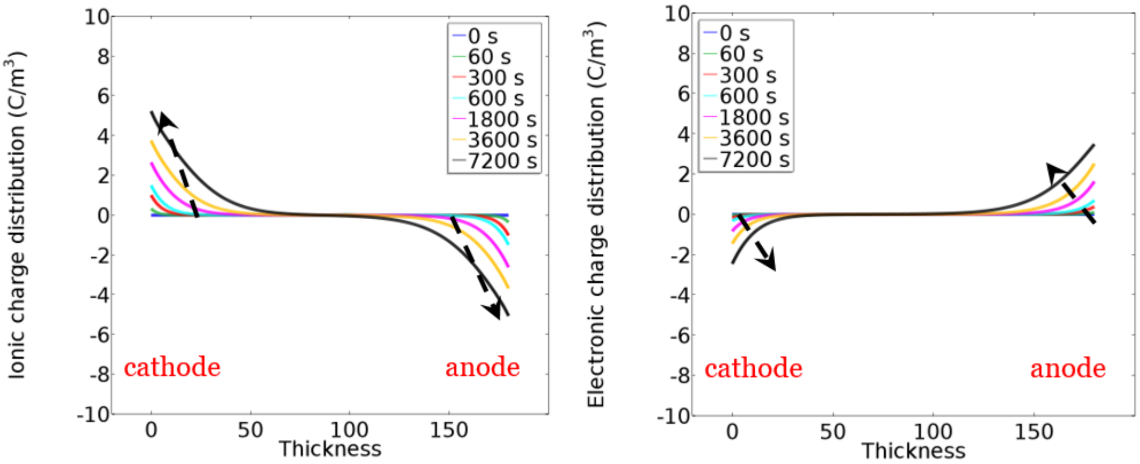

(a) (b)

Figure 5-15. (a) The calculated ionic charge distribution in the fresh XLPE samples. (b) The calculated electronic charge distribution in the fresh XLPE samples.

The sum of the ionic charge distribution and the electronic charge distribution results in the hetero charge accumulation, since much more ionic charge carriers are distributed near the electrodes. The amount of accumulated hetero charges at both electrodes increases with time gradually. Compared with the accumulation of negative charge carriers near the anode, the hetero charge formation at the cathode is more considerable, and this is due to the larger contribution of the holes injected from the electrode, which reduces the amount of negative charge carriers presented near the anode. Figure 5-14b shows the electric field distribution distorted by the presence of hetero charge accumulation. The field strength is enhanced near both electrodes but decreased in the middle part of the insulation.

The space charge distribution in the degassed XLPE samples are obtained by reducing the concentration of dissociable by-products, as shown in Figure 5-16a. Since thermal treatment can expel most volatile species such as crosslinking by-products, the initial neutral ion-pairs concentration in degassed XLPE sample is much less, and the amount of dissociated positive and negative ions is reduced significantly, as presented in Figure 5-17a. By considering the electronic charge carrier distribution as shown in Figure 5-17b, the net charge accumulation near the electrodes is reduced greatly compared with the result in the fresh XLPE samples, and such limited charge distribution leads to an almost unchanged electric field distribution, as presented in Figure 5-16b.

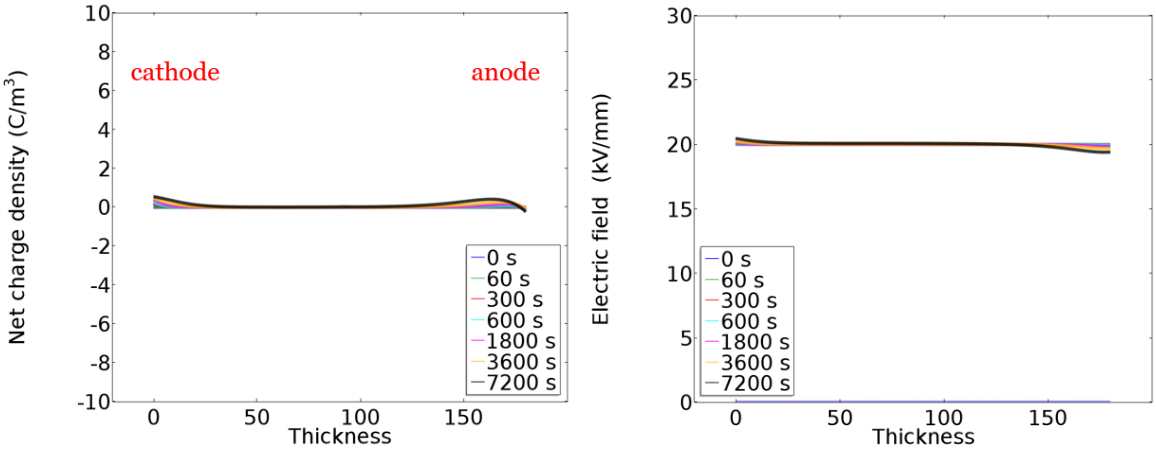

(a) (b)

Figure 5-16. (a) Space charge accumulation simulated by the modified model in degassed XLPE sample at 20 kV/mm field. (b) Electric field distribution across the degassed XLPE film.

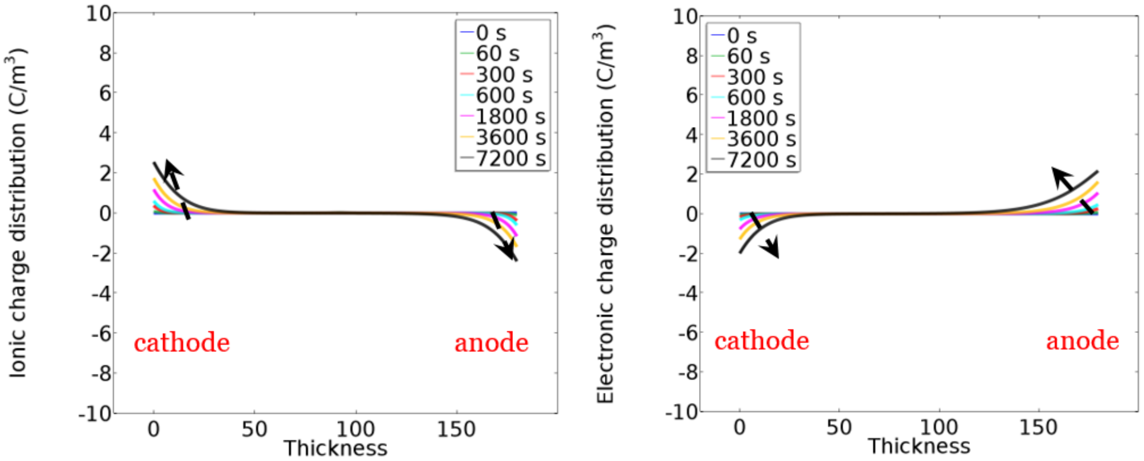

(a) (b)

Figure 5-17. (a) The calculated ionic charge distribution in the degassed XLPE samples. (b) The calculated electronic charge distribution in the degassed XLPE samples.

Consequently, the outputs from the modelling methods are comparable with the experimental observations in the additive-free LDPE samples, fresh and degassed XLPE samples. Under the application of DC voltage, the homo charge accumulation inside LDPE can be simulated by the bipolar charge transport model, and both the space charge and field distribution fit the experimental results quite well, including the charge movement and field variation evolving with time. With the modified model by considering the dissociation of impurities, the hetero charge formation at both electrodes can be simulated in the fresh XLPE samples under the DC field, and the limited charge accumulation in the degassed XLPE samples can be obtained. The location and the amount of accumulated charges within the bulk are quantitatively consistent with the experimental observations. It is found that the ionic charge behaviour interplays tightly with the electronic charge behaviour. For example, a large amount of positive ions accumulate near the cathode could lead to a high field, which enhances the injection of electrons. The injected electrons can counterbalance the hetero charges to some extent, promoting the quasi-equilibrium.

It is should be clarified that part parameters used for the modified model are estimated from the parameter setting of the bipolar charge transport model and fitting the experimental results. The range of the parameters for simulating the ionic dissociation process still need to be further validated. In general, this modified model can not only contribute to simulate dynamic charge and field distribution in XLPE, but also assist to understand the mechanisms of charge generation and transport. However, one restriction of this initial model is, only one type of impurity which can be dissociated into positive and negative ions is considered. The field-assisted thermal ionization of impurity molecules would generate positive and negative ions, protons and electrons, and If the dissociated electrons did not recombine with positive ions or holes, they would be extracted at the anode or deeply trapped in the bulk [3]. Therefore, some improvements can be achieved on this modified model, such as introducing other kinds of impurity species, considering the interactions between the ionic charge carriers and the injected charge carriers.

5.4 Summary

Under 20 kV/mm DC field, homo charge distribution has been experimentally measured in pure LDPE samples, while considerable hetero charge formation is observed in fresh XLPE samples. Only limited charge accumulation could be detected in the degassed XLPE samples, indicating the ionic charge carriers play an important role in the hetero charge formation in XLPE. By employing the bipolar charge transport model considering the electronic charge carriers, the homo charge distribution in the LDPE samples can be simulated, and it fits the measured data quite well. A modified model considering both the ionic and electronic charge behaviour is developed and applied to investigate the space charge behaviour in XLPE material. The considerable hetero charge formation in the fresh XLPE and the very limited charge accumulation in the degassed XLPE can be calculated by the new modelling approach, and the results are consistent with the experimental observations. The preliminary model is able to reproduce the hetero charge formation in XLPE by considering the combination of electronic charge and ionic charge distribution. The parameters related to the ionic charge behaviour still need to be further optimized. The types of ionic charges created by the dissociation of impurities also need to be identified.

Chapter 6 Space charge measurements and modelling in XLPE cables

The space charge behaviour in XLPE cable insulation behaves differently from that in the film insulation, as a non-uniform electric field is across the insulation thickness due to the cable geometry. In order to investigate the space charge behaviour in XLPE cables, a PEA system which is capable for measuring space charge accumulation in cable insulation, needs to be designed and built. In this chapter, the experimental setup of the cable PEA system is introduced first. Space charge measurements have been carried on the XLPE insulated cables by the cable PEA system. A modelling approach by considering both the charge injection and ionic dissociation is employed to simulate the charge accumulation within the insulation bulk subjected to a non-uniform field. Comparisons have been made between the experimental observations and the simulation results, and some discussions are given on the further study of space charge behaviour in the degassed cables and the loaded cables.

6.1 The experimental setup of cable PEA system

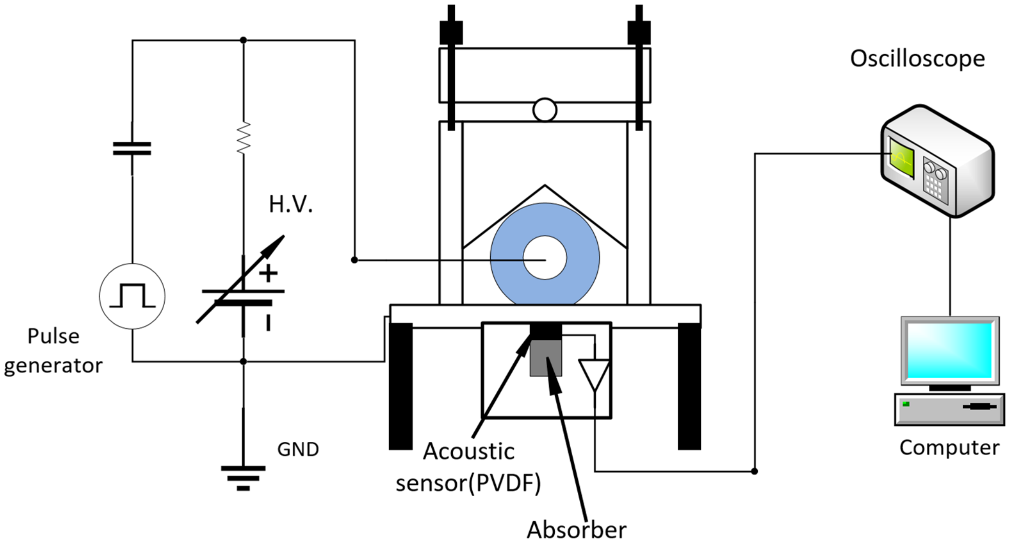

Figure 6-1. The schematic diagram of the cable PEA system.

The schematic diagram of the cable PEA system is presented in Figure 6-1. In this system, the cable sample locates on an earthed flat Al electrode, and the interface between the outer screen of the cable sample and the earthed electrode is in a line contact which is maintained intimately by giving mechanical pressure. A DC high voltage source up to 80 kV is connected to the cable core via a protecting resistor (20 kΩ) which can limit the current in the case of breakdown or flashover of the sample. Through the coupling capacitor bank (500 nF), a pulse generator can provide a HV pulse with a width of 100 ns and an amplitude up to 5 kV. The acoustic transducer (PVDF) is attached at the bottom side of the ground electrode, covered by a brass shielding box. The transducer signal is amplified by the amplifier (48 dB) and then collected by a digital oscilloscope, and the data is transferred through a general-purpose interface bus (GPIB) to a personal computer for further processing. The whole data acquisition and processing is implemented in a program developed under a graphical programming environment of Labview^{TM}.

In order to minimize the impact of the electric field generated by the high voltage pulse on the measurement, the pulse amplitude is suggested to be lower than 1/10 of the applied DC voltage. The spatial resolution of the PEA system mainly depends on the width of the pulse voltage, and a spatial resolution between 2% to 10% is preferable based on IEC standard 62758. The spatial resolution can be expressed by:

$$\eta = \frac{\Delta T_p}{d_s / v_s} \times 100\% \tag{6-1}$$

where d_s is the sample thickness (about 5 mm); ΔT_p is the pulse width; v_s is the sound velocity in polyethylene (about 2000 m/s). A high-voltage transistor switch produced from BEHLKE has been adopted to generate electric pulse signals with a width of 100 ns, providing the resolution of cable PEA system is about 5%.

6.1.1 The electrode system

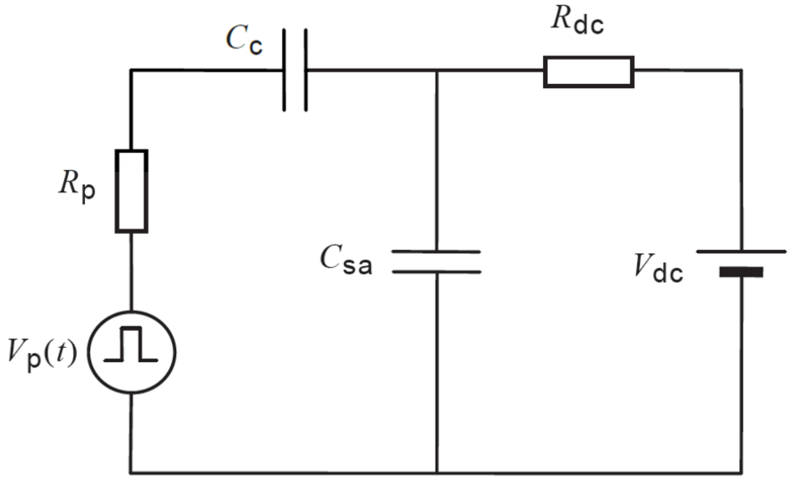

Figure 6-2. The equivalent circuit for cable PEA system.

The equivalent circuit for voltage application in cable PEA system is given in Figure 6-2, where V_p and V_{dc} are the pulse voltage and the DC voltage respectively; R_p is the internal resistance of pulse generator (50 Ω); C_{sa} is the cable sample capacitance (in the order of pF); C_c is the capacitance of the coupling capacitor; R_{dc} is the bias resistor. To apply a DC voltage to the cable insulation, the coupling capacitor C_c is necessary. If there is no coupling capacitor C_c in the circuit, the DC voltage will be separately applied to the protecting resistor R_{dc} (over 10 kΩ) and the internal resistance of pulse generator R_p (50 Ω), and consequently the voltage is not applied to R_p placed in parallel with the cable sample. Only when the coupling capacitor is connected to the circuit, the DC voltage can be adequately applied to the cable sample. In addition, the capacitance of the coupling capacitor C_c should be much bigger than the sample capacitance C_{sa}, therefore the pulse voltage can be almost applied to the cable sample. The capacitance of cable per unit length can be expressed as [110]:

$$C_{cable} = \frac{2\pi\varepsilon_0\varepsilon_r}{\ln(D_i/D_c)} \tag{6-2}$$

where D_i and D_c are the diameters of outer insulation and conductor of cable separately. Compared with the cable sample capacitance (in the order of pF), the capacitance of 500 nF is adequate for the coupling capacitor. The bias resistor R_{dc} is also needed to apply adequate pulse voltage on the capacitive cable sample. If there is no R_{dc} in the circuit, since the capacitance of cable samples C_{sa} is usually very small (in the order of pF) compared with the capacitance of power supply (in the order of mF), the pulse voltage will be almost applied on the coupling capacitor C_c (in the order of nF). Therefore, the high voltage resistor R_{dc} of 20 kΩ is applied, which can also limit the current in the case of breakdown for protecting the power supply.

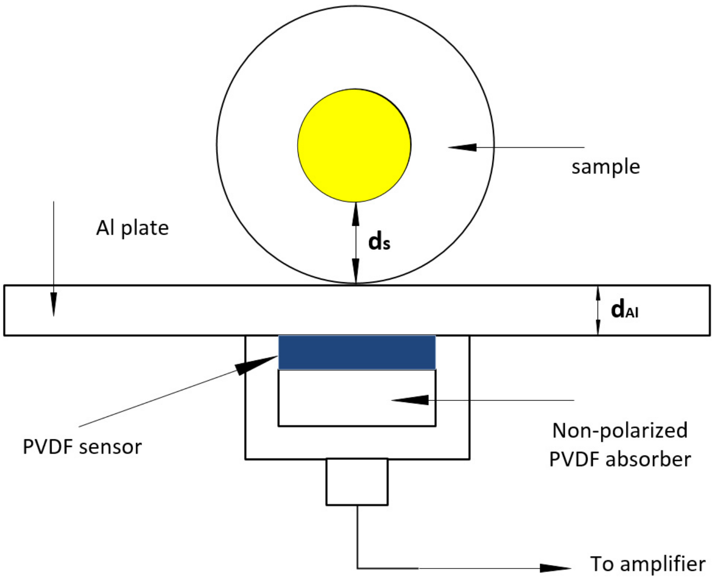

Figure 6-3. Structure diagram of the flat ground electrode.

The structure diagram of the ground electrode is shown in Figure 6-3. A rectangle transducer (PVDF) is fabricated and attached on the bottom side of the ground electrode. The PVDF sensor is supported by a cylinder, which is made of the non-polarized PVDF with the same acoustic impedance but no piezoelectric properties, serving as a backing material to reduce the acoustic reflection. Considering the acoustic reflection in the bottom electrode, the thickness of the ground electrode should match the thickness of the cable insulation. Indeed, the aluminium plate can be regarded as a delay line for acoustic wave. It takes t_1 time that the acoustic wave generated from the interface between the sample and the ground electrode goes through the Al plate and reaches the transducer, as shown in Figure 6-4.

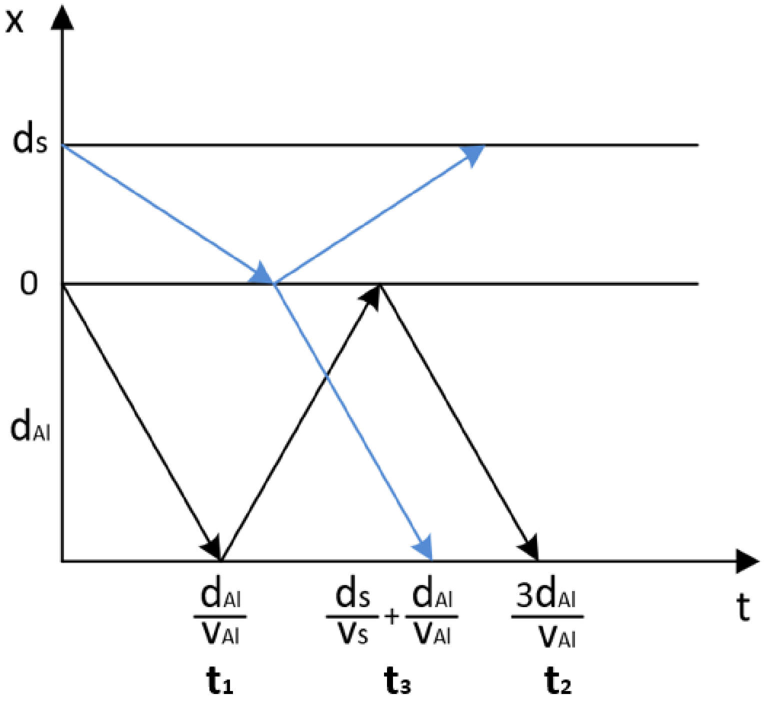

Figure 6-4. Propagation of the acoustic wave in the sample and aluminium plate.

$$t_1 = \frac{d_{Al}}{v_{Al}} \tag{6-3}$$

where d_{Al} is the thickness of the Al plate, v_{Al} is the sound velocity in aluminium (about 6000 m/s). It takes twice t_1 time when the acoustic wave reflects twice at the lower and upper surface respectively inside the Al plate. When this wave is received by the transducer again, the time is:

$$t_2 = \frac{3d_{Al}}{v_{Al}} \tag{6-4}$$

While the acoustic wave generated at the interface between the upper electrode and the sample arrives at the transducer at last, and the time it takes:

$$t_3 = \frac{d_s}{v_s} + \frac{d_{Al}}{v_{Al}} \tag{6-5}$$

where d_s is the sample thickness; v_s is the sound velocity in cross-linked polyethylene. In order to prevent the impact of wave reflections which can interfere the accuracy of the PEA test, t_2 should be bigger than t_3, so that:

$$\frac{2d_{Al}}{v_{Al}} > \frac{d_s}{v_s} \tag{6-6}$$

Therefore, if the maximum thickness of the cable insulation is 10 mm, the thickness of the ground electrode should be over 15 mm, in order to prevent the superposition of the original and reflected acoustic signals. The thickness of the ground electrode is designed as 20 mm in this system. Because of the capacitive characteristics of the PVDF transducer, it can be easily affected by other electromagnetic interferences. In this system, a shielding brass box is used to house the sensor, aiming to eliminate vibration signals from external. The experimental setup for measuring space charge in cable insulation at room temperature is given in Figure 6-5.

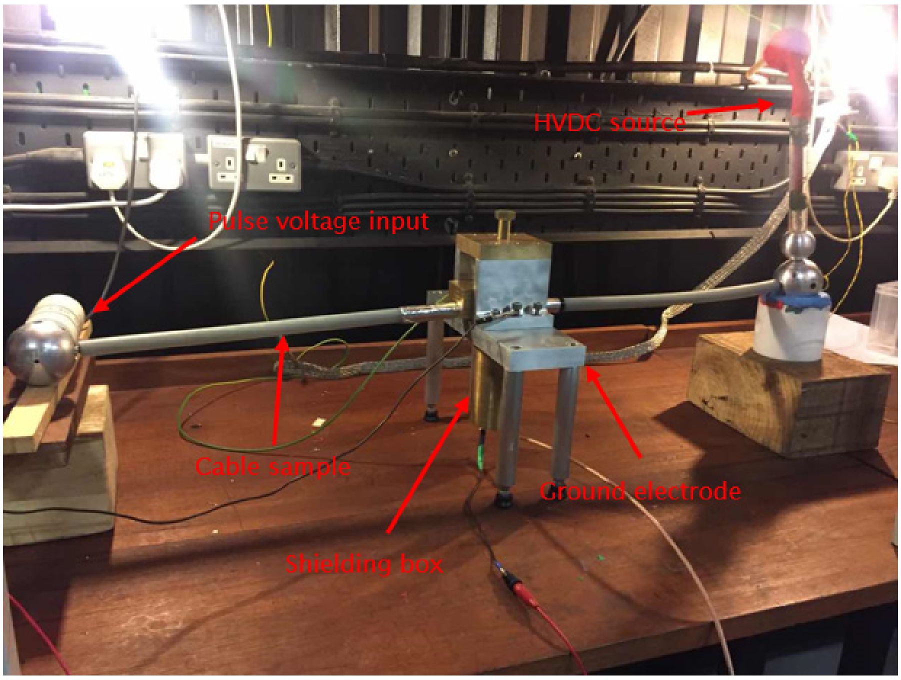

Figure 6-5. The experimental setup of the cable PEA system.

6.1.2 The temperature gradient setup

A current transformer has been installed into the cable PEA system, in order to study the space charge behaviour in cable insulation subjected to a temperature gradient. The induced current flowing in the cable core can generate heat due to Joule effect, and the outer screen of the cable is cooled by thermal convection at the room temperature, forming a radial temperature gradient across the cable insulation. Due to the limited space in the experiment cage, the current transformer has to be lay on the floor. An XLPE cable covered by grounded metallic screen is used to pass through the hollow core of current transformer, and both ends of the cable are connected to the measured cable sample, as shown in Figure 6-6.

A small hole was drilled on the test cable sample, allowing the thermal couple could be inserted into the insulation and attached to the cable conductor. Another thermal couple was attached to the outer surface of the cable insulation, and both thermal couples were connected to two thermometers separately. By inducing a current of 200 A, a stable temperature gradient of about 10°C can be reached after 2-hour heating, as presented in Table 6-1.

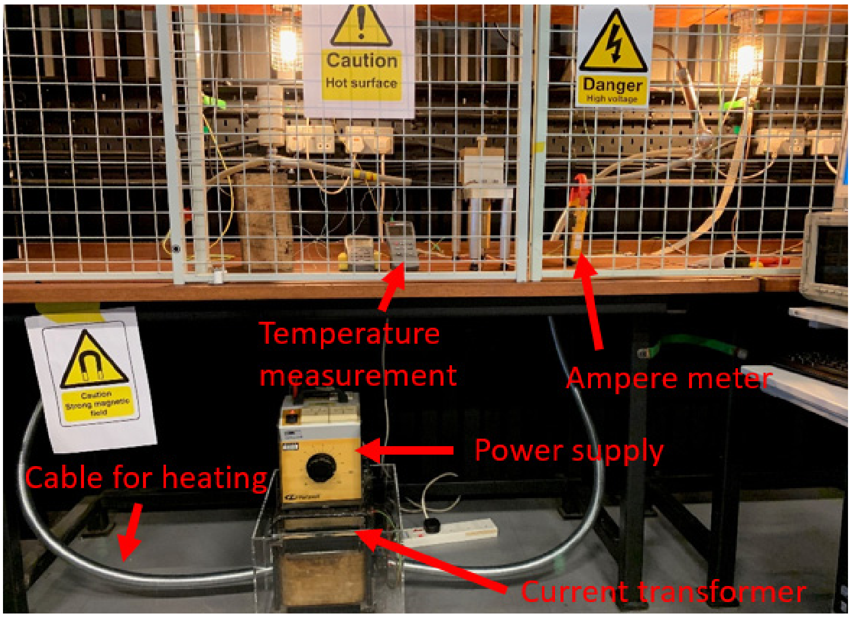

Figure 6-6. Test of thermal gradient across the XLPE cable

Table 6-1. The temperature gradient across the insulation using a 200 A induced current.

Time (h)	Ambient temperature (°C)	Inner temperature (°C)	Outer temperature (°C)	Temperature gradient (°C)
0	18.2	18.0	17.9	0.1
1	18.4	46.2	35.4	10.8
2	18.6	48.3	38.0	10.3
3	18.3	48.5	38.4	10.1
4	18.4	48.6	38.5	10.1
5	18.1	48.8	38.2	10.6

However, the space charge measurement has not been carried on the cables subjected to a temperature gradient. The reason is that the discharge may take place at the joints of the cables when the applied voltage exceeds 40 kV in the experiment cage. The aluminium ball electrodes covered by insulation clay are used to applied high DC voltage (up to 80 kV) on the cable conductor at room temperature. However, to connect the cable for induced current heating, the cable joints have to be installed to connect the two cables and the electrical components, as shown in Figure 6-7. The discharge still occurs even with the joint surface polished by the conductive paste. Generally, the cable connection needs to be further improved to achieve the space charge measurement in safety, and it is also suggested to move the cable PEA system into a larger experiment cage with a longer distance between the ground and the high voltage potential.

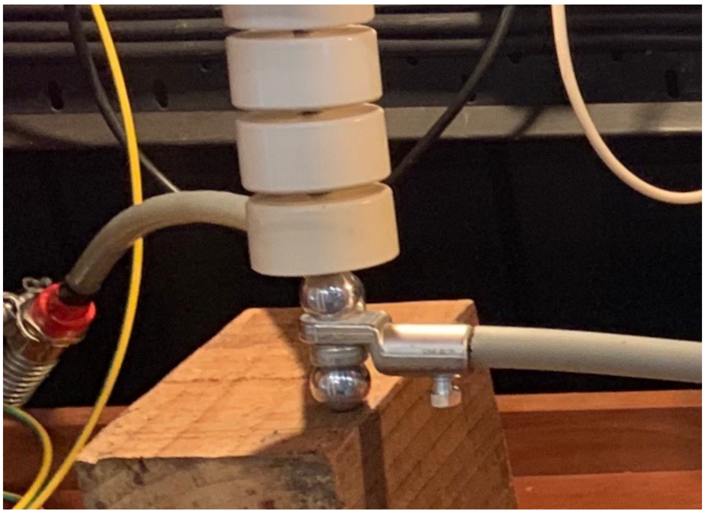

Figure 6-7. The joint for cable connection.

6.2 Space charge measurements in XLPE model cables

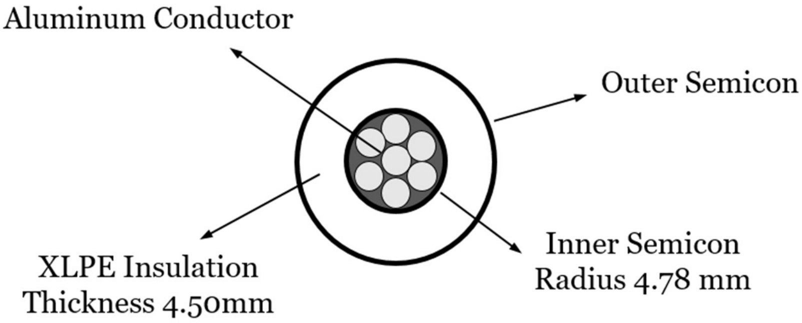

Figure 6-8. The cross-section view of the XLPE model cable.

The insulation system of the XLPE model cable is produced from HV super clean cable-grade low density polyethylene (LDPE) and 2 wt% DCP has been added, serving as the crosslinking agent. An insulation thickness of 4.5 mm was manufactured on a Troester triple extrusion line, as shown in Figure 6-8. The area of 7-stranded aluminum conductor is about 50 mm^2. Two kinds of samples, the original cable and the degassed cable samples, are prepared for measurements, in order to observe the impacts of degassing on material performance.

6.2.1 Cable samples preparation

For space charge measurements, the XLPE model cable was cut into a length of 1.3 m. At the ends of the cable samples, the insulation and the semicon screens were removed, leaving only conductor with a length of 5 cm. The outer semicon screen was stripped away from the two ends, only leaving a length of 15 cm at the middle of the sample. In order to reduce the distributed capacitance at the gap between the curved cable and the flat ground electrode, the remaining outer semicon layer was covered with wrapped aluminium foil carefully. The prepared model cable sample for space charge measurement is shown in Figure 6-9. Indeed, degassing is an essential procedure adopted by cable manufacturers, to remove volatile residual by-products at a moderately high temperature [117]. In this study, the cut model cable samples were placed in a vacuum oven at a constant temperature of 80℃ for 7 days. After cooling down to the room temperature, measurements were taken on the degassed samples directly.

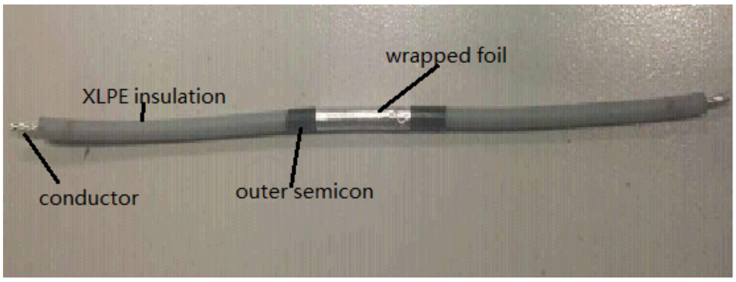

Figure 6-9. Prepared model-cable sample for space charge measurement.

6.2.2 Space charge profile in XLPE cables at room temperature

The space charge behaviour in original cable samples evolving with time is presented in Figure 6-10. It has to be clarified that a negative radius axis is adopted here for indicating left to the outer semicon layer, right to the cable core, and for sake of visual comparison, the simulated results are also plotted in the same way. After the application of DC voltage of +80 kV at the cable conductor, it is clear to observe that the hetero charge formation near the cathode. The amount of positive charge carriers increases with time, while the accumulation of negative charge carriers near the anode is inconspicuous. The net charge distribution presenting within the cable insulation can be obtained by removing the capacitive charges at the electrodes via the subtraction process mentioned in section 5.2.2, and the considerable hetero charge formation inside the cable insulation results in a high electric field near the cathode, as presented in Figure 6-11.

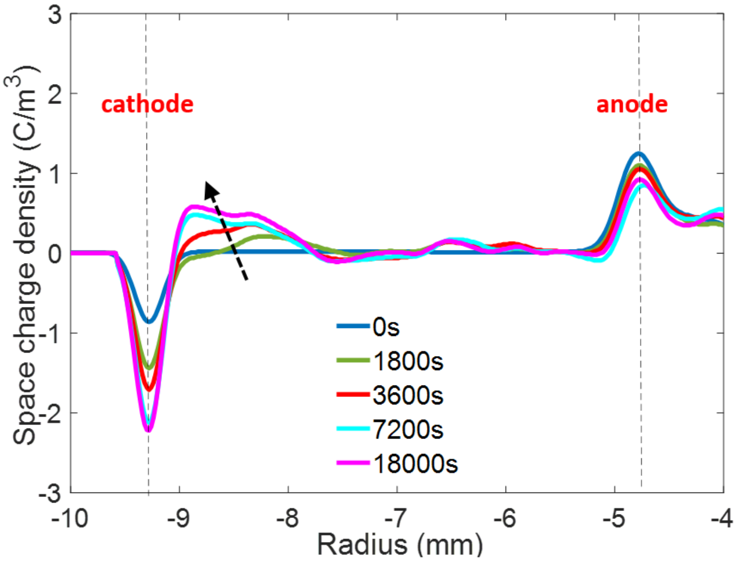

Figure 6-10. The space charge profile of the undegassed XLPE cable sample under 80 kV at the room temperature (25°C).

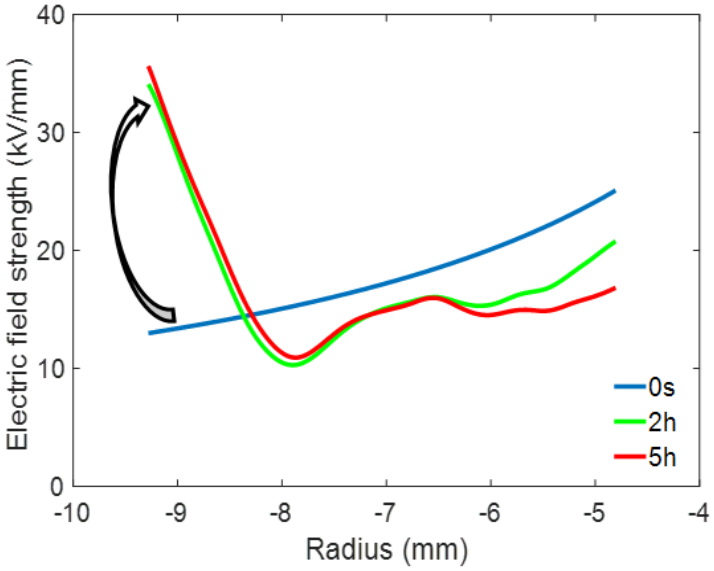

Figure 6-11. The electric field distribution across the original cable insulation at the room temperature.

When no space charge presents over the insulation thickness, the initial transient electric field distribution is a capacitive distribution, which is mainly dependent on the permittivity of insulation, and the inner insulation withstands the highest electric stress. However, in DC cables the long-term field distribution is not only governed by the field and temperature dependent conductivity, but also determined by the build-up of space charge. Due to the presence of large amount of hetero charges, the electric field near the cathode is enhanced greatly, which might also promote the charge injection at the interface and the dissociation of impurities. The space charge characteristics of the XLPE model cable under the DC field are also confirmed by the space charge decay results, as shown in Figure 6-12. A large amount of positive hetero charges is observed near the cathode, and the decay of these hetero charges is extremely slow. There is no obvious charge accumulation near the anode. The accumulated positive charges within the bulk induce negative charges on the electrodes. After 24 hours of the voltage removal, the hetero charges can still be detected near the cathode.

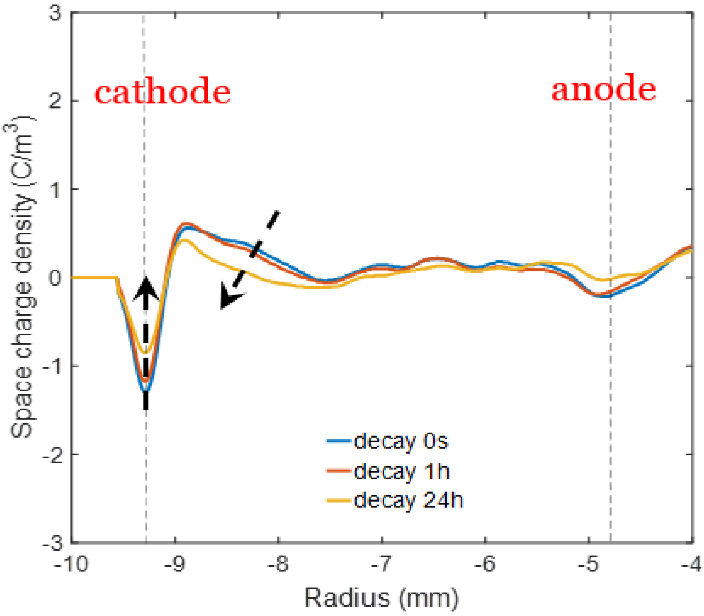

Figure 6-12. The space charge decay results of the undegassed XLPE cable sample.

Figure 6-13 presents the space charge profiles in the degassed cable samples under the same voltage, compared with the results in the original samples, the hetero charge accumulation reduces apparently, since most volatile crosslinking by-products have been removed from the bulk. The limited hetero charge formation in the degassed cable samples indicates there are still residual crosslinking by-products after the thermal treatment. Until t=18000 s, limited positive charges can only be detected near the cathode, and there is still no apparent charge accumulation at the anode. Due to the insufficient charge accumulation, the electric field is only lightly distorted, as shown in Figure 6-14.

The experimental observations from the PEA technique only indicate the net charge density, and it cannot characterize the charge species. For original XLPE cable samples, it is considered that the hetero charge formation is primarily owing to the ionization of dissociable impurities, and similar profiles are measured in an XLPE cable at a mean electric field of 20 kV/mm [71]. It should be noted that positive charges accumulate notably near the cathode, while the accumulation of negative charges is limited. This phenomenon may be as a result of a larger amount of injected charges from the anode due to the relatively high electric field at the inner cable insulation, which offsets the negative charge accumulation. It can also be argued that the generated ionic charges may behave differently in migration in electric field depending on their polarity.

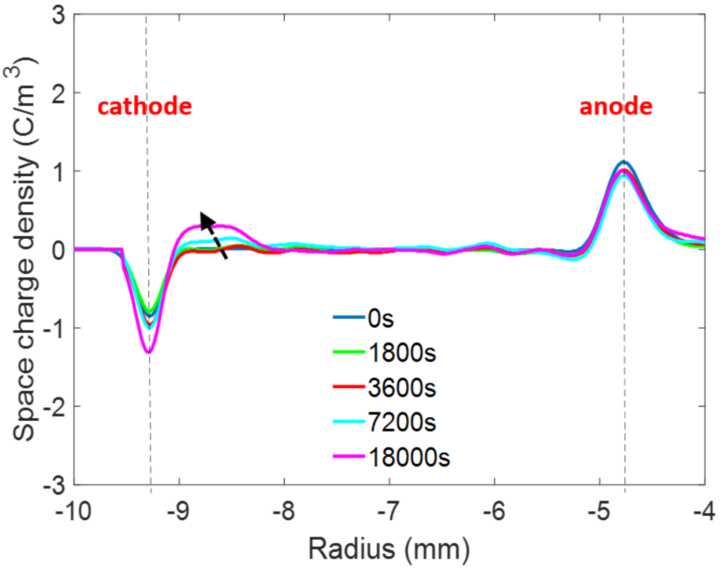

Figure 6-13. The space charge profile of the degassed cable sample under 80 kV at the room temperature (25°C).

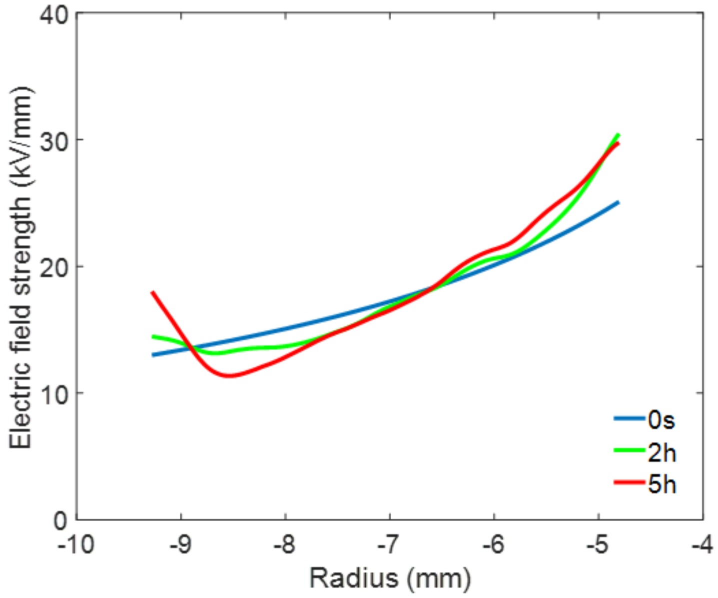

Figure 6-14. The electric field distribution within the degassed cable insulation bulk at the room temperature.

6.3 Space charge modelling in XLPE insulated cables

The modelling approach following the work in section 5.3.2 where the formation and transport of ionic charge carriers have been considered and fed into the bipolar charge transport model. Since the model has been successfully employed to simulate and analyse the space charge behaviour in

XLPE flat specimens, by considering both the charge injection and ionic dissociation, the model is employed to simulate the space charge and field distribution within the cable insulation bulk subjected to a non-uniform field. The model is implemented by using COMSOL Multiphysics. The “Transport of Diluted Species”, the “Heat Transfer in Solids” and the “Electrostatics” modules have been applied to simulate the charge dynamics migrating in electric field. The thickness of the sample is divided into 450 divisions equally.

6.3.1 Model descriptions

The model used in the plane geometry has been described in detail in section 5.3, here, three space and time dependent equations describing the charge behaviour in a cable geometry are presented as follows:

$$\frac{\partial^2 V(r,t)}{\partial r^2}+\frac{1}{r}\frac{\partial V(r,t)}{\partial r}=-\frac{\rho(r,t)}{\varepsilon_0\varepsilon_r} \tag{6-7}$$

$$\frac{\partial n_a(r,t)}{\partial t}+\frac{1}{r}\frac{\partial(j_a\cdot r)}{\partial r}=s_a(r,t) \tag{6-8}$$

$$j_a(r,t)=\mu_a(r,t)n_{a\mu}(r,t)E(r,t)-D_f\frac{\partial n_a(r,t)}{\partial r} \tag{6-9}$$

where V is the electric potential; ρ is the net charge density; j_a is the conduction current density, and a refers to the type of charge; D_f is the diffusion coefficient; s is the source term, which encompasses changes in local density due to processes other than transport, such as internal ionic charge generation, recombination, trapping and de-trapping of charge carriers. Nine species are considered in this model, and they are mobile/trapped electrons, mobile/trapped holes, mobile/trapped negative ions, mobile/trapped positive ions and the neutral ion-pairs. The electronic charge carriers are considered from the charge injection. A threshold electric field is introduced to define the boundary conditions, when the local field at the electrodes exceeds 10 kV/mm, the injected current density is determined by the Schottky injection law, otherwise the current form follows the conduction of Ohmic type, as described in section 3.3.2. It is also assumed that the ionic charge carriers can be generated from the dissociation of an impurity molecule *AB*, and the dissociation rate considering the influence of electric field is applied, which has been described in section 5.3.2. The charge conduction has been described by a constant effective mobility under the uniform field at room temperature. Considering the non-uniform electric field and the thermal effects, the charge transport within the polymeric insulation is described by a hopping mechanism in which charge carriers migrate from site to site by overcoming a potential barrier, and the mobility for mobile charge carriers (electrons, holes, negative and positive ions) can be expressed as:

$$\mu_{e,h}(r,t)=\frac{2d_e v}{E(r,t)}\exp\left(\frac{-ew_{\mu e,\mu h}}{k_B T(r)}\right)\sinh\left(\frac{eE(r,t)d_e}{2k_B T(r)}\right) \tag{6-10}$$

$$\mu_{n,p}(r,t)=\frac{2d_i v}{E(r,t)}\exp\left(\frac{-ew_{\mu n,\mu p}}{k_B T(r)}\right)\sinh\left(\frac{eE(r,t)d_i}{2k_B T(r)}\right) \tag{6-11}$$

where d_e and d_i are the hopping distances for electronic and ionic charges respectively; $w_{\mu e}$, $w_{\mu h}$, $w_{\mu n}$ and $w_{\mu p}$ are the hopping barrier heights for electrons, holes, negative and positive ions separately. In the present simulation, it is presumed that the impurity molecule *AB* is distributed uniformly along the cable radial direction. It should be noted that no extraction barrier is considered at the electrodes, and the extraction fluxes for holes at the cathode and for electrons at the anode follow the transport equation, as it is considered that the ionic charges are the main contributors to hetero charge formation.

6.3.2 Simulation of space charge profiles in XLPE insulated cables at room temperature

Both the electrical and thermal conditions are set to be same with the experiments, and the parameters used for modelling space charge behaviour in the XLPE insulated cable are listed in Table 6-2. The parameters are almost same with the ones used to simulate space charge accumulation in flat XLPE specimens in section 5.3.2. However, it should be noted that the fabrication process of the XLPE flat specimens in the laboratory is different from that of the XLPE cable insulation in the factory, thus the XLPE material properties may be different from each other. In this simulation, we still apply the parameters used for the XLPE flat specimens to investigate the space charge behaviour in XLPE insulated cable, assuming the insulation material had the same electrical performance. The hopping barrier heights for different charge carriers are considered to describe the charge mobility. The hopping barrier heights for electrons and holes follow the ones used in bipolar charge transport model, and it is assumed that the ionic charges have a lower mobility with higher hopping barrier heights. It has to be clarified that the space charge profiles are contributed from the combination of injected electronic charges and the dissociated ionic charges.

Table 6-2. Parameters used for modelling space charge in the XLPE cable.

Parameter		Value	Unit
Injection barrier height	w_{ei} for electrons	1.27	eV
	w_{hi} for holes	1.24	eV

Initial ion-pair concentration	N_0 for fresh XLPE	40	mol/m^3
	for degassed XLPE	0-4	mol/m^3
Dissociation barrier height	w_d for neutral ion-pairs	1.36	eV
Trapping coefficient	B_e for electrons	0.05	s^{-1}
	B_h for holes	0.05	s^{-1}
	B_n for negative ions	0.1	s^{-1}
	B_p for positive ions	0.1	s^{-1}
Detrapping barrier height	w_{tre} for electrons	0.95	eV
	w_{trh} for holes	0.95	eV
	w_{trn} for negative ions	0.99	eV
	w_{trp} for positive ions	0.99	eV
Hopping barrier height (for mobility)	$w_{\mu e}$ for electrons	0.71	eV
	$w_{\mu h}$ for holes	0.65	eV
	$w_{\mu n}$ for negative ions	0.77	eV
	$w_{\mu p}$ for positive ions	0.75	eV
Trap density	n_{oet} for electrons	100	C/m^3
	n_{oht} for holes	100	C/m^3
	n_{ont} for negative ions	100	C/m^3
	n_{opt} for positive ions	100	C/m^3
Diffusion coefficient	For ions, holes and electrons	1×10^{-12}	m^2/s

The calculated net charge distribution within the cable insulation is presented in Figure 6-15. The amount of positive charges at the cathode increases gradually with time, and very limited hetero charge accumulation can be formed near the anode. Such charge profiles result from the combination of the ionic charge and the electronic charge distribution as presented in Figures 6-16a and 6-16b respectively. Shortly after the application of DC voltage, the impurity molecules *AB* are dissociated into positive and negative ions under the influence of field. The positive ions A^+ move towards the cathode and the negative ones B^- migrate oppositely, leading to a hetero charge formation at the electrodes. Meanwhile, the holes and the electrons are injected from the electrodes respectively, and they are enforced to penetrate towards the opposite electrode by the electric field, building up a homo charge accumulation. With the assumptions of a lower injection barrier height and a higher mobility for holes, the amount of holes presenting inside the bulk is much larger than electrons. Therefore, as a sum of the ionic and electronic charge carriers, the net charge distribution shows a hetero charge formation consequently, which deforms the electric field distribution by enhancing the field strength greatly at the cathode, as shown in Figure 6-17.

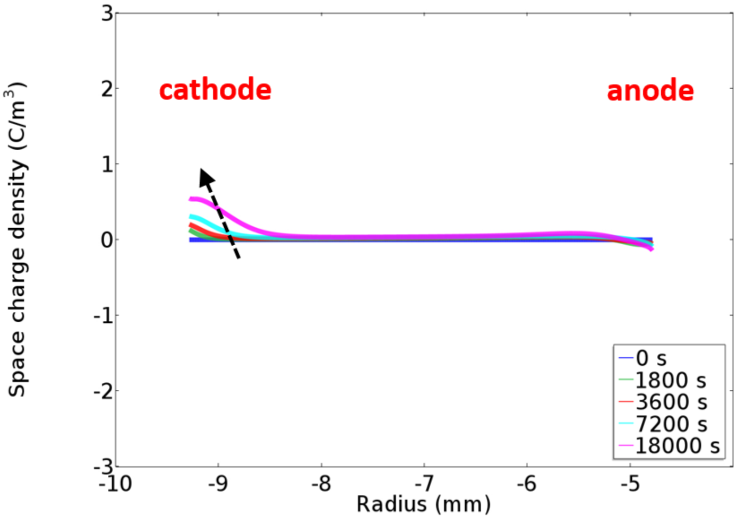

Figure 6-15. The calculated net charge distribution in the original XLPE cable.

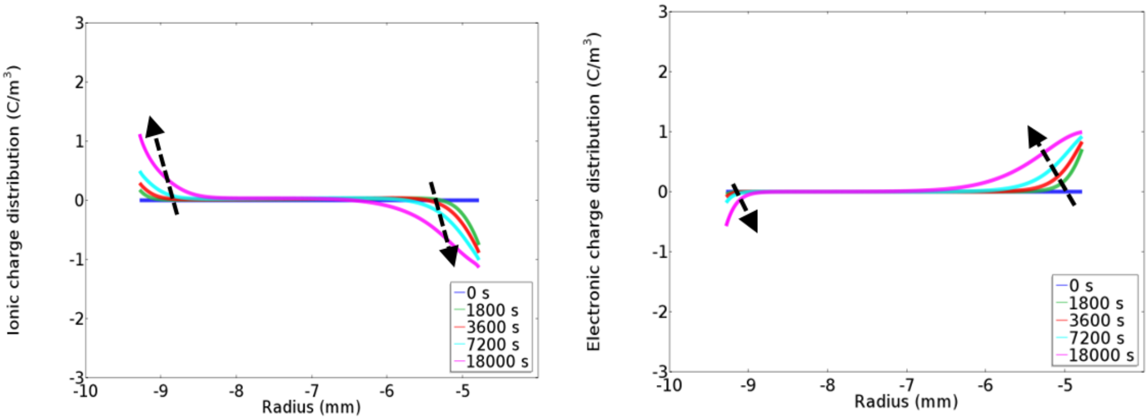

(a) (b)

Figure 6-16. (a) The ionic charge distribution over the undegassed cable insulation thickness; (b) The electronic charge distribution over the undegassed cable insulation thickness.

The net charge distribution in the degassed cable samples is calculated by lowering the concentration of impurity, as presented in Figure 6-18. Since the degassing process removes most volatile crosslinking by-products, fewer impurity molecules *AB* are left to be dissociated into ions under the field, leading to a much less ionic charge carrier accumulation, as presented in Figure 6-19a. By considering the injected charge carriers shown in Figure 6-19b, very limited charge accumulation can be observed inside the bulk compared with the result in the original cable sample. A small amount of positive charges accumulates near the anode, which slightly deforms the electric field distribution over the cable insulation thickness, as shown in Figure 6-20.

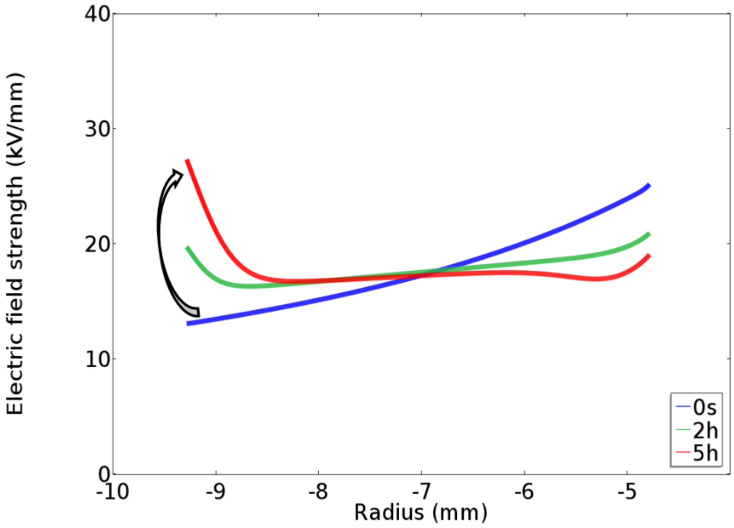

Figure 6-17. The calculated electric distribution over the undegassed cable insulation thickness.

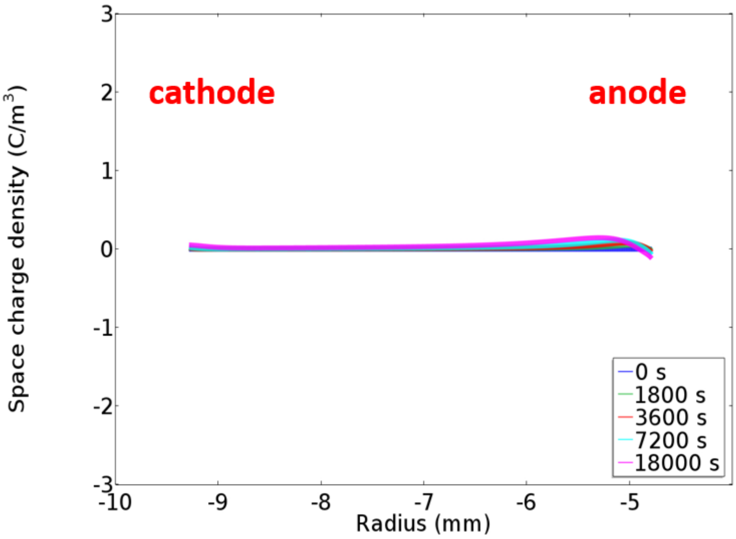

Figure 6-18. The calculated net charge distribution in the degassed XLPE insulated cable.

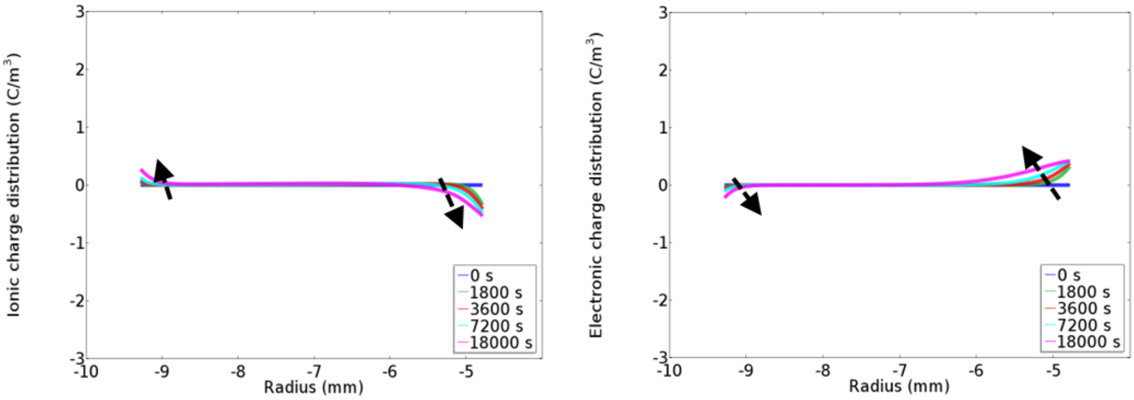

(a)

(b)

Figure 6-19. (a) The ionic charge distribution over the degassed cable insulation thickness; (b) The electronic charge distribution over the degassed cable insulation thickness.

Compared with the experimental observations, the calculated space charge profiles can reproduce the considerable hetero charge formation in original XLPE cable samples and the local field reinforcement near the cathode. The simulated net charge density near the cathode at last is increased to about 0.5 C/m^3, fitting the measured data well, but the calculated final field strength at the cathode is about 28 kV/mm, which is gently underestimated compared with the experimental results. It seems that both the net charge distribution and field variation tendency are generally consistent with the experimental observations in the original cable samples. However, in the degassed samples, although the limited charge accumulation and the slightly distorted field can be calculated by the modelling method, the simulated charge and field distribution cannot quantitatively correspond the measured data. The hetero charges can hardly be found near the cathode, and the lowered field strength at the anode is different from the measured results. Such differences could be resulted from the assumption of a uniformly fixed initial impurity concentration level in the degassed cable samples.

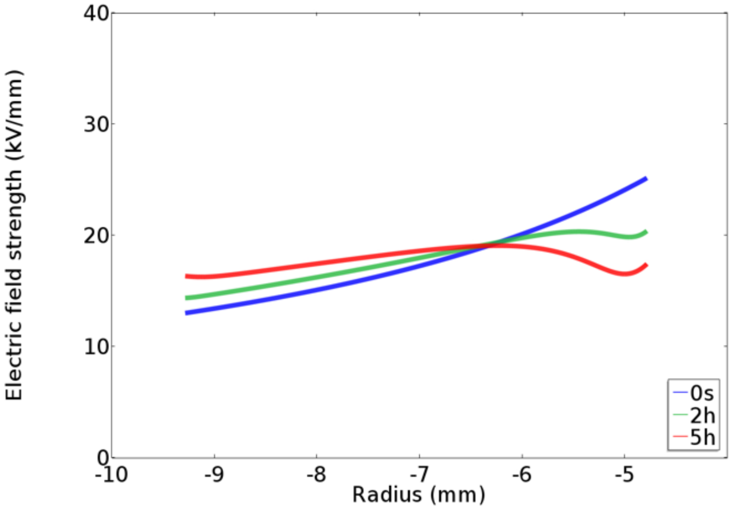

Figure 6-20. The calculated field distribution in the degassed XLPE insulated cable.

In this study, in both the undegassed and degassed samples, the impurity is considered to distribute uniformly across the cable radial thickness, but it has been reported in many literatures that there could be an impurity concentration gradient along the cable radius, which could greatly affect the ionic charge generation and transport in the cable geometry. Indeed, during the degassing process, the crosslinking by-products diffuse with different rates and their distribution might be inhomogeneous across the insulation thickness. After measuring the content of crosslinking byproducts in sliced cable samples, Ren et al. considered the inner cable insulation retains higher level of by-products, and the concentration decreases from inner to the outer part [126]. Smedberg et al. proposed that the by-products diffuse from the middle part to the inner and the outer semicon layer, therefore the middle insulation shall contain the highest level of impurities [127]. In literature [128], it was also suggested that the interdiffusion of residues between the semicon layer and the insulation material results in a higher concentration of impurities at the inner and the outer part. It seems that the impurity concentration is mainly determined by the diffusion of by-products during the degassing process, and the initial impurity gradient across the cable insulation should be taken into account in future study by measuring the concentration of crosslinking by-products in different regions of cable insulation.

By assuming the impurity concentration level is higher at the inner insulation and lower at the outer part, a simple linear function along the radius is applied as the initial impurity concentration distribution in the degassed cable samples, as presented in Figure 6-21. And the calculated space charge and field distribution based on such initial impurity concentration distribution are shown in Figures 6-22 and 6-23 separately.

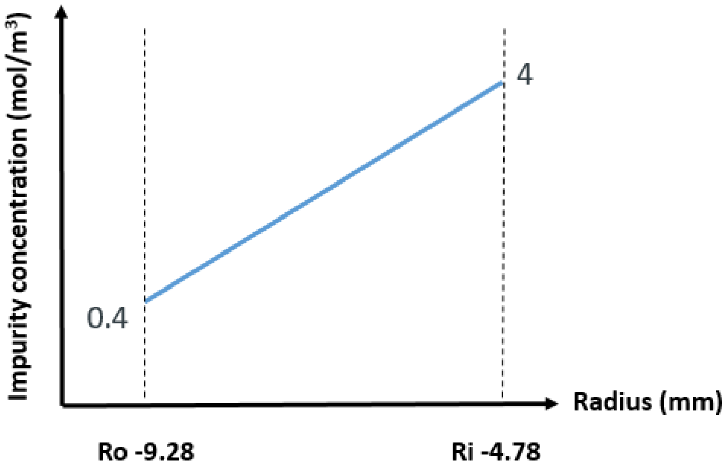

Figure 6-21. The presumed initial impurity concentration distribution in the degassed cable sample.

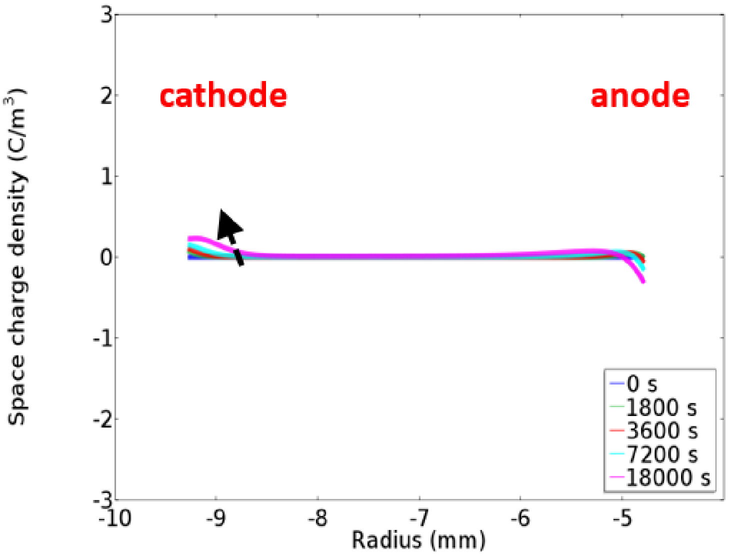

Figure 6-22. The calculated net charge distribution in the degassed cable sample with an impurity concentration gradient.

With a higher concentration of impurity molecules at the inner insulation, both the calculated space charge and field distribution seem to be more comparable with the experimental results in the degassed cable samples. More ionic charge carriers can be generated near the anode due to the higher concentration of neutral ion-pairs, therefore the amount of negative ions presenting near the anode is larger. The accumulation of ionic charge carriers near the electrodes offsets the electronic charge carrier distribution in the vicinity of the electrodes, and limited hetero charge accumulation can be observed within the insulation bulk. It can be argued that the calculated results of an initial concentration gradient are more consistent with the experimental observations in the degassed cable sample, which indicates the impurities are distributed intensively at the inner part after the degassing process.

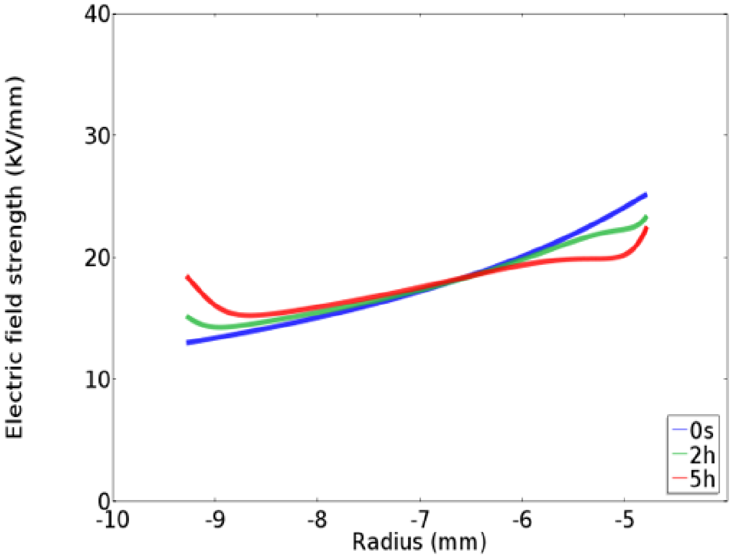

Figure 6-23. The calculated electric field distribution in the degassed cable sample with an impurity concentration gradient.

6.3.3 Simulation of space charge profiles in XLPE insulated cables with a temperature gradient

Space charge accumulation is highly dependent on temperature in polyethylene-based materials, and It is also reported that the increased temperature can enhance the ionic dissociation of cross-linking by-products and accelerate the hetero charge formation [106] [129]. Space charge measurements have been carried on the XLPE cables in the presence of temperature gradients, and the results revealed that the hetero charges always accumulate near the low temperature side, and the charge amount increases with a larger temperature gradient [27] [130]. Based on the assumptions of temperature-dependent charge generation and transport of both ionic and electronic charge carriers, the space charge behaviour in the XLPE model cable subjected to a temperature gradient is simulated by the proposed model. The impurity molecules are assumed to be distributed uniformly across the cable insulation. The inner temperature is set to be 50℃, and the outer is set to be 40℃, forming a temperature gradient of 10℃ across the cable insulation, which can be expressed as:

$$T(r)=T(r_o)+\frac{\ln\left(\frac{r_o}{r}\right)\left(T(r_i)-T(r_o)\right)}{\ln\left(\frac{r_o}{r_i}\right)} \tag{6-12}$$

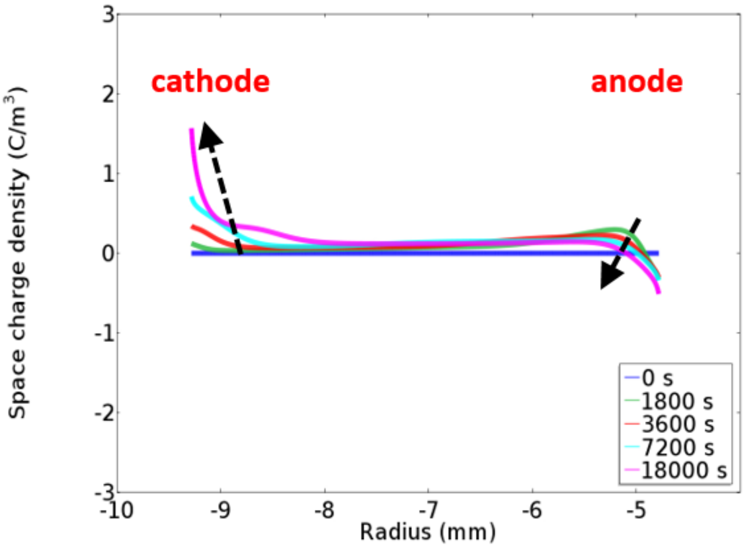

Figure 6-24. The calculated net charge distribution in the degassed XLPE insulated cable with the presence of a temperature gradient (50-40℃).

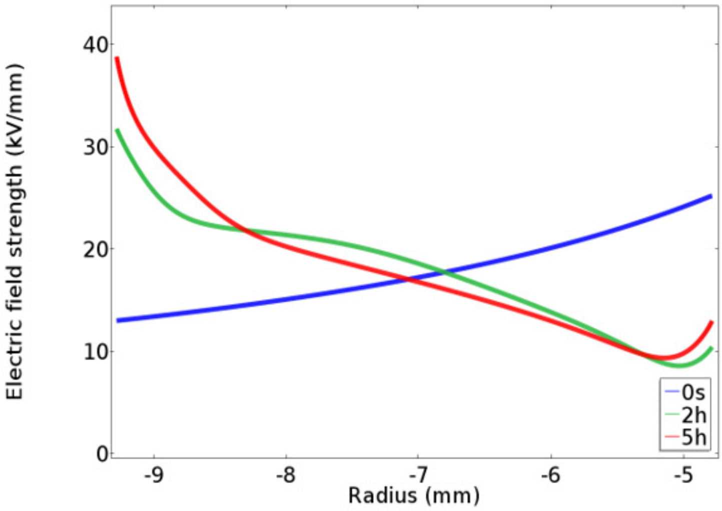

Figure 6-25. The calculated field distribution in the degassed XLPE insulated cable with the presence of a temperature gradient (50-40℃).

Figure 6-24 shows the simulated net charge distribution in degassed XLPE cable insulation subjected to a 10℃ temperature gradient. The considerable hetero charge formation can be calculated by the model. Due to the temperature gradient across the cable insulation, both the ionic dissociation and electronic injection have been enhanced significantly, and the charge transport has also been accelerated. The accumulated positive charge carriers near the cathode are mainly from the dissociated positive ions, which reinforce the electric field significantly near the cathode, as presented in Figure 6-25. A small amount of positive charge carriers is observed in the vicinity of the anode, which decreases gradually with time. This is because the trapped holes near the anode are offset gradually by the dissociated negative ions.

However, it should be noted that the model still needs to be further improved to simulate the space charge behaviour in the loaded cables. The impurity diffusion need to be considered under the high temperature, and the parameters related to ionic charge behaviour still need to be further optimized via space charge measurements and conduction current measurements under various thermal conditions. Consequently, the modelling approach is able to be potentially applied to calculate the dynamic charge and field distribution in XLPE cable insulation subjected to both electrical and thermal stresses.

6.4 Summary

A cable PEA system has been designed and built, and the space charge measurements have been carried on the XLPE model cables at the room temperature. The noticeable hetero charge accumulation is observed in original XLPE insulated cables under 80 kV, and limited hetero charges could be still detected in the degassed cable samples. Space charge behaviour in XLPE cable insulation is investigated by the modelling method which considers both the electronic and ionic charge generation and transport. Compared with the experimental observations, both the hetero charge formation and the field enhancement near the cathode can be calculated and the results show good consistency in the original cable samples. The limited charge accumulation and slightly deformed field can be calculated in the degassed cable samples. However, it seems necessary to introduce an impurity concentration gradient instead of a uniformly distributed concentration for calculating the charge behaviour in the degassed cables. For future study, space charge measurements in XLPE insulated cables subjected to thermal gradients need to be achieved, and it is also suggested to optimize the parameters linked with temperature for predicting the charge behaviour in loaded cables.

Chapter 7 Conclusions and future work

7.1 Conclusions

The dissertation concentrates on the research into space charge behaviour and electric field distribution in HVDC extruded cable insulation. The research work has been accomplished by implementing numerical modelling of the space charge behaviour in polyethylene-based material in cable geometry under the DC stress. The transient electric field distribution in the cable insulation has been studied by considering the practical operation of the HVDC cable system. A new modelling approach is proposed to investigate the space charge behaviour in XLPE material, which considers both the electronic and ionic charge carrier generation and transport mechanisms. A cable PEA system is built to measure the space charge accumulation in XLPE insulated cables, and the new modelling approach is also extended to investigate the hetero charge formation in XLPE insulated cables. Several conclusions can be drawn based on the present work.

Based on previous experimental observations, a threshold electric field (10 kV/mm for polyethylene based material) at which the charge injection takes place at the interface of electrode/insulation has been introduced into the bipolar charge transport model. The bipolar charge injection, the charge conduction mechanism, the charge trapping, detrapping and recombination processes are taken into account in the bipolar charge transport model. The space charge accumulation and the field inversion phenomenon can be successfully simulated by employing the bipolar charge transport model in a MV size polymeric cable (insulation thickness 4.5 mm) in the presence of a steady temperature gradient. The calculated space charge and field distribution are very consistent with the previous experimental observations [75]. Comparisons have been made between the conventional conductivity model and the bipolar charge transport model, and it is found that the bipolar charge transport theory is superior in calculating electric field in DC cable systems, due to its well descriptions on charge generation and transport mechanisms. The space charge behaviour and the transient field distribution in DC cable under the voltage polarity reversal have been calculated by the bipolar charge transport model, and the significant field enhancement near the conductor can be predicted immediately after the polarity reversal. It is suggested that the fast polarity reversal may lead to a higher electric field near the conductor, and the slow polarity reversal is more preferable as the space charge accumulation can be eased during the grounding stage.

Thermal transient effects on space charge accumulation in the DC cable insulation have been investigated by employing the bipolar charge transport model. The transient temperature distribution across the cable insulation can be achieved by applying a time-varying current (200-300 A) flowing in the cable conductor. Both the charge injection and the charge transport mechanisms are highly dependent on the temperature. It is found that the field inversion phenomenon can only take place with a higher load current which represents a higher general temperature and a larger temperature gradient, and this phenomenon can be still maintained even with the temperature decreasing, as the charge movement under the low temperature condition is insignificant. The space charge and field distribution have been investigated in DC cable insulation subjected to a cyclic load lasting 3 days. It is found that maximum electric field strength is always maintained near the outer insulation, and both the charge and field distribution are mainly dependent on the high load period. The space charge accumulation almost remains unchanged, since the charge generation and transport are very limited during low load periods.

Both the homo charge and hetero charge formation have been experimentally observed on the additive-free LDPE film, the fresh and the degassed XLPE specimens via space charge measurements. Under 20 kV/mm DC field, homo charge distribution is dominant in pure LDPE samples, and a large amount of hetero charges can be observed in the vicinity of both electrodes in the fresh XLPE samples. The amount of hetero charges can be greatly reduced by the degassing process, which indicates the hetero charge formation is mainly contributed from the ionization of dissociable impurities presenting within the insulation. A modelling approach has been proposed to investigate the space charge behaviour in XLPE material by considering both the electronic and ionic charge behaviour. An impurity molecule is introduced as the neutral ion-pairs, which can be dissociated into positive and negative ions by overcoming a dissociation barrier. The trapping, detrapping and recombination processes of the ionic charge carriers are considered in this model. The considerable hetero charge formation in the fresh XLPE specimens can be successfully simulated by considering the combination of electronic charge distribution and the ionic charge distribution, and the very limited charge accumulation in the degassed XLPE samples can also be calculated. The simulation results are quantitatively consistent with the experimental observations in XLPE material.

A PEA system for measuring space charge in cables has been successfully established, and the temperature gradient setup is installed into the system. Space charge measurements have been carried on the both original and degassed cable samples under 80 kV at the room temperature. Considerable hetero charge formation can be found in the original cable samples, and much less space charge accumulation can be detected in the degassed cable samples, since thermal treatment removes most volatile species such as crosslinking by-products. The modelling approach which considering both the ionic and electronic charge behaviour has been extended to cable geometry to simulate the space charge behaviour in XLPE insulated cables. Both the hetero charge formation and the field enhancement near the cathode can be calculated and the results show good consistency in original cable samples. The limited charge accumulation and slightly deformed field can be calculated in the degassed cable samples. However, it seems necessary to introduce an impurity concentration gradient instead of a uniformly distributed concentration for calculating the charge behaviour in the degassed cable samples.

7.2 Future work

Future work can be expanded from several aspects as following:

The space charge behaviour in DC cables in the presence of a temperature gradient has been successfully investigated by numerically modelling. A threshold electric field has been introduced to define the charge injection from the interface of electrode/insulation. The Schottky injection law dominates when the applied electric field exceeds the threshold, and the conduction of Ohmic type takes over under the low field. However, it is found that the threshold field could vary with different temperature. For both LDPE and XLPE, generally, a higher temperature leads to a smaller threshold field. In further study, the temperature dependence of the injection threshold field should be investigated at the interface of the electrode and polymeric insulation, which can assist to investigate the space charge accumulation in polymeric insulation under different thermal conditions.

The modified bipolar charge transport model in cable geometry is able to reproduce the space charge behaviour, the field inversion phenomenon and the enhancement of maximum electric field, which are observed experimentally in DC cable insulation. However, the parameter setting is still following the measurements achieved on LDPE. The parameters need to be optimized for a XLPE material from the measurements of space charge and conduction current under various electric fields and at different temperatures.

The space charge behaviour and transient field distribution under the polarity reversal and cyclic load have been studied by employing the bipolar charge transport model, which indicates such modelling approach can be applied to predict the electric field distribution in cable insulation subjected to different electrical and thermal stresses. The modelling method should be developed for full size HVDC cable design by considering the practical operation stages of the HVDC cable system. A more complicated heat transfer model considering the whole structure of the HVDC cable and the ambient environment should be developed to calculate the real temperature distribution across the insulation.

The PP-based cable technology has become the hotspot in the development of HVDC extruded cable systems recently, as the thermoplastic material is recyclable and no crosslinking and degassing are needed. The modelling approach could be developed for a PP-based material to provide recommendations on the operation and design of the PP-based cable systems.

Based on the assumptions of ionic dissociation, the formation and transport of ionic charge carriers have been fed into bipolar charge transport model, and the proposed model has been successfully employed to simulate the space charge behaviour in XLPE. However, the parameters linked with the ionic charge carriers are estimated following the parameter setting of the electronic charge carriers. The ionic dissociation mechanism of the impurity such as crosslinking by-products is still unclear in XLPE material, and the types of ions generated from the dissociation still need to be identified. The ionic charge behaviour in XLPE should be further studied, and the interactions between the ionic charge carriers and the electronic ones need to be investigated.

Space charge measurements have been successfully achieved on the original and degassed XLPE insulated cables at room temperature, and simulations have been performed to simulate the hetero charge formation in XLPE cables. However, it seems necessary to introduce an impurity concentration gradient instead of a uniformly distributed concentration for calculating the space charge behaviour in the degassed cable samples. The impurity diffusion in the cable insulation during the degassing process and the loading period need to be investigated, to obtain the distribution of the residual impurities. In future study, the cable PEA system including the temperature gradient setup need to be further improved, in order to achieve the space charge measurement in XLPE cables subjected to thermal gradients in safety. It is also suggested to optimize the parameters linked with temperature in the model for predicting the charge behaviour in loaded cables.

Appendix A [MATLAB Code]

In this part, the MATLAB code for calculating the space charge and field distribution in the medium voltage size polymeric insulation cable by the bipolar charge transport model will be shown. The simulation is implemented by using partial differential equation (PDE) solvers in MATLAB coding, to calculate the charge density for each species along the insulation radius. Both the calculated space charge and field distribution are same with the simulation results from modelling by COMSOL Multiphysics, as presented in Figures A.1 and A.2.

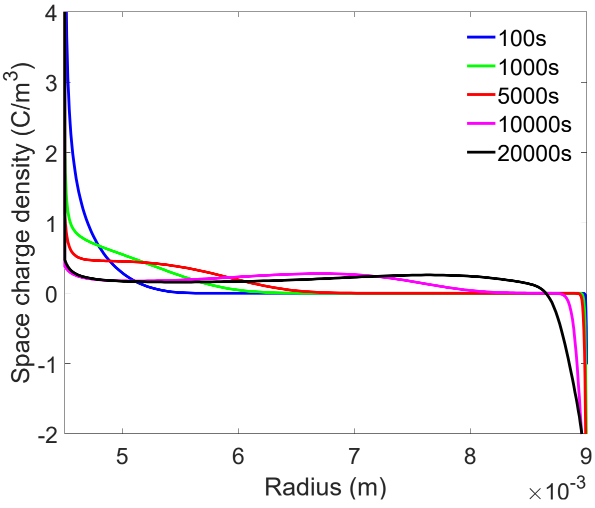

Figure A.1. The calculated space charge density in the MV size polymeric cable by the bipolar charge transport model.

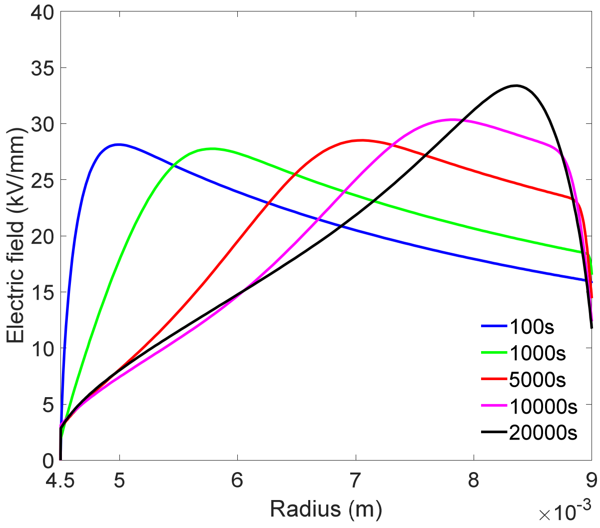

Figure A.2. The calculated electric field distribution in the MV size polymeric cable by the bipolar charge transport model.

```
%By Yunpeng Zhan on 01 Nov,2018
%PhD programme in EPE group of ECS
%Modelling of dynamics of Space Charge in cable under DC High Electric Field
%Supervisor : Prof. George Chen
%Assuming there is no charge in the bulk of the sample at time t<=0
%Definition of constants
global V d m alt dx dt K ec epr Be Bh S0 S1 S2 S3 Eot Hot Wei Whi A para_a para_we para_wh Tinner Touter alpha R0 Wtre Wtrh h dx_add;
%------------------------------------------
alt=1000;                        %number of iterations
alpha=10;                        % angle
V=90e3;                          %External applied voltage ( in volts )
d=4.50e-3;                       %sample thickness (in metres)
m=180;                           %number of equal divisions
dx_add=d/((1+m/2)*m/2);
dxUp=[dx_add:dx_add:(dx_add*m/2)];
dxDown=[(dx_add*m/2):-dx_add:dx_add];
dx=[dxUp dxDown];                     %divisional length_equal addition
R0=4.5e-3;                            %inter radius
dt=0.1;                               %time step = time difference between each loop ( in secs )/10^-2
K=1.380658e-23;                       %Boltzmann's constant
ec=1.6e-19;                           %Electronic charge
epr=2.3*8.854e-12;                    %Permittivity of the Sample material
Be=0.05;         Bh=0.05;             %Trapping coefficient for electrons & holes ( s^-1 )
%Recombination coefficients ( m^3C^-1s^-1 )for
S0=0;                                 %trapped electron/trapped hole
S1=0;                                 %mobile electron/trapped hole
S2=0;                                 %trapped electron/mobile hole
S3=0;                                 %mobile electron/mobile hole
Eot=100;         Hot=100;             %Trap density for electrons & holes
Wei=1.27;         Whi=1.16;           %Barrier Height for injection for electrons & holes
Wtre=0.96;        Wtrh=0.99;          % detrapping coefficents
h=6.626e-34;                          % detrapping constant
A=1.2e6;                              %Richardson constant [ Am^-1K^-2 ]
%Temperature
Tinner=65+273;
Touter=45+273;
para_a=2.5e-9;                        %distance between traps
para_we=0.71;                         %trap depth (eV) for hopping mobility
para_wh=0.65;
set=1;
%initiation / defination of working matrix
E=zeros(1,m);                         %Mobile Electron densities
H=zeros(1,m);                         %Mobile hole densities
Et=zeros(1,m);                        %Densities of Trap Electon
Ht=zeros(1,m);                        %Densities of Trap Hole
N=(H - E + Ht - Et);                  %Effective Current density
JE=zeros(1,m-1);                      %Current density of electrons
JH=zeros(1,m-1);                      %Current density of holes
DC=zeros(1,m-1);                      %Density of Displacement current
TC=(JE + JH + DC);                    %Total current density
F=zeros(1,m);                         %Electric field
fprintf('Hopping Mobility: DC %skV on %sum LDPE (cable geometry)\nApplied field: %skV/mm\n',num2str(V/1e3),num2str(d/1e-6),num2str((1e-6*V/d)));
[ch,F1,DC1,TC1,Esave,Hsave,Etsave,Htsave,JEsave,JHsave,E,H,Et,Ht,JE,JH,F,N,DC,TC]=Junwei_prog_linx(E,H,Et,Ht,F,N);
savefile = strcat('Cable_',num2str(alt*dt),'s','_L_set',num2str(set));
save(savefile,'ch','F1','DC1','TC1','Esave','Hsave','Etsave','Htsave','JEsave','JHsave','set','E','H','Et','Ht','JE','JH','F','N','DC','TC');
for i=1:1:499
```

```
fname1 = strcat('Cable_',num2str(i*alt*dt),'s','_L_set',num2str(i));
load(fname1,'E','H','Et','Ht','F','N');
[ch,F1,DC1,TC1,Esave,Hsave,Etsave,Htsave,JEsave,JHsave,E,H,Et,Ht,JE,JH,F,N,DC,TC]=Junwei_prog_linx(E,H,Et,Ht,F,N);

fname2 = strcat('Cable_',num2str((i+1)*alt*dt),'s','_L_set',num2str(i+1));
save(fname2,'ch','F1','DC1','TC1','Esave','Hsave','Etsave','Htsave','JEsave','JHsave','set','E','H','Et','Ht','JE','JH','F','N','DC','TC');

end

function [ch,F1,DC1,TC1,Esave,Hsave,Etsave,Htsave,JEsave,JHsave,E,H,Et,Ht,JE,JH,F,N,DC,TC]=Junwei_prog_linx(E,H,Et,Ht,F,N)
global V d m alt dx dt K ec epr Wei Whi A para_a para_we para_wh Tinner Touter alpha R0 Wtre Wtrh h Dek Dhk dx_add S1 S2 S3 ;
%index of the 1st iteration
a=1;
format long;
%calculation for temperature distribution.
for z=2:m
r(1)=R0+d;
r(z)=R0+d-sum(dx(1:z-1));
end
r(m+1)=d;
Mid_r=(r(1:m)+r(2:m+1))/2;
T_matrix=Touter+(Tinner-Touter)/log((R0+d)/d)*log((R0+d)./Mid_r);
v=K*T_matrix/h;                  %escape frequency
De=v.*exp(-Wtre*ec/K./T_matrix);   %detrapping coefficient
Dh=v.*exp(-Wtrh*ec/K./T_matrix);
% -------------------
% Poisson's Equation
% -------------------
for t=1:alt
F0=F;   %electric field at time t=0s
for k = 1:m
b = 0;
for i = 1:k
b = b + (i-0.5)*N(i)*dx(i)*Mid_r(i);
end
c = 0;
for w = k:m
c = c + (m-w+0.5)*N(w)*dx(w)*Mid_r(w);
end
F(k) = 1./Mid_r(k)*((c-b)/(epr*(m)))+1./Mid_r(k)*(V/log((R0+d)/(d)));

end
F1(a:t*m)=F;
%for displacement current DC(k)
DC(1:m-1)=epr*((F(1:m-1)-F0(1:m-1))/dt);
DC1(a:(t*m)-1)=DC;
% ------------------------------
% Transport & Continuity Equation
% ------------------------------
%hopping type mobility
Ue=2.*v*para_a./F.*exp(-1*para_we*ec./(K.*T_matrix)).*sinh(ec.*F*para_a./(2*K.*(T_matrix)));
Uh=2.*v*para_a./F.*exp(-1*para_wh*ec./(K.*T_matrix)).*sinh(ec.*F*para_a./(2*K.*(T_matrix)));
% solve for the s value ( by assuming J value can be formulated)
% Schottky Injection for E at Cathode(k=1) and H at Anode (k=m)
%     JE_Catd = A*T_matrix(1)^2*exp(-(ec*Wei/(K*T_matrix(1))))*(exp((ec/(K*T_matrix(1)))*sqrt((ec*abs(F(1)))/(4*pi*epr)))-1);
%     JH_Anod = A*T_matrix(m)^2*exp(-(ec*Whi/(K*T_matrix(m))))*(exp((ec/(K*T_matrix(m)))*sqrt((ec*abs(F(m)))/(4*pi*epr)))-1);
```

```
% if F(1)<0
%     JE_Catd = A*T_matrix(1)^2*exp(-(ec*Wei/(K*T_matrix(1))))*(exp((ec/(K*T_matrix(1)))*sqrt((ec*abs(F(1)))/(4*pi*epr))));
% else
%     JE_Catd=0;
% end
% if F(m)<0
%     JH_Anod = A*T_matrix(m)^2*exp(-(ec*Whi/(K*T_matrix(m))))*(exp((ec/(K*T_matrix(m)))*sqrt((ec*abs(F(m)))/(4*pi*epr))));
% else
%     JH_Anod=0;
% end
%
JE = Ue(1:m-1).*E(1:m-1).*abs(F(1:m-1));
JH = Uh(2:m).*H(2:m).*abs(F(2:m));
%Total current density added as shown
TC=JE + JH + DC;
JEsave(a:(t*m)-1)=JE;
JHsave(a:(t*m)-1)=JH;
TC1(a:(t*m)-1)=TC;
%Extraction of electrons and holes respectively
%at the Anode and Cathode under no extraction barrier
JE_Anod = Ue(m)*E(m)*abs(F(m));
JH_Catd = Uh(1)*H(1)*abs(F(1));

% ------------------ODE initial condition----------------
E(1) = (-(JE(1) - JE_Catd)/dx(1)-JE(1)/Mid_r(1))*(dt) + E(1);
H(m) = (-(JH(m-1) - JH_Anod)/dx(m)-JH(m-1)/Mid_r(m))*(dt) + H(m);
E(2:m-1) = (-(JE(2:m-1) - JE(1:m-2))./dx(2:m-1)-JE(2:m-1)./Mid_r(2:m-1))*dt + E(2:m-1);
H(2:m-1) = (-(JH(1:m-2) - JH(2:m-1))./dx(2:m-1)-JH(1:m-2)./Mid_r(1:m-2))*dt + H(2:m-1);
E(m) = (-(JE_Anod - JE(m-1))/dx(m)-JE_Anod/Mid_r(m))*(dt) + E(m);
H(1) = (-(JH_Catd - JH(1))/dx(1)-JH_Catd/Mid_r(1))*(dt) + H(1);

% --------------------ODE solver---------------------------
for k=1:m
Dek=De(k);
Dhk=Dh(k);
S1=Ue(k)/epr;
S2=Uh(k)/epr;
S3=(Ue(k)+Uh(k))./epr;
tspan = [0 dt];
y0 = [E(k), H(k), Et(k), Ht(k)];
sol = ode45(@f,tspan,y0);
x = dt;
y = deval(sol,x);
%------- setting the output of ODE to the species value ------
E(k) = y(1,:);
H(k) = y(2,:);
Et(k) = y(3,:);
Ht(k) = y(4,:);
end % for ODE solver
Esave(a:t*m)=E;
Hsave(a:t*m)=H;
Etsave(a:t*m)=Et;
Htsave(a:t*m)=Ht;
N = (H - E + Ht - Et);
ch(a:t*m)=N;
a=a+m;
if mod(t*dt,1)==0
fprintf('Time step is %ss; Charging at %ss.\n',num2str(dt),num2str(t*dt));
end
end % for iterations
```

```
% ---------------------------------------------------------------
function dNdt = f(t,y)

global Be Bh S0 S1 S2 S3 Eot Hot Dek Dhk;

% y1 = E, y2 = H, y3 = Et, y4 = Ht
dNdt = [ -S1*y(4)*y(1) - S3*y(2)*y(1) - Be*y(1)*(1-(y(3)/Eot))+Dek*y(3)
-S2*y(2)*y(3) - S3*y(2)*y(1) - Bh*y(2)*(1-(y(4)/Hot))+Dhk*y(4)
-S2*y(2)*y(3) - S0*y(4)*y(3) + Be*y(1)*(1-(y(3)/Eot))-Dek*y(3)
-S1*y(4)*y(1) - S0*y(4)*y(3) + Bh*y(2)*(1-(y(4)/Hot))-Dhk*y(4) ];

%--------------------------------------------------------------
%                    * * END * *
%--------------------------------------------------------------
```

List of References

[1] G. Chen, M. Hao, Z. Xu, A. Vaughan, Cao, Junzheng, and H. Wang, “Review of High Voltage Direct Current Cables,” *10 Csee J. Power Energy Syst.*, vol. 1, no. 2, pp. 9–21, 2015.

[2] M. Jeroense, “HVDC, the next generation of transmission: highlights with focus on extruded cable systems,” *IEEJ Trans. Electr. Electron. Eng.*, vol. 5, no. 4, pp. 400–404, 2010.

[3] T. L. Hanley, R. P. Burford, R. J. Fleming, and K. W. Barber, “A general review of polymeric insulation for use in HVDC cables,” *IEEE Electr. Insul. Mag.*, vol. 19, no. 1, pp. 13–24, 2003.

[4] G. Mazzanti and G. C. Montanari, “Electrical aging and life models: the role of space charge,” *IEEE Trans. Dielectr. Electr. Insul.*, vol. 12, no. 5, pp. 876–890, 2005.

[5] G. Mazzanti and M. Marzinotto, *Extruded cables for high-voltage direct-current transmission: advances in research and development*, vol. 93. John Wiley & Sons, 2013.

[6] R. Liu, “Long-distance DC electrical power transmission,” *IEEE Electrical Insulation Magazine*, vol. 29, no. 5. pp. 37–46, 2013.

[7] A. G. Siemens, “High voltage direct current transmission–proven technology for power exchange,” *Erlangen, Brochure*, 2011.

[8] D. Van Hertem, O. Gomis-Bellmunt, and J. Liang, “Comparison of HVAC and HVDC technologies,” in *HVDC Grids: For Offshore and Supergrid of the Future*, pp.79-96, 2016.

[9] G. Bianchi, G. Luoni, and A. Morello, “High voltage DC cable for bulk power transmission,” *IEEE Trans. Power Appar. Syst.*, no. 6, pp. 2311–2317, 1980.

[10] O. E. Oni, I. E. Davidson, and K. N. I. Mbangula, “A review of LCC-HVDC and VSC-HVDC technologies and applications,” in *2016 IEEE 16th International Conference on Environment and Electrical Engineering (EEEIC).*, pp. 1–7, 2016.

[11] M. P. Bahrman and B. K. Johnson, “The ABCs of HVDC transmission technologies,” *IEEE power energy Mag.*, vol. 5, no. 2, pp. 32–44, 2007.

[12] R. Rendina, A. Gualano, M. R. Guarniere, G. Pazienza, E. Colombo, S. Malgarotti, F. Bocchi, A. Orini, T. Sturchio and S. Aleo, “Qualification test program for the 1000 MW-500 kV HVDC very deep water submarine cable interconnection between Sardinia island and Italian peninsula (SA. PE. I),” in *CIGRE Session*, 2008, vol. 42, pp. 1–8.

[13] T. Worzyk, *Submarine power cables: design, installation, repair, environmental aspects*.

Springer Science & Business Media, 2009.

[14] C. A. Arkell and A. F. Parsons, "Insulation design of self contained oil-filled cables for DC operation," *IEEE Trans. Power Appar. Syst.*, no. 6, pp. 1805–1814, 1982.

[15] G. Bahder, G. S. Eager, G. W. Seman, F. E. Fischer, and H. Chu, "Development of±400 KV/±High and Medium-Pressure Oil-Filled Paper Insulated DC Power Cable System," *IEEE Trans. Power Appar. Syst.*, no. 6, pp. 2045–2056, 1978.

[16] R. Hata, "Solid DC submarine cable insulated with polypropylene laminated paper (PPLP)," *SEI TECHNICAL REVIEW-ENGLISH EDITION-62*, 2006.

[17] M. Ardelean and P. Minnebo, "HVDC Submarine Power Cables in the World: State-of-the-Art Knowledge," *Publ. jrc. ec. Eur. eu*, 2015.

[18] M. Jeroense, "HVDC Light cable system extended to 320 kV,", *CIGRE conference in Paris,* 2008.

[19] A. Gustafsson, M. Saltzer, A. Farkas, H. Ghorbani, T. Quist, and M. Jeroense, "The new 525 kV extruded HVDC cable system," *ABB Grid Syst. Tech. Pap.*, 2014.

[20] P. Bergelin, M. Jeroense, T. Quist, and H. Rapp, "640 kV extruded HVDC cable system," *NKT HV Cables Lyckeby, Sweden*, 2017.

[21] X. Huang, Y. Fan, J. Zhang, and P. Jiang, "Polypropylene based thermoplastic polymers for potential recyclable HVDC cable insulation applications," *IEEE Trans. Dielectr. Electr. Insul.*, vol. 24, no. 3, pp. 1446–1456, 2017.

[22] T. Andritsch, A. Vaughan, and G. C. Stevens, "Novel insulation materials for high voltage cable systems," *IEEE Electr. Insul. Mag.*, vol. 33, no. 4, pp. 27–33, 2017.

[23] J. He and Y. Zhou, "Progress in eco-friendly high voltage cable insulation materials," in *2018 12th International Conference on the Properties and Applications of Dielectric Materials (ICPADM)*, pp. 11–16, 2018.

[24] Z. Li and B. Du, "Polymeric insulation for high-voltage dc extruded cables: challenges and development directions," *IEEE Electr. Insul. Mag.*, vol. 34, no. 6, pp. 30–43, 2018.

[25] Y. Zhou, S. Peng, J. Hu, and J. He, "Polymeric insulation materials for HVDC cables: Development, challenges and future perspective," *IEEE Trans. Dielectr. Electr. Insul.*, vol. 24, no. 3, pp. 1308–1318, 2017.

[26] X. Huang, J. Zhang, P. Jiang, and T. Tanaka, “Material progress toward recyclable insulation of power cables part 2: Polypropylene-based thermoplastic materials,” *IEEE Electr. Insul. Mag.*, vol. 36, no. 1, pp. 8–18, 2019.

[27] M. Fu, L. A. Dissado, G. Chen, and J. C. Fothergill, “Space charge formation and its modified electric field under applied voltage reversal and temperature gradient in XLPE cable,” *IEEE Trans. Dielectr. Electr. Insul.*, vol. 15, no. 3, 2008.

[28] M. S. Khalil, “International research and development trends and problems of HVDC cables with polymeric insulation,” *IEEE Electr. Insul. Mag.*, vol. 13, no. 6, pp. 35–47, 1997.

[29] U. H. Nilsson and J. O. Boström, “Influence of the semiconductive material on space charge build-up in extruded HVDC cables,” in *2010 IEEE International Symposium on Electrical Insulation*, pp. 1–4, 2010.

[30] Z. An, Q. Yang, C. Xie, Y. Jiang, F. Zheng, and Y. Zhang, “Suppression effect of surface fluorination on charge injection into linear low density polyethylene,” *J. Appl. Phys.*, vol. 105, no. 6, p. 64102, 2009.

[31] G. A. Cartwright, A. E. Davies, S. G. Swingler, and A. S. Vaughan, “Effect of an antioxidant additive on morphology and space-charge characteristics of low-density polyethylene,” *IEE Proceedings-Science, Meas. Technol.*, vol. 143, no. 1, pp. 26–34, 1996.

[32] T. Mizuno, T. Takahashi, H. Harada, N. Hayashi, Y. Tanaka, and T. Maeno, “Effect of conductive inorganic filler on space charge characteristics in XLPE as a HVDC insulating material,” *Pap. c*, vol. 5, 2011.

[33] T. Tanaka, A. Bulinski, J. Castellon, M. Frechette, S. Gubanski, J. Kindersberger, G.C. Montanari, M. Nagao, P. Morshuis, Y. Tanaka and S. Pelissou, “Dielectric properties of XLPE/SiO2 nanocomposites based on CIGRE WG D1. 24 cooperative test results,” *IEEE Trans. Dielectr. Electr. Insul.*, vol. 18, no. 5, pp. 1482–1517, 2011.

[34] T. Yamanaka, S. Maruyama, and T. Tanaka, “The development of DC+/-500 kV XLPE cable in consideration of the space charge accumulation,” in *Proceedings of the 7th International Conference on Properties and Applications of Dielectric Materials*, vol. 2, pp. 689–694, 2003.

[35] T. Andritsch, R. Kochetov, P. H. F. Morshuis, and J. J. Smit, “Influence of manufacturing on dielectric performance of nanocomposites,” in *2013 IEEE International Conference on Solid Dielectrics (ICSD)*, pp. 900–903, 2013.

[36] H. Fukagawa, H. Miyauchi, Y. Yamada, S. Yoshida, and N. Ando, “Insulation properties of 250

kV DC XLPE cables," *IEEE Trans. Power Appar. Syst.*, no. 7, pp. 3175–3184, 1981.

[37] G. Asplund, "HVDC using voltage source converters-a new way to build highly controllable and compact HVDC substations," *Int. Counc. Large Electr. Syst. CIGRÉ 2000*, pp. 2–4, 2000.

[38] L. A. Dissado and J. C. Fothergill, *Electrical degradation and breakdown in polymers*, vol. 9. IET, 1992.

[39] K. S. Suh, S. J. Hwang, J. S. Noh, and T. Takada, "Effects of Constituents of XLPE on the Formation of Space Charge," *IEEE Trans. Dielectr. Electr. Insul.*, vol. 1, no. 6, pp. 1077–1083, 1994.

[40] M. Fu, G. Chen, L. A. Dissado, and J. C. Fothergill, "Influence of thermal treatment and residues on space charge accumulation in XLPE for DC power cable application," *IEEE Trans. Dielectr. Electr. Insul.*, vol. 14, no. 1, 2007.

[41] N. Hussin and G. Chen, "Analysis of space charge formation in LDPE in the presence of crosslinking byproducts," *IEEE Trans. Dielectr. Electr. Insul.*, vol. 19, no. 1, pp. 126–133, 2012.

[42] M. Fu, S. Hou, T. Liu, Z. Lv, K. Wu, Y. Wang and X. Wang, "Mechanism of space charge accumulation in crosslinked polyethylene under temperature gradient," in *2015 IEEE 11th International Conference on the Properties and Applications of Dielectric Materials (ICPADM)*, pp. 356–359, 2015.

[43] G. C. Montanari, J. Ghinello, F. Peruzzotti, and M. Albertini, "Endurance characteristics of XLPE compounds under DC voltage," in *ICSD'98. Proceedings of the 1998 IEEE 6th International Conference on Conduction and Breakdown in Solid Dielectrics*, pp. 439–442, 1998.

[44] N. Ando and F. Numajiri, "Experimental investigation of space charge in XLPE cable using dust figure," *IEEE Trans. Electr. Insul.*, no. 1, pp. 36–42, 1979.

[45] M. S. Khalil and B. S. Hansen, "Investigation of space charge in low-density polyethylene using a field probe technique," *IEEE Trans. Electr. Insul.*, vol. 23, no. 3, pp. 441–445, 1988.

[46] R. E. Collins, "Analysis of spatial distribution of charges and dipoles in electrets by a transient heating technique," *J. Appl. Phys.*, vol. 47, no. 11, pp. 4804–4808, 1976.

[47] H. von Seggern, "Thermal-pulse technique for determining charge distributions: Effect of measurement accuracy," *Appl. Phys. Lett.*, vol. 33, no. 2, pp. 134–137, 1978.

[48] P. Notingher, S. Agnel, A. Toureille, B. Rousset, and J.-L. Sanchez, "Characterization of

electric charge in non irradiated and irradiated MOS structures by thermal step and capacitance-voltage measurements," in *Electrical Insulation and Dielectric Phenomena, 2002 Annual Report Conference on*, pp. 95–100, 2002.

[49] S. B. Lang and D. K. Das-Gupta, "A technique for determining the polarization distribution in thin polymer electrets using periodic heating," *Ferroelectrics*, vol. 39, no. 1, pp. 1249–1252, 1981.

[50] T. Takada and T. Sakai, "Measurement of electric fields at a dielectric/electrode interface using an acoustic transducer technique," *IEEE Trans. Electr. Insul.*, no. 6, pp. 619–628, 1983.

[51] G. M. Sessler, J. E. West, and G. Gerhard, "High-resolution laser-pulse method for measuring charge distributions in dielectrics," *Phys. Rev. Lett.*, vol. 48, no. 8, p. 563, 1982.

[52] W. Eisenmenger and M. Haardt, "Observation of charge compensated polarization zones in polyvinylindenfluoride (PVDF) films by piezoelectric acoustic step-wave response," *Solid State Commun.*, vol. 41, no. 12, pp. 917–920, 1982.

[53] G. Ala, M. Caruso, V. Cecconi, S. Ganci, A. Imburgia, R. Miceli, P. Romano and F. Viola, "Review of acoustic methods for space charge measurement," *2015 AEIT Int. Annu. Conf. AEIT 2015*, pp. 3126–3142, 2016.

[54] Y. Murata, S. Masatoshi, A. Kazutoshi, I. Yoshiyuki, M. Shoji, K. Seiji and M. Osamu, "Development of high voltage DC-XLPE cable system," *SEI Tech. Rev*, vol. 101, pp. 55–62, 2013.

[55] G. Mazzanti, "Space charge measurements in high voltage DC extruded cables in IEEE Standard 1732," *IEEE Electr. Insul. Mag.*, vol. 33, no. 4, pp. 9–15, 2017.

[56] T. T. N. Vu, G. Teyssedre, B. Vissouvanadin, S. Le Roy, C. Laurent, M. Mammeri and I. Denizet, "Field distribution in polymeric MV-HVDC model cable under temperature gradient: simulation and space charge measurements," *Eur. J. Electr. Engg.*, vol. 17, pp. 307–325, 2014.

[57] S. Le Roy, G. Teyssedre, C. Laurent, G. C. Montanari, and F. Palmieri, "Description of charge transport in polyethylene using a fluid model with a constant mobility: fitting model and experiments," *J. Phys. D. Appl. Phys.*, vol. 39, no. 7, p. 1427, 2006.

[58] W. Choo, G. Chen, and S. G. Swingler, "Electric field in polymeric cable due to space charge accumulation under DC and temperature gradient," *IEEE Trans. Dielectr. Electr. Insul.*, vol. 18, no. 2, 2011.

[59] G. C. Montanari, D. Fabiani, and L. A. Dissado, “A new conduction phenomenon observed in polyethylene and epoxy resin: Ultra-fast soliton conduction,” *J. Polym. Sci. Part B Polym. Phys.*, vol. 49, no. 16, pp. 1173–1182, 2011.

[60] K. C. Kao, *Dielectric phenomena in solids*. Academic press, 2004.

[61] C. Laurent, G. Teyssedre, S. Le Roy, and F. Baudoin, “Charge dynamics and its energetic features in polymeric materials,” *IEEE Trans. Dielectr. Electr. Insul.*, vol. 20, no. 2, pp. 357–381, 2013.

[62] G. Teyssedre and C. Laurent, “Charge transport modeling in insulating polymers: From molecular to macroscopic scale,” *IEEE Trans. Dielectr. Electr. Insul.*, vol. 12, no. 5, pp. 857–874, 2005.

[63] K. J. Less and E. G. Wilson, “Intrinsic photoconduction and photoemission in polyethylene,” *J. Phys. C Solid State Phys.*, vol. 6, no. 21, p. 3110, 1973.

[64] R. Coelho and B. Aladenize, *Les diélectriques: propriétés diélectriques des matériaux isolants*. Hermès, 1993.

[65] C. Laurent, “Charge dynamics in polymeric materials and its relation to electrical ageing,” in *2012 Annual Report Conference on Electrical Insulation and Dielectric Phenomena*, pp. 1–20, 2012.

[66] J. Brunson, “Hopping conductivity and charge transport in low density polyethylene,” Utah State University, 2010.

[67] T. Takada, “Acoustic and optical methods for measuring electric charge distributions in dielectrics,” in *1999 Annual Report Conference on Electrical Insulation and Dielectric Phenomena*, pp. 1–14, 1999.

[68] T. Maeno and K. Fukunaga, “High-resolution PEA charge distribution measurement system,” *IEEE Trans. Dielectr. Electr. Insul.*, vol. 3, no. 6, pp. 754–757, 1996.

[69] T. Takeda *et al.*, “Space charge behavior in full-size 250 kV DC XLPE cables,” *IEEE Trans. Power Deliv.*, vol. 13, no. 1, pp. 28–39, 1998.

[70] K. Fukunaga, H. Miyata, M. Sugimori, and T. Takada, “Measurement of charge distribution in the insulation of cables using pulsed electroacoustic method,” *IEEJ Trans. Fundam. Mater.*, vol. 110, no. 9, pp. 647–648, 1990.

[71] N. Hozumi, T. Takeda, H. Suzuki, and T. Okamoto, “Space charge behavior in XLPE cable

insulation under 0.2-1.2 MV/cm dc fields," *IEEE Trans. Dielectr. Electr. Insul.*, vol. 5, no. 1, pp. 82–90, 1998.

[72] M. Fu, G. Chen, A. E. Davies, and J. G. Head, "Space charge measurements in power cables using a modified PEA system," *IET Conference Proceedings,* p. 74-79, 2000.

[73] G. Chen and M. Fu, "Space charge measurement in polymer insulated power cables using flat ground electrode PEA system," *in IEE Proceedings-Science, Measurement and Technology,* vol. 150, no. 2, pp. 89–96, 2003.

[74] R. Bodega, "Space charge accumulation in polymeric high voltage DC cable systems," 2006.

[75] D. Fabiani, G. Montanari, C. Laurent, G. Teyssedre, P. Morshuis, R. Bodega, L. Dissado, "HVDC cable design and space charge accumulation. part 3: effect of temperature gradient," *IEEE Electr. Insul. Mag.*, vol. 24, no. 2, pp. 5–14, 2008.

[76] Y. Li, M. Yasuda, and T. Takada, "Pulsed electroacoustic method for measurement of charge accumulation in solid dielectrics," *IEEE Trans. Dielectr. Electr. Insul.*, vol. 1, no. 2, pp. 188–195, 1994.

[77] J. Zhao, "Dynamics of space charge and electroluminescence modelling in polyethylene." University of Southampton, 2012.

[78] W. Xia, C. Chen, J. Hao, K. Wu, X. Chen, L. Peng, C. Zhang, "Recovery Algorithm for Space Charge Waveform in Coaxial Cable under Temperature Gradient," *Sensors Mater.*, vol. 29, no. 8, pp. 1147–1157, 2017.

[79] M. Fu, "Space charge measurement in polymer insulated power cables using the PEA method.," 2004.

[80] B. Vissouvanadin, T. T. N. Vu, L. Berquez, S. Le Roy, G. Teyssedre, and C. Laurent, "Deconvolution techniques for space charge recovery using pulsed electroacoustic method in coaxial geometry," *IEEE Trans. Dielectr. Electr. Insul.*, vol. 21, no. 2, pp. 821–828, 2014.

[81] E. Ildstad, F. Mauseth, and G. Balog, "Space charge and electric field distribution in current loaded polyethylene insulated HVDC cables," in *Int. Symp. HV Eng*, p. 366, 2003.

[82] P. H. F. Morshuis, R. Bodega, D. Fabiani, G. C. Montanari, L. A. Dissado, and J. J. Smit, "Calculation and Measurement of Space Charge in MV-size Extruded Cables Systems under Load Conditions," in *Solid Dielectrics, 2007. ICSD'07. IEEE International Conference on*, pp. 502–505, 2007.

[83] R. N. Hampton, “Some of the considerations for materials operating under high-voltage, direct-current stresses,” *IEEE Electr. Insul. Mag.*, vol. 24, no. 1, pp. 5–13, 2008.

[84] Z. Y. Huang, J. A. Pilgrim, P. L. Lewin, and S. G. Swingler, “Real-time electric field estimation for HVDC cable dielectrics,” in *Electrical Insulation Conference (EIC)*, pp. 1–4, 2015.

[85] M. J. P. Jeroense and P. H. F. Morshuis, “Electric fields in HVDC paper-insulated cables,” *IEEE Trans. Dielectr. Electr. Insul.*, vol. 5, no. 2, pp. 225–236, 1998.

[86] B. Aladenize, R. Coelho, J. C. Assier, H. Janah, and P. Mirebeau, “Field distribution in HVDC cables: Dependence on insulating materials,” in *Jicable*, vol. 99, p. p557, 1999.

[87] I. W. McAllister, G. C. Crichton, and A. Pedersen, “Charge accumulation in DC cables: A macroscopic approach,” in *Proceedings of 1994 IEEE International Symposium on Electrical Insulation*, pp. 212–216 , 1994.

[88] S. Boggs, D. H. Damon, J. Hjerrild, J. T. Holboll, and M. Henriksen, “Effect of insulation properties on the field grading of solid dielectric DC cable,” *IEEE Trans. power Deliv.*, vol. 16, no. 4, pp. 456–461, 2001.

[89] M. Hao, A. Fazal, A. S. Vaughan, G. Chen, H. Wang, C. Zhang, and Y. Zhou, “The effects of semicon on space charge behavior under different temperature conditions for HVDC cable insulation,” 2016.

[90] F. Aida, S. Wang, M. Fujita, G. Tanimoto, and Y. Fujiwara, “Study of the mechanism of space charge formation in polyethylene,” *J. Electrostat.*, vol. 42, no. 1–2, pp. 3–15, 1997.

[91] J. M. Alison and R. M. Hill, “A model for bipolar charge transport, trapping and recombination in degassed crosslinked polyethene,” *J. Phys. D Appl. Phys.*, vol. 27, pp. 1291–1299, 1994.

[92] M. Fukuma, M. Nagao, and M. Kosaki, “Computer analysis on transient space charge distribution in polymer,” in *Proceedings of 1994 4th International Conference on Properties and Applications of Dielectric Materials (ICPADM)*, vol. 1, pp. 24–27, 1994.

[93] K. Kaneko, T. Mizutani, and Y. Suzuoki, “Computer simulation on formation of space charge packets in XLPE films,” *IEEE Trans. Dielectr. Electr. Insul.*, vol. 6, no. 2, pp. 152–158, 1999.

[94] S. Le Roy, P. Segur, G. Teyssedre, and C. Laurent, “Description of bipolar charge transport in polyethylene using a fluid model with a constant mobility: model prediction,” *J. Phys. D. Appl. Phys.*, vol. 37, no. 2, pp. 298–305, 2004.

[95] S. Le Roy, G. Teyssedre, C. Laurent, and P. Segur, “Numerical model for studying dynamic space charge behavior in polyethylene,” in *Proceedings of the 7th International Conference on Properties and Applications of Dielectric Materials*, vol. 3, pp. 859–862, 2003.

[96] S. Le Roy, G. Teyssedre, P. Segur, and C. Laurent, “Modelling of space charge, electroluminescence and current in low density polyethylene under DC and AC field,” in *The 17th Annual Meeting of the IEEE Lasers and Electro-Optics Society*, pp. 29–32, 2004.

[97] G. Chen and S. H. Loi, “Space charge modelling in solid dielectrics under high electric field based on double charge injection model,” *MRS Online Proc. Libr. Arch.*, vol. 889, 2005.

[98] C. Zhou and G. Chen, “Space charge and AC electric breakdown strength in polyethylene,” *Annu. Rep. - Conf. Electr. Insul. Dielectr. Phenomena, CEIDP*, vol. 2015-Decem, pp. 106–109, 2015.

[99] J. Zhao, G. Chen, and L. Zhong, “Space charge in polyethylene under combined AC and DC voltages,” *Ieee Trans. Dielectr. Electr. Insul.*, vol. 21, no. 4, pp. 1757–1763, 2014.

[100] S. Le Roy, G. Teyssedre, and C. Laurent, “Modelling space charge in a cable geometry,” *IEEE Trans. Dielectr. Electr. Insul.*, vol. 23, no. 4, pp. 2361–2367, 2016.

[101] F. Boufayed, G. Teyssedre, C. Laurent, S. Le Roy, L. A. Dissado, P. Segur, and G. C. Montanari, “Models of bipolar charge transport in polyethylene,” *J. Appl. Phys.*, vol. 100, no. 10, p. 104105, 2006.

[102] N. Liu, C. Zhou, G. Chen, and L. Zhong, “Determination of threshold electric field for charge injection in polymeric materials,” *Appl. Phys. Lett.*, vol. 106, no. 19, p. 192901, 2015.

[103] G. C. Montanari, G. Mazzanti, F. Palmieri, A. Motori, G. Perego, and S. Serra, “Space-charge trapping and conduction in LDPE, HDPE and XLPE,” *J. Phys. D. Appl. Phys.*, vol. 34, no. 18, p. 2902, 2001.

[104] L. Chen, T. D. Huan, Y. C. Quintero, and R. Ramprasad, “Charge injection barriers at metal/polyethylene interfaces,” *J. Mater. Sci.*, vol. 51, no. 1, pp. 506–512, 2016.

[105] S. Boggs, “A rational consideration of space charge,” *IEEE Electr. Insul. Mag.*, vol. 20, no. 4, pp. 22–27, 2004.

[106] Y. L. Chong, G. Chen, and Y. F. F. Ho, “Temperature effect on space charge dynamics in XLPE insulation,” *IEEE Trans. Dielectr. Electr. Insul.*, vol. 14, no. 1, pp. 65–76, 2007.

[107] T. Mizutani, H. Semi, and K. Kaneko, “Space charge behavior in low-density polyethylene,”

IEEE Trans. Dielectr. Electr. Insul., vol. 7, no. 4, pp. 503–508, 2000.

[108] K. R. Bambery and R. J. Fleming, “The temperature dependence of space charge accumulation in cross-linked polyethylene,” *J. Therm. Anal.*, vol. 50, no. 1–2, pp. 19–31, 1997.

[109] S. Internasional, “IEC 60287-1-1; Electric cables–Calculation of the current rating–Part 1–1: Current rating equations (100% load factor) and calculation of losses–General. International Electrotechnical Commission (IEC) Geneva, Switzerland.”, 2006.

[110] G. F. Moore, *Electric cables handbook*. Blackwell Science, 1997.

[111] D. Fabiani, G. C. Montanari, R. Bodega, P. H. F. Morshuis, C. Laurent, and L. A. Dissado, “The effect of temperature gradient on space charge and electric field distribution of HVDC cable models,” in *2006 IEEE 8th International Conference on Properties & applications of Dielectric Materials*, pp. 65–68, 2006.

[112] S. Catmull, R. D. Chippendale, J. A. Pilgrim, G. Hutton, and P. Cangy, “Cyclic load profiles for offshore wind farm cable rating,” *IEEE Trans. Power Deliv.*, vol. 31, no. 3, pp. 1242–1250, 2015.

[113] T . Takeda; N. Hozumi; H. Suzuki; T. Okamoto, “Factor of Space Charge Generation in XLPE under DC Electric Field of 20 kV/mm,” no. 4, pp. 137–141, 1997.

[114] Y. Sekii, T. Ohbayashi, T. Uchimura, and T. Hukuyama, “A study on the space charge formation in XLPE,”in *Annual Report Conference on Electrical Insulation and Dielectric Phenomena*, pp. 469–472, 2001.

[115] Y. Maeno, N. Hirai, Y. Ohki, T. Tanaka, M. Okashita, and T. Maeno, “Effects of crosslinking byproducts on space charge formation in crosslinked polyethylene,” *IEEE Trans. Dielectr. Electr. Insul.*, vol. 12, no. 1, pp. 90–97, 2005.

[116] M. Hao, A. Fazal, A. S. Vaughan, G. Chen, Y. Zhou, and C. Zhang, “The impacts of degassing on space charge characteristics and DC conductivity in semicon-bonded XLPE for HVDC cable applications,” in *2016 IEEE Conference on Electrical Insulation and Dielectric Phenomena (CEIDP)*, pp. 97–100, 2016.

[117] T. Andrews, R. N. Hampton, A. Smedberg, D. Wald, V. Waschk, and W. Weissenberg, “The role of degassing in XLPE power cable manufacture,” *IEEE Electr. Insul. Mag.*, vol. 22, no. 6, pp. 5–16, 2006.

[118] K. M. Tibbetts, M. Tarazkar, T. Bohinski, D. A. Romanov, S. Matsika, and R. J. Levis,

"Controlling the dissociation dynamics of acetophenone radical cation through excitation of ground and excited state wavepackets," *J. Phys. B At. Mol. Opt. Phys.*, vol. 48, no. 16, p. 164002, 2015.

[119] R. Anbarasan, O. Babot, and B. Maillard, "Crosslinking of high-density polyethylene in the presence of organic peroxides," *J. Appl. Polym. Sci.*, vol. 93, no. 1, pp. 75–81, 2004.

[120] M. Chen, Y. Yin, H. Zhang, Z. Gao, Z. Ma, and J. Wu, "Effects of Acetophenone on Charge Dynamics in Low Density Polyethylene," in *2019 IEEE Electrical Insulation Conference (EIC)*, pp. 234–237, 2019.

[121] S. Le Roy and G. Teyssedre, "Ion generation and transport in low density polyethylene under electric stress," in *2015 IEEE Conference on Electrical Insulation and Dielectric Phenomena (CEIDP)*, pp. 63–66, 2015.

[122] Z. Lv, J. Cao, X. Wang, H. Wang, K. Wu, and L. A. Dissado, "Mechanism of space charge formation in cross linked polyethylene (XLPE) under temperature gradient," *IEEE Trans. Dielectr. Electr. Insul.*, vol. 22, no. 6, pp. 3186–3196, 2015.

[123] J. Wu, L. Lan, Z. Li, and Y. Yin, "Simulation of space charge behavior in LDPE with a modified of bipolar charge transport model," in *Proceedings of 2014 International Symposium on Electrical Insulating Materials*, pp. 65–68, 2014.

[124] C. Thomas, G. Teyssedre, and C. Laurent, "Space-charge dynamic in polyethylene: from dc to ac stress," *J. Phys. D. Appl. Phys.*, vol. 44, no. 1, p. 15401, 2010.

[125] G. C. Montanari, C. Laurent, G. Teyssedre, A. Campus, and U. H. Nilsson, "From LDPE to XLPE: investigating the change of electrical properties. Part I. space charge, conduction and lifetime," *IEEE Trans. Dielectr. Electr. Insul.*, vol. 12, no. 3, pp. 438–446, 2005.

[126] H. Ren *et al.*, "Influence of Crosslinking Byproducts on DC Conductivity of HVDC XLPE Cable Insulation," in *2018 IEEE Conference on Electrical Insulation and Dielectric Phenomena (CEIDP)*, pp. 90–93, 2018.

[127] A. Smedberg, A. B. Borealis, and D. Wald, "Determination of diffusion constants for peroxide by-products formed during the crosslinking of polyethylene," in *Conference Record of the 2008 IEEE International Symposium on Electrical Insulation*, pp. 586–590, 2008.

[128] J. Hjerrild, J. Holboll, M. Henriksen, and S. Boggs, "Effect of semicon-dielectric interface on conductivity and electric field distribution," *IEEE Trans. Dielectr. Electr. Insul.*, vol. 9, no. 4, pp. 596–603, 2002.

[129] L. Lan, J. Wu, Y. Yin, X. Li, and Z. Li, “Effect of temperature on space charge trapping and conduction in cross-linked polyethylene,” *IEEE Trans. Dielectr. Electr. Insul.*, vol. 21, no. 4, pp. 1784–1791, 2014.

[130] W. Xia, C. Chen, C. Cheng, Y. Wu, K. Wu, M. Fu, S. Hou, B. Hui, “Space charge characteristics in 160 kV DC XLPE cable under temperature gradient,” *IEEE Trans. Dielectr. Electr. Insul.*, vol. 25, no. 6, pp. 2366–2374, 2018.